NONLINEAR OPTICS IN NANOPHOTONIC STRUCTURES

A Dissertation

Presented to the Faculty of the Graduate School

of Cornell University

in Partial Fulfillment of the Requirements for the Degree of

Doctor of Philosophy

by

Kasturi Saha

May 2014

NONLINEAR OPTICS IN NANOPHOTONIC STRUCTURES

Kasturi Saha, Ph.D.

Cornell University 2014

Photonic structures such as photonic bandgap fibers and high confinement nanowaveguides have proven to be excellent platforms for studying nonlinear optical interactions tailored towards applications in spectroscopy, quantum communication, quantum computation protocols, optical clockwork and precision frequency metrology. This thesis discusses our approach towards exploiting these high confinement media for demonstrating novel few photon nonlinear optical interactions such as two-photon absorption and cross-phase modulation in hot atomic vapors (Rubidium) confined inside hollow-core photonic bandgap fibers (PBGF), generating ultra-broadband optical frequency combs that utilize cascaded parametric four-wave mixing and mode-locked femtosecond pulses in silicon nitride nanowaveguides.

We generate large optical depths in such a Rb-PBGF system, and the tight light confinement, high vapor density and long interaction length allow us to perform nonlinear optics at ultralow power. We observe 25% all-optical modulation with <20 photons, i.e., a few attojoules of energy, and large cross-phase shifts of 0.3 mrad per photon with a response time <5 ns in Rb-filled PBGF. This result takes us to within an order of magnitude of single-photon switching, and improves upon previous experiments for freely propagating optical fields, including those in cold-atoms.

Using high quality factor silicon nitride optical microcavities we show that the gain from the four-wave mixing process can lead to optical parametric os-

cillation, allowing for the generation of multiple new wavelengths as wide as an octave of wavelengths. Next we show that by dispersion engineering the waveguide dimensions, we can generate combs by pumping at 1064 nm. The advantage of this platform is that we can independently tune the free spectral range (FSR) and the dispersion. We exploit this property of the silicon nitride microresonator platform to generate microcombs with various FSRs such as 20-, 40-, 80-,100-GHz. Next we go on to characterize the spectral and temporal dynamics of the microresonator based combs and demonstrate that such parametric frequency combs can generate modelocked ultra-short pulses.

BIOGRAPHICAL SKETCH

Kasturi Saha was born in the city of Kolkata, located in the state of West Bengal, India on 19th September 1984. She spent the first 18 years of her life in Kolkata, enjoying the comforts of home and the love of parents and relatives. She has always believed in and respected the power of active research, which forms the basis of all major discoveries today. Her passion for Physics drove her out of her comfort zone as she joined St. Stephen's College, Delhi to do B.Sc. in Physics. Thereafter she went on to do M.Sc. from the Indian Institute of Technology, Delhi (IIT-D). Each summer break provided her opportunities for experiencing the research world of Physics and dirtying her hands with different projects, both in experimental and theoretical condensed matter physics and optical physics, while meeting eminent scientist at the Indian Institute of Science, Bangalore, Tata Institute of Fundamental Sciences, Mumbai and many other research institutes. Armed with IITs technical prowess and St.Stephen's scientific and intellectual foundations, she decided to pursue a Ph.D. in Physics. Kasturi left the country for the first time in Fall 2008 and came to Ithaca, NY, USA to pursue graduate study at Cornell University. She joined the Quantum and Nonlinear Photonics group of Prof. Alexander Gaeta in the School of Applied and Engineering Physics, and has been exploring nonlinear optical interactions in nanophotonic structures as part of her doctoral thesis research.

To Baba and Ma

ACKNOWLEDGEMENTS

"It is the supreme art of the teacher to awaken joy in creative expression and knowledge." - Albert Einstein.

First, I would like to thank my advisor Prof. Alexander Gaeta, although a few sentences of "thank you" is not enough for expressing my gratitude towards him. I thank you for always allowing me to express my rather strong opinions on any matter and patiently listening to all of my problems and issues. You have allowed me to explore a plethora of research problems, given me the freedom to work on what I like best, recognize the big picture and coherently present ideas. Your penchant for tiny details such as "the commas", "the only at most two colons per manuscript", "the hyphens", "the illustration in a manuscript or talk","Igor", and "Apple" are extremely contagious. You have been a constant source of inspiration and support throughout my doctoral program and always extremely encouraging, especially during tough times. Thank you! Next, I would like to thank Prof. Michal Lipson for agreeing to be my special committee member. Her vivacious and dynamic nature has always inspired me. I would also thank my other special committee members Prof. Mukund Vengalattore and Prof. Erich Mueller for their advice and support. Finally, I would like to thank Prof. Sunil Bhave for being my mentor and friend.

"Friendship is unnecessary, like philosophy, like art... It has no survival value; rather it is one of those things that give value to survival." C. S. Lewis

To my group-mates - you are my extended family. Without all of you, life in the Gaeta Group would not have been the same. Vivek was the first person I interacted before I joined this group and he turned out be the person I have coauthored many papers with in the years to come. I have always been amazed by his time management skills! Until I had got accustomed to his ways of working,

I must agree that it was quite frustrating waiting for him to turn up in lab to take data! You were and always will be -"when in doubt - go ask person". Thank you.

Me,"Yoshi...", Yoshi,"What???!!!, not again.. "..silence... followed by exchange of weird looks.. Yoshi,"ye..es, ..".. That is how every conversation has started to date. As I slowly moved from the Rubidium projects to the Silicon side of things, Yoshi and I have been constant companions. I've grown to know when not to disturb him and when to bug him endlessly. The hours spent in lab, being excited and sad about working and not working experiments, innumerable number of time-outs, conferences, and parties and the endless number of other things - these will forever remain as fond memories. I'm sure I'l always have a working "Yoshi-App", no matter where I go and where you are in this world! You've not only taught me how to tackle research problems, expand the scope of potential solutions, present data in the right way, but also how to be a responsible group-mate and a leader. You've shepherded me through the travails of scientific research and gradschool. I will always be indebted to you. Thank you! To Ting and Kai - I've shared many a happy outings with both of you. You will always be on my mind.

Bonggu you've taught me many a "life-lessons"! Your presence in the lab always filled the air with cheerfulness. The high-fives, the drawings on the white board, the "do-behaves", have all added the extra flavour of happiness in my Ph.D. Thank you and "I respect you a lot". To my ping-pong-mates - Bonggu, Vivek, Sam, Amar, Pablo - thank you for teaching me how to play table tennis. This has not only made my Ph.D. exciting and memorable, but also made me realise the importance of balance between work and play. Thanks to Sam, Adrea, Ryan, Alessandro, Henry, Stephane, Moti, Prathamesh, Chaitanya,

Mike, Emily, Jordan, Amar, Pablo, Imad, Dan, Reza, Mark, Chris, Mengjie, for being wonderful colleagues at various points of time. Special thanks to Jake and Kevin for fabricating the devices. I would also like to extend my thanks to others members of the Lipson group with whom I have interacted over the past 5 years. I will always be grateful to you for having learnt a great deal about science and doing research from all of you.

Apart from the Gaeta Group, I've made many friends in Ithaca, without whom survival in this lonely part of the planet would have been impossible. To start with, Saikat and Sharvari, whose home was my second home in Ithaca. Saikat, has played an important role not only as my friend and scientific mentor but also as my philosophical guide. Lauren, you will always remain my special friend. I will always be grateful to you for always being there. Amongst others, Tanay, Suresh, Amit, Shruti, Anand, Ashima, Krishna, Adarsh, Parag, Debashree, Deepti, Amit Viswas, Abhinandan, Ishita, Mihir, Shivam, Ajay, and Shreesha, thank you for all the wonderful time we have spent.

Last but not the least, I would like to thank my parents, relatives and Sid without whose support and unconditional love, life means nothing and it is because them, that I am who I am.

TABLE OF CONTENTS

Biographical Sketch . . . iii
Dedication . . . iv
Acknowledgements . . . v
Table of Contents . . . viii
List of Tables . . . x
List of Figures . . . xi

1 Introduction **1**
1.1 Nonlinear optics in nanophotonic structures . . . 1
1.1.1 Photonic bandgap fibers: Few-photon nonlinear optics . . . 3
1.1.2 Silicon nitride microresonators: Frequency comb generation 7
1.2 Thesis layout - chapter overview and collaborative work . . . 10

2 Few-Photon Nonlinear Optics in Rb-Filled Photonic Bandgap Fiber **12**
2.1 Introduction . . . 12
2.2 The system . . . 13
2.3 Two-photon absorption: Intensity and phase modulation . . . 17
2.3.1 Degenerate two-photon absorption . . . 18
2.3.2 Non-denegerate two-photon absorption . . . 28
2.3.3 Cross-phase modulation . . . 36
2.4 Summary and Conclusion . . . 42

3 Silicon Nitride Microresonator Based Optical Frequency Combs **44**
3.1 Introduction . . . 44
3.2 Generation of frequency comb . . . 45
3.2.1 Silicon based microresonator . . . 47
3.2.2 Parametric oscillation . . . 53
3.2.3 Octave spanning comb . . . 56
3.2.4 One micron comb . . . 64
3.2.5 Low repetition rate comb . . . 70
3.3 Frequency and time dynamics of frequency comb . . . 72
3.3.1 Temporal measurement technique: Intensity autocorrelation . . . 72
3.3.2 Time-lens technique . . . 84
3.4 Summary and Conclusion . . . 87

4 Integrating Rubidium with Microresonators **88**
4.1 Introduction . . . 88
4.2 Experimental setup . . . 88
4.3 Results . . . 90
4.4 Summary . . . 92

5 Optical isolation via Bragg Scattering Four Wave Mixing **93**
5.1 Introduction 93
5.2 Experiment and discussion 94
5.3 Conclusion 103

6 Summary and Future Directions **104**
6.1 Summary 104
6.2 Experiments related to photonic bandgap fiber 105
6.3 Experiments related to silicon nitride platform 107
6.3.1 Integrated Rb-SiN platform 107
6.3.2 Microresonator based frequency combs 108

A Group Velocity Dispersion **114**

Bibliography **117**

LIST OF TABLES

3.1 Pulse shapes, pulse widths, autocorrelation trace widths for different pulse shapes 75

LIST OF FIGURES

1.1 **Photonic bandgap fiber:** (a) Transmission electron microscope image of the cross section of the fiber (AIR-6-800 fiber from NKT Photonics [35]) used in these experiments. The core diameter is 6 μm and the fundamental mode area is ~10 μm^2 for the guided optical field. (b) Schematic of how light is guided in the fiber via optical interference [17]. 3

1.2 **Silicon nitride microresonator:** (a) A scanning electron micrograph of a silicon-nitride microresonator resonator of radius 112-μm with a free spectral range (FSR) of 225 GHz. (b) Micrograph of the waveguide cross-section. 8

1.3 **Illustration of a frequency comb:** Power spectrum of a frequency comb. 8

2.1 **Schematic of vacuum chamber:** Schematic of the vacuum chamber used for TPA. The Rb-PBGF system consists of an ultra-high vacuum (UHV) chamber with a Rb source attached, inside of which one or more PBGFs are mounted. On one side of the ultra high-vacuum (UHV) compatible stainless steel chamber, a cylindrical glass tube is attached which provides optical access to all sides of the fiber. Glass windows on either side allow for coupling into and out of either end of the fiber(s). 13

2.2 **Generation of Rubidium vapor:** Under steady-state conditions, the Rb atoms inside the PBGF core are all stuck to the inside walls of the fiber forming nanoclusters (b). A strong vapor-generation beam at ~805 nm (far detuned from the atomic transitions of Rb) coupled into the PBGF heats and evaporates the adsorbed nanoclusters, creating a vapor of Rb atoms in the core (c). The vapor density in the core is set by the generation beam power and duration. After the interaction is over the atoms collide with the walls of the fiber and coat it uniformly (a,d), until they form nanoclusters again. 15

2.3 **Schematic of energy level:** Energy level structure for TPA in Rb. Δ is the detuning from the intermediate level. We observe degenerate TPA at 778.1 nm. 18

2.4 **Simulated TPA:** (a) Expected two-photon absorption versus pump power in a Rb-filled PBGF with an optical depth of 100.(b) Quadratic dependence of two-photon fluorescence on pump power in hollow-core photonic bandgap fiber. 20

2.5 **Schematic of experimental setup for degenerate TPA:** The pump laser is split into two counter-propagating beams using a 50/50 beamsplitter (BS). The polarizations are made identical using polarization beam splitter (PBS) cubes, and the beams are then coupled through the hollow-core photonic bandgap fiber (PBGF). A blue colored glass is used to filter the fluorescence from the excited $6P_{3/2}$ state and then detected on a photomultiplier tube (PMT). An acousto-optic modulator (AOM-1) is used modulate the pump beams as a triangular wave at a 1-kHz frequency to vary linearly the intensity from 'x' to '4x' of the counter-propagating beams simultaneously. For lock-in detection of the TPA through the PBGF, one of the two counter-propagating beams is modulated using AOM-2 as a square wave at 25-kHz. The signal is detected on a photodiode (PD) using a pick-off beam at one end and sent to a lock-in amplifier, the ouput of which is subsequently monitored using an oscilloscope. 22

2.6 **TPA measurement through fluorescence:** Blue fluorescence signal detected by the PMT. Fluorescence peaks corresponding to each of the hyperfine ground states of ^{85}Rb and ^{87}Rb are observed as the pump laser is scanned in frequency. Since the two beams are perfectly counter-propagating in the fiber, all the peaks are Doppler-free. The peaks are homogeneously broadened due to the short transit time (~5 ns) of the Rb atoms across the $6 - \mu$m core of the fiber. 24

2.7 **Quadratic dependence of TPA:** Blue fluorescence signal (black dots) detected by the PMT as the pump laser power is varied using AOM-1 when the laser is tuned to the $5S_{1/2} \rightarrow 5D_{5/2}$ ($F = 3$ to F') two-photon transition of ^{85}Rb. The solid red line shows the expected square dependence of two-photon absorption on intensity. 25

2.8 **Direct measurement of TPA:** The blue circles show the data from the direct measurement of two-photon absorption from one of the pump beams using a lock-in detector as the pump laser was scanned across the $5S_{1/2} \rightarrow 5D_{5/2}$, $F_g = 3$ to F_e (778.1055 nm) two-photon transition of ^{85}Rb. The solid black line shows a fit of a sum of five Lorentzians which correspond to each of the hyperfine lines. The homogenous linewidth is estimated to be 73 ±10 MHz. 26

2.9 **Schematic of energy level for non-degenerate TPA:** TPA level scheme in $_{85}$Rb used for performing all-optical modulation. An atom in the ground $5S_{1/2}$ state can simultaneously absorb a photon each from the 780-nm control and 776-nm signal beams to make a resonant transition to the excited $5D_{5/2}$ state. The signal photon can only be absorbed if the control photon is also present. A small fraction of the excited atoms decay through the $6P_{3/2}$ level emitting blue fluorescence. 29
2.10 **Calculation of optimum detuning:** Optimum detuning for non-degenerate TPA. Absorption of the signal beam at two-photon resonance with varying detuning of the control beam from the intermediate $5P_{3/2}$ level. 29
2.11 **TPA dependence on optical depth:** Absorption of the signal beam at two-photon resonance with varying atomic density. . . . 31
2.12 **Schematic of experimental setup:** Experimental setup for few-photon all-optical modulation. The polarizations of the signal and control beams are made identical (circular) using polarization beam splitter (PBS) cubes and quarter ($\lambda/4$) waveplates, and the beams are then coupled counter-propagating into the fiber. A pick-off is used to monitor the transmission of the signal beam using a sensitive photodetector (PD). A strong (3 mW) off-resonant vapor generation beam is also coupled into the fiber to generate the desired atomic density and optical depth. The optical depth is monitored during the experiment using a weak 795-nm beam scanning across the D1 resonance of Rb. An electro-optic modulator (EOM) driven by a function/waveform generator is used to make square pulses from the signal beam for the pulsed measurement. An acousto-optic modulator (AOM) driven by another function generator is used to ramp the power of the control beam as a sawtooth wave for the measurement. . . 32
2.13 **Nondegenerate TPA** Transmission (red dots) versus detuning of the pump beam at 776 nm showing ~25 % absorption with 1.4 nW total power in the fiber. The 780 nm pump beam was tuned close to the $5S_{1/2} \rightarrow 5P_{3/2}$ ($F = 3 \rightarrow F' = 4$) transition. The solid black line shows a fit of sum of three exponentials corresponding to the accessible hyperfine states of $5D_{5/2}$ level, from which the transit time τ was extracted to be 5.3 ns. 33

2.14 **Pulsed TPA measurement:** Absorption (red dots) of the pulsed signal beam at two-photon resonance versus pulse width. Error bars indicate measurement noise (one standard deviation). An amplitude modulator is used to create square pulses of varying duration (from 5 - 200 ns) from the signal beam, and the TPA is measured for each pulse width. The peak power in the signal pulses is kept the same (5 nW) for each measurement run. The control beam is kept CW and at the same power (5 nW) for all the measurements. The experimental data agree very well with the theoretically predicted curve (dotted black line) for a transit time τ = 5 ns of the Rb atoms across the fiber core and corroborates that the response time of the system is determined by the transit time. 34

2.15 **XPS level scheme and experimental setup**(a) (b)The linearly polarized meter and circularly polarized signal beams are coupled counter-propagating into the fiber. The meter beam undergoes slight polarization rotation due to crossphase modulation from the weak signal beam. A polarizer is used at the output to select the meter polarization orthogonal to that at the input, and measured with a photomultiplier tube (PMT). An acousto-optic modulator (AOM) is used to amplitude modulate the signal at 25 kHz, and a lock-in amplifier detects the cross-phase shift imparted on the meter at the same frequency. A strong (3 mW) off-resonant vapor generation beam is also coupled into the fiber to generate the desired atomic density and optical depth. The optical depth is monitored during the experiment using a weak 795-nm beam scanning across the D1 resonance of Rb. An electro-optic modulator (EOM) is used to make square pulses of varying duration from the meter beam for pulsed measurements. 38

2.16 **XPS Measurement:** (a) Cross-phase shift (XPS) imparted on the meter beam (red dots) versus detuning from two-photon resonance. The data are shown for one continuous scan of the laser. Tens of milliradians of phase shift are observed even for detunings greater than 1 GHz from line center. The signal absorption at these detunings is < 1%. The signal power is 50 nW, and the OD in the fiber is ~50. The power in the meter beam is 2 μW. The solid black line shows the theoretical calculation taking into account the Doppler absorption profile of the atoms in the fiber core. The deviation of the experimental data from theory is due to slow drifts in the coupling and polarization maintenance of the PBGF as the laser is scanned in frequency at a rate of ~10 Hz. 39

2.17 **XPS Measurement:** Large cross-phase modulation at the few-photon level. Cross phase shift (XPS) imparted on the meter (red dots) as a function of average signal power (and average number of signal photons in a 5-ns pulse). Error bars indicate measurement noise (one standard deviation). An OD~100 is produced in the fiber for each measurement. The power in the meter beam was 10 μW for each measurement. A ~5 mrad phase shift is measured for ~16 signal photons, corresponding to ~5 aJ of energy. The solid black line shows the theoretical prediction, and the slope corresponds to an XPS of ~0.3 mrad per signal photon, which to our knowledge, represents the largest such nonlinear phase shift induced in a single-pass through a room temperature medium. 41

3.1 **Illustration of a frequency comb:** Power spectrum of a frequency comb. 45
3.2 **Pulses:** Power spectrum of pulses generated from an optical frequency comb. 46
3.3 **Schematic of ring resonator:** Illustration of ring resonator coupled to a bus waveguide. The ring resonator has radius, r, and a coupling gap, g, from ring to waveguide. The diagram shows the coupling,κ, and transmission, t, coefficients for the input and output fields of the device along with the round-trip loss factor, α. 48
3.4 **SEM of silicon nitride microresontor:** A scanning electron micrograph of a silicon-nitride microresonator resonator with a zoomed-in viewgraph of the waveguide cross-section. 52
3.5 **Illustration of a microresontor based frequency comb:** Figure shows the general scheme for generating optical frequency combs and ultra-short pulses using cascaded parametric oscillation in a high-Q silicon-nitride microresonator. Pumping with a single frequency continuous-wave laser, a wide-band frequency comb is generated. 53
3.6 **Schematic of comb generation dynamics:** Illustration of how a frequency comb is generated via cascaded four-wave mixing(FWM) in a silicon nitride microresonator. As we tune into resonance of the cavity, a single frequency pump is coupled into the microresonator and the power builds up proportional to its quality factor. When the phase matching condition is satisfied, two pump photons are converted into a signal and idler via degenerate FWM. When more power is coupled into the resonator, the signal and idler act as pumps themselves and generate mini-combs via several degenerate and non-degenerate FWM processes. 55

3.7 **Dispersion engineering for generating octave spanning comb:** Dispersion simulations for the fundamental TE mode of a silicon-nitride waveguide with the height fixed at 730 nm and widths of 1200, 1650, and 2000 nm. The dashed curve indicates the dispersion for bulk silicon nitride. 57
3.8 **Experimental setup for generating octave spanning comb:** The experimental setup used for generating an octave spanning microresonator based comb. A single-frequency diode laser centered at 1562 nm is amplified with a erbium-doped fiber amplifier (EDFA) and inject it into a nanowaveguide using a lensed fiber. The input polarization is adjusted to quasi-TE using a fiber polarization controller. The output is collected with a free-space objective, fiber coupled (using FC) and sent to an optical spectrum analyser (OSA) for measuring the output spectrum. A small portion of the transmitted beam is initially also used for monitoring the optical resonance while tuning in to generate the comb. 59
3.9 **Octave spanning comb at 1550 nm:** Optical spectrum of octave-spanning parametric frequency comb generated in a silicon nitride ring resonator. 60
3.10 **Tuning:** Demonstration of tuning performance of the parametric comb. A 5-nm segment of parametric comb is monitored at various incident powers from 1.3 to 2.1 W. The frequency tuning range for this range of powers is 29 GHz, and we estimate the change in the comb spacing to be 36 MHz.. 61
3.11 **RF characterization setup:** The experimental setup used for generating an octave spanning microresonator based comb and characterizing the radio-frequency (RF) spectrum as the comb is generated. A single-frequency diode laser centered at 1562 nm is amplified with a erbium-doped fiber amplifier (EDFA) and inject it into a nanowaveguide using a lensed fiber. The input polarization is adjusted to quasi-TE using a fiber polarization controller. The output is collected with a free-space objective, fiber coupled (using FC) and sent to a wavelength division multiplexer (WDM) to filter a 9-nm section of the comb spectrum that does not include the pump wavelength. The filtered portion is detected by a fast photodiode, and the electrical signal is sent to an RF spectrum analyzer. We simultaneously monitor the remaining spectrum using an optical spectrum analyzer (OSA). 62

3.12 **RF dynamics:** (a) RF noise spectral of parametric frequency comb. A 9-nm portion of the optical spectrum is filtered from the comb for RF measurement. The noise is measured at four different pump detunings over 10 GHz as the pump is tuned into the cavity resonance. (b)-(e) show the corresponding optical spectra after the 9-nm section is filtered. 63
3.13 **Dispersion engineering for 1-μm comb:** Simulated dispersion curves for the fundamental TE-mode of a silicon-nitride waveguide with 600-nm height and with widths of 900, 1000, 1100, and 1200 nm. 65
3.14 **Comb dynamics:**(a-e) Comb generation dynamics (from top to bottom). As the power oscillating inside the microring increases and threshold is reached, cavity modes which are maximally phase-matched experience gain and grow. When the pump is tuned deeper into resonance and power in the side modes increase further, cascaded four-wave mixing takes place, leading to multiple cascaded oscillations and development of a wide bandwidth comb. (f) Optical spectrum of frequency comb generated pumping at 1064-nm. The comb spans 97.3 THz with a spacing of 230 GHz. (g) A zoomed in spectrum of the higher wavelength end. Comb teeth do not appear at every FSR due to lack of proper phase-matching and power buildup. 66
3.15 **Dispersion engineering for fully-filled 1-μm comb:**(a) Simulated dispersion curves for the fundamental TE-mode (dashed yellow) and TM-mode (solid red) of a silicon-nitride waveguide with 725-nm height and 1000-nm width. (b) Broadband frequency comb at 1 micron spanning 55 THz and 230-GHz comb spacing. (c-d) Zoomed in of low wavelength and high wavelength region of the frequency comb showing fully developed comb lines at every cavity mode. 69
3.16 **Microresonators designs for low-repetition rate combs:**(a, c, e)Figure shows micrographs of spiral resonators and the corresponding optical frequency combs. (b, d, f) Optical spectrum of frequency combs with FSRs of 20-, 40-, 80-GHz are shown. 71
3.17 **Intensity autocorrelator:** Schematic of an intensity autocorrelator. 73

3.18 **Experimental setup for spectral and temporal characterization:** Figure shows the experimental setup for simultaneous spectral and temporal characterization of a microresonator-based optical frequency comb. The pump wave is derived by amplifying a single-frequency tunable diode laser at 1560 nm to 2.5 W using an erbium-doped fiber amplifier (EDFA) and coupling it into the bus waveguide using a lensed fiber. A 4-*f* shaper is used to filter a 25-nm section of the comb. The optical spectrum of this 25-nm section is measured using an OSA. This signal is then sent to an intensity autocorrelator for temporal characterization. An electronic spectrum analyser (ESA) was used to measure the RF spectrum. 76

3.19 **SEM of microresonator and spectrum of generated comb:** (a) A scanning electron micrograph of a silicon-nitride resonator of length 1.44 mm coupled to a bus waveguide. The free-spectral range (FSR) is 99 GHz. (b) Optical spectrum of 99-GHz FSR frequency comb. (c) Micrograph of a silicon-nitride microresonator resonator of radius 112-μm with an FSR of 225 GHz. (d) Optical spectrum of a 225-GHz FSR frequency comb. 78

3.20 **Autocorrealtion of 99-GHz-FSR comb:**(a) Filtered optical spectrum of a 99-GHz FSR frequency comb. The filter bandwidth is 25 nm. (b) Normalized autocorrelation trace of the pulse train obtained from the filtered comb. The pulse separation is 10.1 ps. (c) Zoomed-in view of a single pulse with a 147-fs FWHM pulse width. (d) Autocorrelation traces of pulses undergoing additional dispersive propagation through additional lengths of SMF. The observed broadening is consistent with that associated with coherent pulses. 79

3.21 **Autocorrelation of a 225-GHz-FSR comb:**(a) Filtered optical spectrum of a frequency comb with 225-GHz free spectral range. (b) Normalized autocorrelation trace of pulse train obtained from the filtered comb. The pulse separation is 4.44 ps and the FWHM pulsewidth is 205 fs. 80

3.22 **Spectral and temporal dynamics:** (a) From top to bottom, pulse formation dynamics as the laser is tuned into resonance of the microresonator, thereby increasing the power coupled into the microresonator. (b) RF amplitude noise corresponding to each stage of pulse formation shown in column a to its left. (c) Optical spectrum of comb generation dynamics. Full comb is represented in blue, the filtered section of the comb used for pulse generation is shown in red. 82

3.23 **Time dynamics using time magnification technique:** (a) Single-shot characterization of temporal evolution (top to bottom) of pulses generated in a microresonator with 99-GHz FSR measured with an ultrafast temporal magnifier and a real-time oscilloscope. (b) Spectral evolution of the generated frequency comb as the pump is tuned into resonance and the power inside the microresonator increases. 85

4.1 **Silicon nitride waveguide for evanescent interaction with rubidium:** (a) Illustration of waveguide design. The silicon nitride waveguide is 400 nm in width and 200 nm in height. (b) Optical mode profile of the of waveguide showing 13.2% light outside such that interaction with Rb is possible. 88

4.2 **Schematic of Rb-chip experimental setup:** Photograph of the cell-chip unit. A small glass dome is bonded to a chip with waveguides fabricated on it. The cell-chip is then evacuated by a turbo pump through the small glass stem. Rubidium is then loaded via the same stem, and the cell-chip is sealed by heating and pinching off the stem. The coupling ends of the waveguide lie outside the dome, enabling simple coupling to the waveguides via an objective or a fiber lens. The vapor density inside the cell is regulated using a small oven that does not interfere with external objectives or fiber lenses. 89

4.3 **Waveguide transmission:** Transmission spectrum of the waveguide showing evanescent optical interaction with Rb. 91

5.1 **Schematic for optical isolation via Bragg scattering four-wave mixing (BS-FWM) in a silicon-on-insulator platform:** In the BS-FWM process, the two pumps form a grating from which the signal can scatter off depending on its propagation direction. (a) When the signal is counter-propagating with respect to the pump waves (P1 and P2), the BS-FWM process is not phase matched, and the signal passes unattenuated. (b) When the signal co-propagates with the two pumps, the phase matching condition is satisfied and the signal is extinguished generating an idler. With appropriate filters, the two pumps and the generated idler can be removed for the system to work as an isolator. 95

5.2 **Schematic of the experimental setup:** WDM-wavelength division multiplexer, PC-polarization controller, EDFA-erbium doped fiber amplifer, TBPF-tunable bandpass filter, OSA-optical spectrum analyzer. 96

5.3 **Optical spectrum of Bragg scattering in a Si waveguide:** (a) Measured optical spectra showing Bragg scattering in a Si nanowaveguide with 720-nm width and 300-nm height with pump waves centered at 1555.7 nm and 1535.5 nm and signal at 1567.5 nm. The idler is generated at 1587.9 nm. (b) Optical spectra of the signal (for which the background from the SPM of the two pumps has been removed along with the ASE of the EDFA) showing 9 dB isolation ratio. 97
5.4 **Tuning:** (a) Measured optical spectra showing Bragg scattering in a Si nanowaveguide with pump waves centered at 1554.1 nm and 1536 nm and the signal at 1582.3 nm. The idler is generated at 1601.7 nm. The red curve is the spectra in the absence of pump 1 whereas the orange curve corresponds to the case of both pump waves. (b) Optical spectra of the signal showing a 4 dB isolation ratio. (c) As the signal is tuned, the idler is simultaneous tuned while maintaining the isolation ratio. The isolation bandwidth is 8 nm corresponding to ~1 THz. 99
5.5 **Experimental setup:** Schematic of the experimental setup for measuring the forward and backward direction of the isolator simultaneously. (a) Forward direction for isolator: The pump and the signal travel counter-propagating to each other. A circulator on either side was added to the setup to simultaneously couple the signal and pumps from each side of the silicon chip. The signal is sent through port 2 via port 1 of the circulator on the right side of the chip. It is measured on port 3 of the circulator on the left side of the chip. (b) Backward direction for isolator: The pump and the signal travel co-propagating to each other. The signal and pumps were temporally overlapped and sent into the chip through port 2 via port 1 on the left side of the chip. The output was measured on port 3 of the circulator on the right side of the chip. 101
5.6 **BS-FWM based isolator:** Measured optical spectrum of the signal travelling in the forward and backward through the BS-FWM-based isolator. In the forward direction, the transmission of the signal through the waveguide is shown in red in the absence of pumps. In the presence of counter-propagating pumps, the signal(shown in yellow) travels unattenuated, while in the backward direction the signal (shown in blue) gets converted to an idler via BS-FWM, hence is extinguished by ~7 dB. The signal shown in green is measured when the pumps are turned off in co-propagating scheme such that no BS-FWM can occur. The difference of ~3 dB between the signals shown in green and red is due to the difference in coupling loss on either side of the chip. 102

6.1 **Optical switching using silicon nitride microresonator:** Illustration of bistable behavior for an s-shaped intensity response function. 107
6.2 **Phase noise measurement:** Schematic of experimental setup for measurement of phase noise. 110

CHAPTER 1

INTRODUCTION

1.1 Nonlinear optics in nanophotonic structures

Nonlinear optics (NLO) is the branch of optics that describes the behavior of light in nonlinear media, that is, media in which the dielectric polarization **P** responds nonlinearly to the electric field **E** of the light. This nonlinearity is typically only observed at very high light intensities (values of the electric field comparable to inter-atomic electric fields, typically 10^8 V/m) such as those provided by lasers. Up until the invention of the laser in the 1960s, research in this field was mostly theoretical. With the development of the pulsed laser technology, most of the earlier experiments were conducted in crystals [1] and in strongly resonant atomic vapours [2]. While silica optical fibers afforded the scientific community a low-loss (< 0.2 dB/km) [3] medium and provided an effective length of several kilometers for nonlinear optical interactions. Additionally, the strong confinement of light in the core of the fiber led to high peak intensities which, combined with the long interaction length, compensated for the weak nonlinearity of the strongly non-resonant, centro-symmetric medium of fused silica, and led to the suitability of optical fibers as a viable system to study nonlinear optical phenomena [4]. The strength of the nonlinearity in silica optical fibers depends linearly on the inverse of the effective modal area, as well as on the pump power launched [4]. The strong confinement of the electromagnetic field in the core lowers the threshold for nonlinear optical interactions. However, most of the nonlinear optical experiments were carried on using a high peak-power pulsed pump source [6, 7, 8, 9], as the power requirements

on continuous-wave (cw) lasers was unrealistic, namely in the tens to hundreds of Watts. Advances in micro- and nano-fabrication technologies has opened up the field of nonlinear optics to new and emerging device platforms comprised of micro- and nano-photonic structures such as photonic bandgap fibers, silicon waveguides, silicon-nitrite microresonators, microstructured fibers, diamond NV-centers etc. These structures allow for further confinement of light than silica optical fibers, thus allowing high nonlinear efficiency at lower powers.

This thesis focuses on studying and demonstrating nonlinear optical phenomena in micro-fabricated structures broadly classified into two genres. The first set of studies employs photonic bandgap fibers (PBGFs), the hollow core design of which facilitates confinement of atoms in addition to photons [10, 11, 12, 13, 14, 15]. This unique attribute affords a window into understanding atom-photon interactions in a controlled environment and demonstrate few-photon level nonlinear optics in such a system for the first time. The second part of this thesis focuses on various studies pertaining to optical frequency combs generated using micro-resonators fabricated in silicon nitride. Leveraging the degrees of freedom afforded by the choice of material platform and tailoring the geometries of these devices to engineer the photon dispersion at multiple wavelengths enables one to efficiently and reliably generate frequency combs. This thesis focuses on utilizing the technology developed till date to investigate the temporal dynamics associated with formation of these comb lines and onset of mode-locking in the same. The following subsections throw more light and serve as an introduction to subsequent chapters that describe these experiments in great detail.

1.1.1 Photonic bandgap fibers: Few-photon nonlinear optics

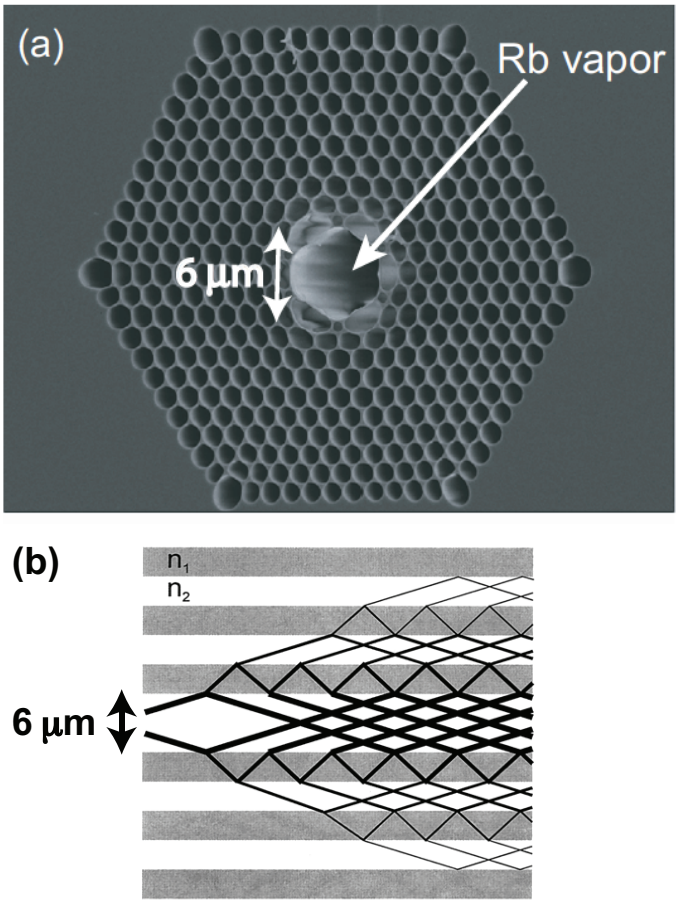

Figure 1.1: **Photonic bandgap fiber:** (a) Transmission electron microscope image of the cross section of the fiber (AIR-6-800 fiber from NKT Photonics [35]) used in these experiments. The core diameter is 6 μm and the fundamental mode area is ~10 μm^2 for the guided optical field. (b) Schematic of how light is guided in the fiber via optical interference [17].

Hollow-core PBGFs consist of a Bragg structure surrounding an empty core, typically a few microns in diameter. The core supports guided mode propagation for many tens of meters. This architecture confines both the atoms and photons to a small transverse area, which permits weak fields to interact strongly with the atoms over a length that is much larger than the Rayleigh diffraction length for a focused beam of a similar spot size. The concept of a photonic

bandgap is exactly analogous to the energy bandgap that arises for electron transport in a periodic crystal. The atomic lattice for the electronic case is replaced by a periodic refractive index variation for the photonic case.

Using this principle, it was proposed [16] and demonstrated [17] that light can be guided in a low-index region surrounded by a Bragg structure as show in Fig. 1.1. Hollow-core PBGFs are made using the stack and draw technique where hollow glass capillaries are stacked together, seven capillaries from the center are removed and the remaining structure is fused and drawn into fibers. The drawn fibers maintain the aspect ratio of the original structure and display a bandgap determined by the spacing (pitch) of the air-holes and the refractive index contrast. These fibers can also be dispersion-engineered and show very low nonlinearities from the silica structure itself because most of the light (> 92%) is confined to the hollow core [18].

Such PBGFs find applications [19] such as supuercontinuum generation, PBGF-based sensors, PBGFs for for mid-and far-infrared guidance, PBGF-based laser and amplifiers, etc., and allow for the ability to control light with light at ultralow powers. The geometry offers the prospect of exploring few-photon nonlinear interactions since both the atoms and the optical fields are transversely confined to a region that is a few wavelengths in size. This has been a major avenue of research in optics with applications in communications, computation, and signal processing. The building blocks for logic operations or single-photon switches, where one photon controls the passage of another photon through a medium, have useful applications in the development of quantum information networks. For example, the presence of one photon may cause another photon to be absorbed in a medium, which is otherwise transparent to that photon.

Such a system that absorbs two photons when they are simultaneously present but not each one separately has been theoretically proposed in an atomic vapor medium employing resonant nonlinearities and quantum interference [20]. For all optical swtiches to compete with existing electronic switches, there is a need for developing optical devices operating at the level below hundreds of photons since the total energy per logic operation for current electronic transistors are at the femtojoule level [21].

Further, such switches would have applications in the processing of quantum-entangled states, such as the generation of three-fold entangled or GHZ states [22]. A strongly two-photon absorbing medium that absorbs two photons but not one can also be used to suppress failure events in a linear-optics approach to quantum computing [23], due to the quantum Zeno effect [24]. Such a medium would also allow the construction of deterministic universal logic gates for quantum computation, like the (SWAP) and controlled-NOT (cNOT) gates, using simple elements like evanescently-coupled optical fibers without the need for ancillary photons or high-efficiency detectors [24]. Further, even heralded single photon sources can be built using such media with large two-photon absorption [25]. Classical logic gates and all-optical switches can also be implemented using these same concepts [26]. The ability to measure properties of a light field without destroying it (non-demolition measurement) is a key requirement of many quantum communication and computation protocols. A medium with a large third-order nonlinearity can be employed for QND measurement of the photon number via the optical Kerr effect [27]. A probe wave propagating through the medium experiences a nonlinear optical phase shift proportional to the intensity (i.e., the number of photons) of a signal wave. By measuring the phase of the probe at the output through balanced homodyne

detection, the signal photon number can be determined. It has been proposed that a Kerr medium with an exceptionally strong nonlinearity such that a single signal photon produces a π-radian phase shift of the probe wave, can be used to build a quantum-optical Fredkin gate [28]. Such an optical Fredkin gate would be a reversible logic gate that dissipates no energy, closely related to the universal cNOT gate in quantum computing. Although the feasibility of realizing a single-photon π-phase shift remains an issue [29], weaker Kerr nonlinearities that mediate interactions between photons through a strong coherent light field may also have useful applications in quantum optical information processing. A unified approach to quantum communication and computation has been recently proposed employing QND measurements of photons and robust distribution of quantum information through intense laser fields [30]. Such a protocol may be more feasible in terms of practical resources and the potential for scalability to many qubits.

All these approaches require the realization of systems that can achieve appreciable nonlinearities at the single-photon level and the development of schemes that can optimally exploit their nonlinear response, i.e. where the frequencies of the interacting light modes and the energy levels of the medium facilitate strong light-matter coupling [20, 43, 32, 33]. In view of this, resonant nonlinearities in atomic vapors are natural choices for exploring optical interactions at ultralow power. Alkali-metal vapors such as rubidium (Rb) enable strong light-matter interactions due to the large cross section per atom and the well-defined energy level structure [34]. Incorporation of such atomic vapors with micro-fabricated optical fibers offers the advantage of possible integration with modern optical communication systems.

Exploiting the advantages of the photonic bandgap fiber material platform, this thesis focuses on the first experimental demonstration of few-photon level two-photon absorption in Rb-filled hollow-core PBGFs. Through these experiments, the potential of this Rb-PBGF system for exploring quantum nonlinear optics at ultralow powers has been demonstrated.

1.1.2 Silicon nitride microresonators: Frequency comb generation

The field of silicon photonics has progressed by leaps and bounds in the past decade due to the constant advances in fabrication technologies, so much so that integrated photonics has been suggested as a possible solution for high-speed communication and energy efficient technology for replacing the existing electronic switches and transistors [21]. Silicon photonics seeks to unify the high bandwidth of optical communications with complimentary metal-oxide-semiconductor (CMOS) microelectronic circuits. One of the limiting factors for optical communications has been the high costs associated with both integration and exotic materials (III-V). Using CMOS-compatible materials, which are abundant and cheap, we can leverage the mature processing technology of the microelectronics industry to overall reduce the cost for the technology. CMOS compatible materials such as silicon-based nonlinear devices have already enabled high-speed data processing [36], parametric amplification [37], signal regeneration [38], demultiplexing [151], and utlra-fast signal detection [40].

Nano-fabricated devices such as silica microtoroids[41], silica microspheres [42], and Silica microfiber [43], MgF_2 and CaF_2 microresonators [44, 45, 46], have

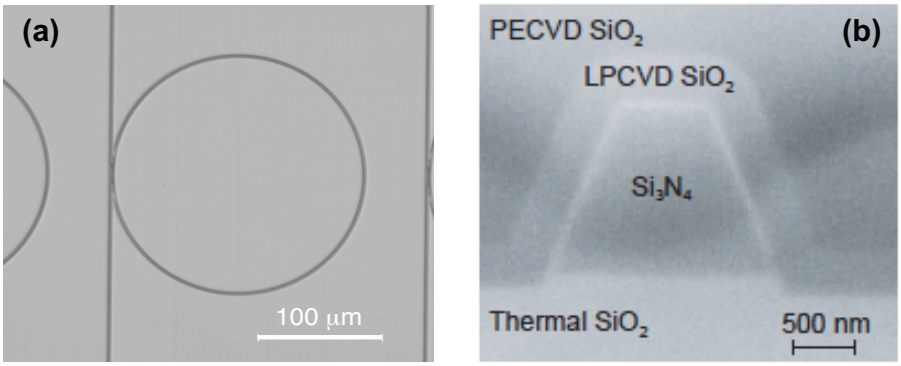

Figure 1.2: **Silicon nitride microresonator:** (a) A scanning electron micrograph of a silicon-nitride microresonator resonator of radius 112-μm with a free spectral range (FSR) of 225 GHz. (b) Micrograph of the waveguide cross-section.

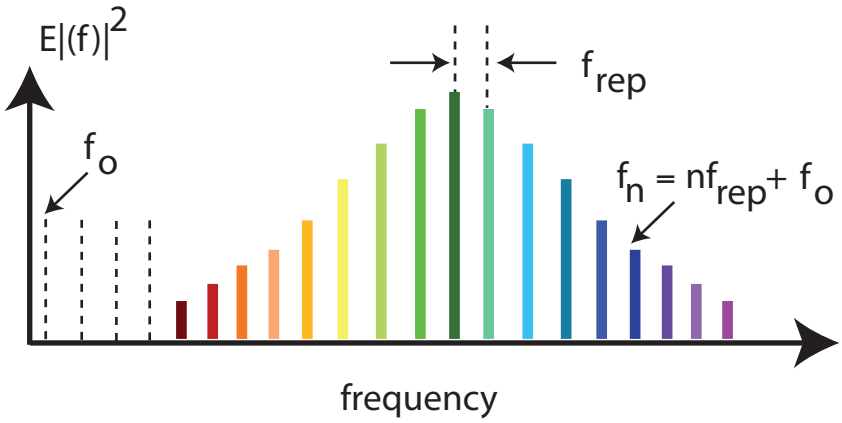

Figure 1.3: **Illustration of a frequency comb:** Power spectrum of a frequency comb.

recently found new footing in starkly different set of applications. One such application is that of optical spectroscopy which attracted attention of generations of scientists, starting with Fraunhofer's discovery of dark lines in the sun spectrum in 1814 followed by work of Kirchho and Bunsen in 1859, who explained these lines as absorption of light in atoms and molecules. Optical spectroscopy necessitates the need of a precisely calibrated frequency ruler or a frequency comb per say. An optical frequency comb consists of a discrete series

of "comb" lines which are equally spaced by the repetition frequency, f_{rep}. It is characterized by the carrier envelope offset frequency and the comb spacing or the repetition rate. Figure 1.3 shows an illustration of the power spectrum of a generic frequency comb. Since the combs lines have a frequency in the optical domain, but the repetition rate is in the microwave domain, it can act as a link between microwave and optical frequencies [47, 89, 90]. The invention of optical frequency combs using supercontinuum generation and fiber lasers in the last decade has revolutionized the field of spectroscopy and paved the way for ground-breaking measurements at previously unattainable accuracy, which has been rewarded with the Nobel Prize in 2005 [47]. Frequency combs have also spread into a variety of research fields and find application in precision spectroscopy, optical clocks, chemical sensing, distance measurements, astrophysical spectrometer calibration and many other applications [152]. While supercontinuum based frequency comb technology is robust and mature, the thrust for miniaturization and building bench top on-chip devices has led to the discovery of microresonator based optical frequency combs utilizing ultra-broadband cascaded four-wave mixing (FWM) [49]. While the full dynamics of comb generation is highly complex and resonator specific, the fundamental mechanism is shared by all geometries.

This thesis focuses on the studies pertaining to the spectral and temporal characterization of frequency combs generated in silicon nitride microresonators, as shown in Fig. 1.2, specifically tailoring the device geometry to independently control the free-spectral range of the frequency combs and dispersion engineer to generate combs pumping at different optical wavelengths and investigating the temporal dynamics associated with formation of these comb lines and onset of mode-locking.

1.2 Thesis layout - chapter overview and collaborative work

The results of the author presented in this thesis were to a large extent performed in collaborative work with her colleagues. This dissertation is divided into four parts. In what follows the results of the individual chapters are given and the relative contributions indicated.

Chapter 2 describes various experiments that demonstrate the potential of the Rb-PBGF system for exploring quantum nonlinear optics at ultralow powers. In this chapter, the Rb-filled PBGF system is discussed in detail with applications to degenerate and non-degenerate two-photon absorption at a few photon level. Following which the demonstration of cross-phase modulation in the same setup has been discussed. In this chapter the author has designed and implemented the experimental infrastructure jointly with her colleague Vivek Venkataraman. The simulations for the degenerate and non-degenerate two-photon absorption were performed by the author, while the experiments were carried out jointly. The cross-phase modulation experiment was conceived and designed by Vivek while the experiment and data analysis were jointly carried out by Vivek and the author.

Chapter 3 describes the second class of material platform used for nonlinear optics i.e. silicon nitride microresonators. This chapter includes detail discussions of the comb generation process, first demonstration of an octave spanning frequency comb using this platform, dispersion engineering and temporal dynamics including mode-locking. The work presented in this chapter has been in collaboration with Prof. Michal Lipson's group in the School of Electrical and Computer Engineering at Cornell University. Jacob Levy from the Lipson group

fabricated the silicon nitride microresonators which were used to characterize the spectral and temporal dynamics of the frequency combs, demonstrate the octave spanning comb and one-micron combs. The author implemented these experiments jointly with her colleague Dr. Yoshitomo Okawachi.

Chapter 4 discusses a potential route for integrating Rb with the silicon microresonators and its potential applications. The experiment were conceived, designed and implemented jointly with Dr. Pablo Londero. The microresonators were fabricated by Jacob Levy from the Lipson group.

Chapter 5 describes an application of nano-fabricated silicon waveguides for building on-chip optical isolators using Bragg scattering four-wave mixing. The experiment was conceived and experimentally demonstrated in highly nonlinear fiber by Dr. Yoshitomo Okawachi and Dr. Onur Kuzucu. The work presented in this chapter has been carried out in silicon nanowaveguides which were fabricated by Dr. Michal Menard from the Lipson group while the experiments was performed by the author.

Chapter 6 provides a summary and discussion of possible future experiments that may be investigated using both systems.

CHAPTER 2

FEW-PHOTON NONLINEAR OPTICS IN RB-FILLED PHOTONIC BANDGAP FIBER

2.1 Introduction

In this chapter, we show that two-photon absorption (TPA) in Rb atoms can be greatly enhanced by the use of a hollow-core photonic bandgap fiber. We investigate off-resonant, degenerate Doppler-free TPA on the $5S_{1/2} \rightarrow 5D_{5/2}$ transition and observe 1% absorption of a pump beam with a total power of only 1 mW in the fiber. These results are verified by measuring the amount of emitted blue fluorescence and are consistent with the theoretical predictions which indicate that transit time effects play an important role in determining the two-photon absorption cross-section in a confined geometry. Furthermore, by employing a near-resonant, non-degenerate two-photon transition in Rb, we demonstrate all-optical intensity modulation with just a few photons (<20) on average or only a few attojoules of energy, at relatively large bandwidths (~50 MHz). Finally, we produce relatively large cross-phase shifts of a few milliradians on a meter beam with < 20 signal photons by tuning slightly away from resonance on the same non-degenerate two-photon transition. This corresponds to a phase shift of 0.3 milliradian per photon, with a response time of < 5 ns.

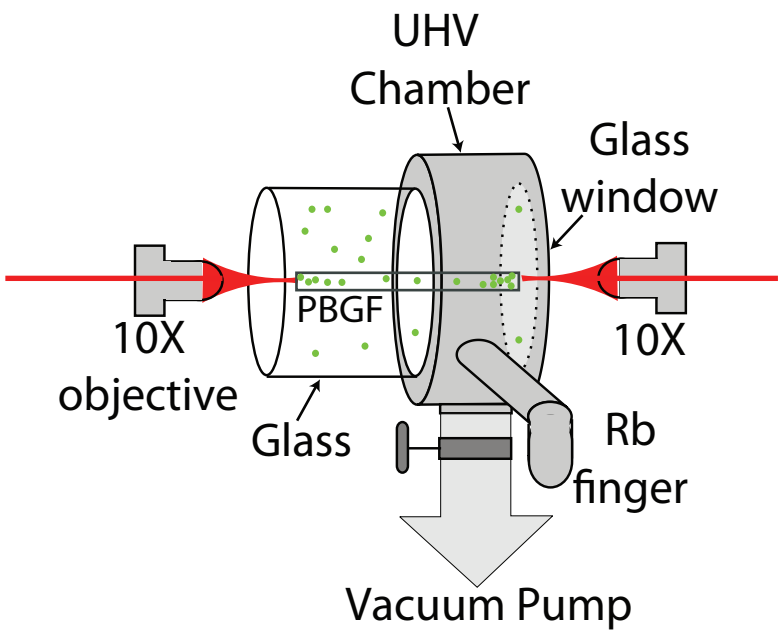

Figure 2.1: **Schematic of vacuum chamber:** Schematic of the vacuum chamber used for TPA. The Rb-PBGF system consists of an ultra-high vacuum (UHV) chamber with a Rb source attached, inside of which one or more PBGFs are mounted. On one side of the ultra high-vacuum (UHV) compatible stainless steel chamber, a cylindrical glass tube is attached which provides optical access to all sides of the fiber. Glass windows on either side allow for coupling into and out of either end of the fiber(s).

2.2 The system

The Rb-PBGF system consists of an ultra-high vacuum (UHV) chamber with a Rb source attached, inside of which one or more PBGFs are mounted as shown in Fig. 2.1[50, 51]. We modified the design of the previously used Rb-PBGF system [52, 53] to allow us to image the fibers from the top and collect the emitted fluorescence. On one side of the ultra high-vacuum (UHV) compatible stainless steel chamber, a cylindrical glass tube is attached which provides optical access to all sides of the fiber. Glass windows on either side allow for coupling into and out of either end of the fiber(s). To minimize the loss of Rb atoms to surfaces and

to hasten the ripening process two things must be ensured: 1) the available surface area is the bare minimum possible and 2) before introducing Rb, the UHV chamber is thoroughly cleaned using ultrasonication and then baked out for a few days to remove any residual oxygen and water molecules. After initial bake-out of the chamber at 150-200°C for 3-4 days to reach a background pressure $<10^{8}$torr, an ampoule of Rb sitting inside a steel appendage (cold-finger) to the chamber is broken. The chamber is then kept at 80-85°C, and the Rb cold-finger is kept at 50-55°C for 1-2 weeks. During this time, the chamber ripens, i.e., Rb atoms attach themselves to the inner surfaces of the chamber by chemically reacting with every available adsorbed oxygen or water molecule and any dangling OH-bonds [54]. Once every reactive site has been covered, only then will a stable, ambient Rb vapor form in the chamber. The vapor density slowly increases as the cell ripens and finally stabilizes to a value that depends on the temperature of the cell and the Rb cold-finger. Once the vapor density (monitored through a weak laser scanning across the absorption lines) reaches a steady-state value, the temperature of the chamber and cold-finger are brought down to ~60°C and ~40°C, respectively, for normal operation. Atoms from the ambient Rb vapor then start diffusing down the hollow core of the PBGF, and most of these atoms attach themselves to the inner silica walls such that there is no Rb vapor inside the fiber core under steady-state conditions. Since the surface area to volume ratio for the inside of the core of our fiber is very large, and we expect that the issues of chemical and physical adsorption on to the silica walls should be particularly severe. In the past, various methods for injecting atoms into the core such as dipole force based funnel beams [55] and light-induced drift based optical piston techniques [56, 57] have been considered. In the recent past, the phenomenon of light-induced atomic desorption

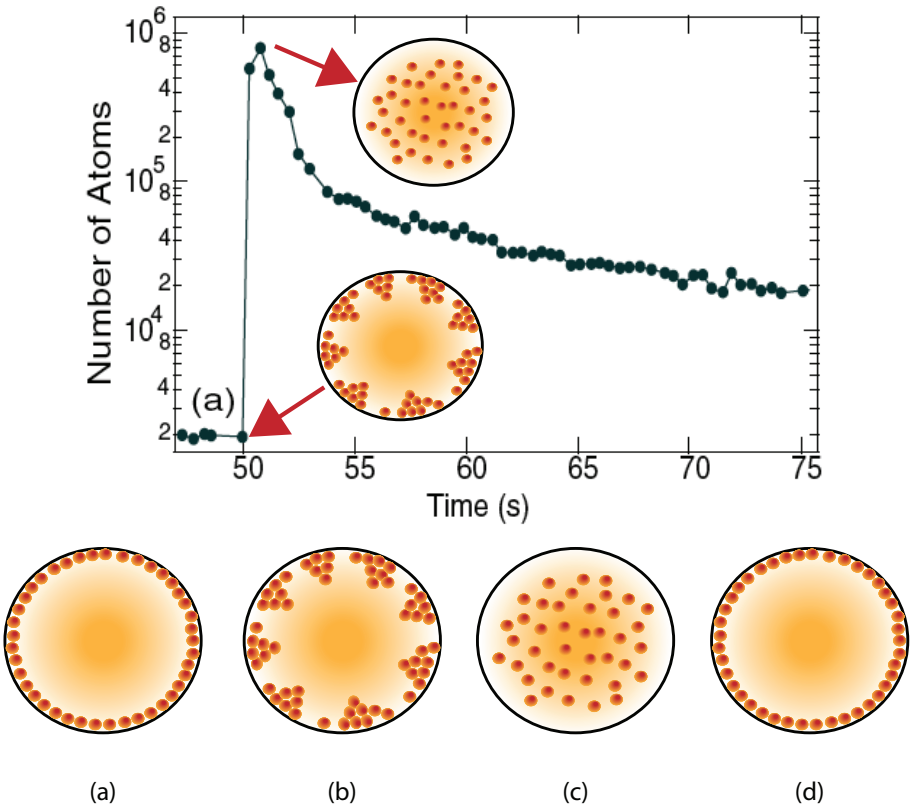

Figure 2.2: **Generation of Rubidium vapor:** Under steady-state conditions, the Rb atoms inside the PBGF core are all stuck to the inside walls of the fiber forming nanoclusters (b). A strong vapor-generation beam at ~805 nm (far detuned from the atomic transitions of Rb) coupled into the PBGF heats and evaporates the adsorbed nanoclusters, creating a vapor of Rb atoms in the core (c). The vapor density in the core is set by the generation beam power and duration. After the interaction is over the atoms collide with the walls of the fiber and coat it uniformly (a,d), until they form nanoclusters again.

(LIAD) [54, 58, 59] has been discovered in which alkali atoms adsorbed onto organic coatings are suddenly released on exposure to visible and near-infrared light in a non-thermal desorption process. However, after similar attempts to perform LIAD in Rb-filled organic material coated hollow-core photonic bandgap fiber have revealed that the wall collisional dephasing rate is quite high and the coatings do not seem to help with generation of controlled, high optical

depths. It was later reported that that alkali-atom desorption is possible from uncoated porous glass surfaces and that it may even be larger than that from hydrocarbon-coated glass [60]. This possibility was investigated in the Rb-filled PBGF system and concluded that the Rb stick to the wall of the fiber and form nanoclusters [61].

In the absence of any laser beams propagating through the fiber, the Rb atoms inside the PBGF core are all stuck to the inside walls of the fiber forming nanoclusters. In order to generate a Rb vapor inside the core, a strong (few mWs) vapor generation beam at ~805 nm (far detuned from the atomic transitions of Rb) is coupled into the PBGF which heats and evaporates the adsorbed nanoclusters [61]. The vapor density in the core is set by the generation beam power and duration [58]. As more nanoclusters are heated, the Rb vapor density inside the core increases. The vapor generation dynamics is shown in Fig. 2.2. Large atomic densities (and optical depths) of Rb inside the hollow-core of PBGFs can be generated all-optically without the need for any change in the temperature of the cell. This approach represents a fast, on-demand, controllable and repeatable technique to produce specified vapor densities for various light-matter interactions. Thus, the tight light confinement, high vapor density and long interaction length allow us to perform nonlinear optics at ultralow power [13, 50, 10, 52, 53, 61, 62, 63].

Using this system, several nonlinear interactions such as electromagnetically induced transparency (EIT) [50] and four-wave mixing using Rb-filled PBGF at ultra-low powers [53] have been demonstrated in the recent past. As mentioned earlier, TPA can provide a route towards building efficient single-photon switches for applications in quantum computing. We thus investigate intensity

modulation and cross phase modulation of one beam due to another in Rb-filled photonic bandgap fiber.

2.3 Two-photon absorption: Intensity and phase modulation

TPA is the simultaneous absorption of two photons from two similar or different light fields (i.e., one from each) which results in a resonant transition from the ground state to an excited state. A key feature of TPA is that it allows access to electronic states that are otherwise dipole-forbidden single-photon transitions. It also represents one of the simplest nonlinear processes that allows one to characterize the strength of the light-matter interaction and to generate novel nonclassical effects. Many interesting two-photon processes and their applications, such as all-optical switching [64], generation of single photons [25], measurement of coherence and photon statistics [65], and precision spectroscopy [66], require a significant TPA at low power levels. For example, it has been shown that the quantum Zeno effect can be used to implement optical logic gates for classical and quantum computing, where the Zeno effect is produced using a strong TPA medium [26]. Alkali atoms such as Rb have relatively large two-photon cross-sections due to near-resonant enhancement and the large oscillator strengths of their transitions. Nevertheless, TPA experiments in bulk alkali vapor cells require relatively high powers to generate measurable effects [74]. Waveguide geometries, such as hollow-core PBGFs filled with an alkali vapor or tapered optical fibers with an ambient thermal vapor of alkali atoms, can enhance nonlinear interactions greatly and significantly reduce the threshold for observing TPA. Recently, non-degenerate resonant TPA was observed at 100 nW power levels in tapered optical fibers with ambient thermal Rubidium (Rb) va-

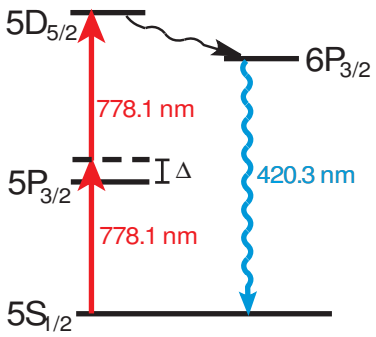

Figure 2.3: **Schematic of energy level:** Energy level structure for TPA in Rb. Δ is the detuning from the intermediate level. We observe degenerate TPA at 778.1 nm.

por, in which the light-matter interaction occurs via the evanescent wave of the guided light in the fiber [68]. This section describes the experimental observation of TPA and cross-phase modulation in a RB-PBGF system, showing several orders of magnitude improvement over previously demonstrated experiments.

2.3.1 Degenerate two-photon absorption

In this section we describe the experimental observation of efficient, Doppler-free TPA in a Rb-PBGF system using the $5S_{1/2} \rightarrow 5D_{5/2}$ two-photon transition at 778.1 nm at milliwatt power levels [69]. We estimate theoretically the amount of TPA for our system (both from direct absorption from the pump beam and from the emitted blue fluorescence) and show that our experimental results are in good agreement with the theoretical predictions. Further we obtain an estimate of the transit-time of the Rb atoms in the PBGF.

Theoretical Calculations:

An illustration of the two-photon level scheme is shown in Fig. 2.3. Once excited to the $5D_{5/2}$ level, the Rb atoms decay with 35% probability to the intermediate $6P_{3/2}$ level, and then with 31% probability back to $5S_{1/2}$ ground state emitting blue photons at 420.3 nm (see Fig. 2.3)[70]. When the pump beam (at 778.1 nm) is far detuned from the intermediate level, or when $\Delta \gg \Gamma$, where Γ is the linewidth of the intermediate level, then the process is termed off-resonant two-photon excitation. We characterize the nonlinearity of the Rb-PBGF system for this process by calculating the imaginary part of the third-order susceptibility $\chi^{(3)}_{Im}$ [71] corresponding to the relevant two-photon transition using,

$$\chi^{(3)}_{Im} = \frac{N\mu_1^2\mu_2^2}{\varepsilon_o\hbar^3\Delta^2\gamma}, \tag{2.1}$$

where N is the atomic number density, μ_1 and μ_2 are the effective detuned dipole moments for the $5S_{1/2} \rightarrow 5P_{3/2}$ and $5P_{3/2} \rightarrow 5D_{5/2}$ transitions, respectively, Δ is the detuning from the $5P_{3/2}$ level, and γ is the homogeneous decay rate of the $5D_{5/2}$ level. In the Rb-PBGF system, γ is determined by the transit time of the atoms across the micron-scale core of the fiber which is much smaller than the excited state lifetime[63].

The two photon absorption coefficient is given by

$$\beta = 0.0282 \times 10^8 \times \left(\frac{2\pi\chi^{(3)}_{Im}}{\lambda}\right), \tag{2.2}$$

where λ is the wavelength of the pump. For our system, using an OD $\sim$ 100 ($N \approx 2 \times 10^{13}$ atoms/cc), a beam waist area, $A \sim 10^{-7}$ cm^2, γ = 50 MHz [63], we estimate the value of $\chi^{(3)}_{Im}$ to be 4×10^{-10} esu and β to be 1.3×10^{-6} cm/W. Correspondingly, the two-photon scattering cross-section $\sigma^{(2)}$ is estimated to be 6.5×10^{-20} cm^4/W.

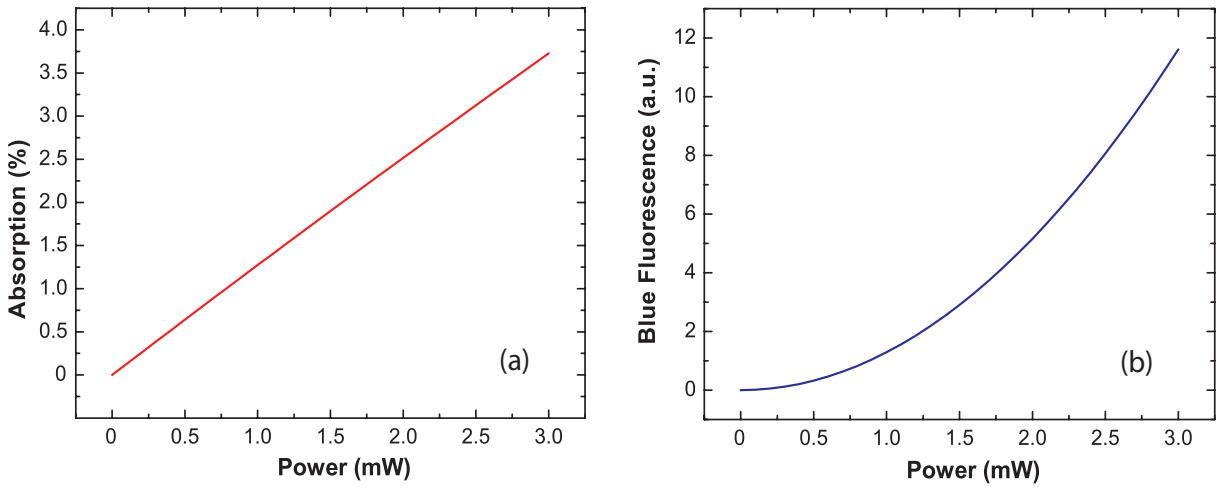

Figure 2.4: **Simulated TPA:** (a) Expected two-photon absorption versus pump power in a Rb-filled PBGF with an optical depth of 100.(b) Quadratic dependence of two-photon fluorescence on pump power in hollow-core photonic bandgap fiber.

The transmission of the beam through a medium with a second-order absorption process can be expressed as [71],

$$T = \frac{I_{out}}{I_{in}} = \frac{1}{(1 + \beta L I_{in})}, \tag{2.3}$$

where I_{in} and I_{out} are the input and output intensities of the pump beam respectively and L is the interaction length (1 cm). For $\beta L I_{in} \ll 1$, the percentage of absorption is given by

$$\left[\frac{I_{out} - I_{in}}{I_{in}} = \beta L I_{in}\right] \times 100. \tag{2.4}$$

To estimate the fluorescence power of the emitted blue light at $\lambda_2 = 420.3$ nm, we take into account the branching ratios of the transitions involved during the decay from the excited $5D_{5/2}$ level to the ground $5S_{1/2}$ level, through the intermediate $6P_{3/2}$ level as mentioned earlier. There are two possible decay mechanisms involved in the process. The first is due to a radiative decay from the $5D_{5/2}$ level, which has a lifetime τ_2 of ~240 ns, and the second is due

to a non-radiative decay resulting from collisions with the walls of the fiber with a lifetime (transit-time,τ_1) of 6 ns. Effectively, the fraction of atoms that fluoresce is $\propto \tau_1/(\tau_2 + \tau_1) \approx \tau_1/\tau_2$ [72, 73]. In addition, the decay path from $5D_{5/2} \rightarrow 5S_{1/2}$ (wavelength, $\lambda_1 = 389.05$ nm) involves the intermediate level $6P_{3/2}$. Hence we must also take into account the energy lost in the $5D_{5/2} \rightarrow 6P_{3/2}$ transition. Therefore, the total power of the blue fluorescence can be calculated from,

$$P = (I_{in} - I_{out}) \times A \times R_1 \times R_2 \times \frac{\tau_1}{\tau_2} \times \frac{\lambda_1}{\lambda_2}, \tag{2.5}$$

where $R_1(= 0.35)$ and $R_2(= 0.31)$ are the branching ratios of the $5D_{5/2} \rightarrow 6P_{3/2}$ and $6P_{3/2} \rightarrow 5S_{1/2}$ transitions, respectively. Using Eqs. (2.4) and (2.5) we get,

$$P = Const \times I_{in}^2. \tag{2.6}$$

Figure 2.4(a) shows the plot of absorption percentage due to TPA versus the total pump power in a Rb-PBGF system. We observe that with 1 mW power we expect to see 1% absorption, which is relatively significant for the degenerate off-resonant TPA process at such low pump powers. Further more, using Eq. (2.6) we simulate a plot of blue fluorescence versus pump power [Fig. 2.4(b)] which clearly illustrates the quadratic dependence of TPA on the pump power (and, correspondingly on the intensity of incident light field).

We next consider TPA with counter-propagating beams at 778.1 nm such that two-photon absorption occurs by the simultaneous absorption of one photon from each of the beams. The advantage of using a counter-propagating scheme is that the interaction is Doppler free[74, 75, 76]. Therefore, we expect to see only homogeneously broadened lines due to transit-time effects. The following section provides the details of the experimental setup that is used to measure the blue fluorescence and direct two-photon absorption from the pump beam.

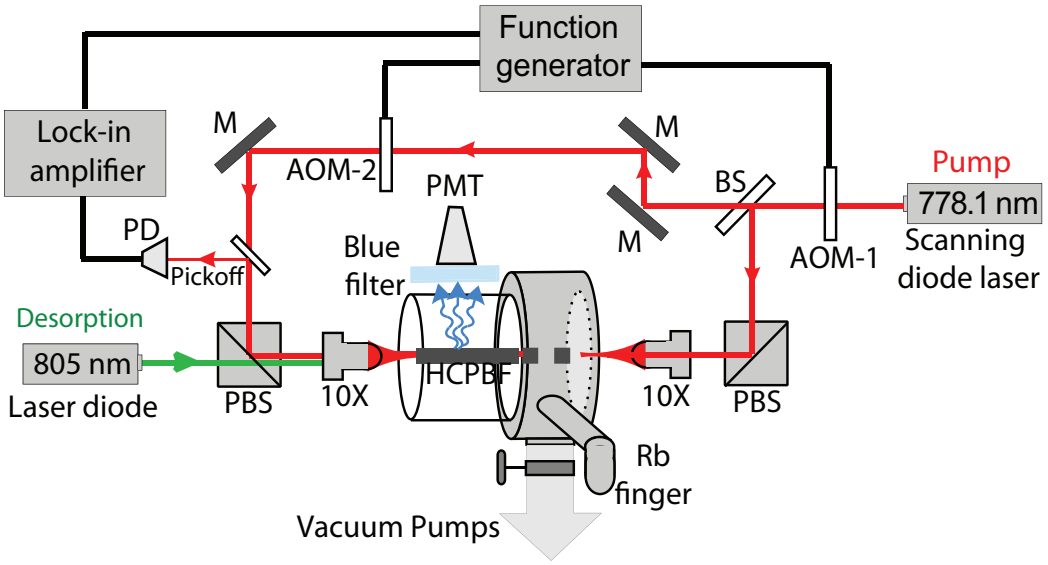

Figure 2.5: **Schematic of experimental setup for degenerate TPA:** The pump laser is split into two counter-propagating beams using a 50/50 beamsplitter (BS). The polarizations are made identical using polarization beam splitter (PBS) cubes, and the beams are then coupled through the hollow-core photonic bandgap fiber (PBGF). A blue colored glass is used to filter the fluorescence from the excited $6P_{3/2}$ state and then detected on a photomultiplier tube (PMT). An acousto-optic modulator (AOM-1) is used modulate the pump beams as a triangular wave at a 1-kHz frequency to vary linearly the intensity from 'x' to '4x' of the counter-propagating beams simultaneously. For lock-in detection of the TPA through the PBGF, one of the two counter-propagating beams is modulated using AOM-2 as a square wave at 25-kHz. The signal is detected on a photodiode (PD) using a pick-off beam at one end and sent to a lock-in amplifier, the ouput of which is subsequently monitored using an oscilloscope.

Experimental setup:

A schematic of the experimental setup is presented in Fig. 2.5. We use the Rb-PBGF system as described before with 9-cm-long and 6-μm-diameter hollow core photonic crystal fibers (Crystal Fiber, AIR-6-800) that guides light over the range of 750-810 nm wavelengths. The temperatures of the chamber and the cold-finger (Rb source) are maintained at 85°C and 55°C, respectively. The beam from an external cavity diode laser at 778.1 nm, scanning mode-hop free across 5 GHz (over the two-photon resonances), is split into two counter-propagating beams using a 50/50 beam splitter (BS) and are each coupled to opposite ends of the fiber using 10x objectives. The two beams have equal powers and identical polarizations.

To generate the desired OD ($\sim$ 100), a highly off-resonant 20-mW desorption beam at 805 nm is also coupled into the fiber with a polarization orthogonal with respect to the pump beams. The design of our chamber enables us to collect a part of the emitted blue photons from the top. The blue photons are filtered using a blue colored glass filter and detected by a photomultiplier tube (PMT, Hamamatsu H7422P-40). The signal is then monitored and recorded for 1 second using an oscilloscope.

We measure the TPA as a function of the intensity of light field using an acouto-optic modulator (AOM-1) (see Fig. 2.5) to vary the intensity of the two-counter propagating beams simultaneously from 'x' to '4x' using a triangular wave at 1-kHz. The emitted blue photons are collected and detected from the top of the fiber by the method described before. For direct measurement of TPA from the 778.1 nm pump beams, we perform a lock-in detection by using another acousto-optic modulator (AOM-2) to modulate one of the two counter-

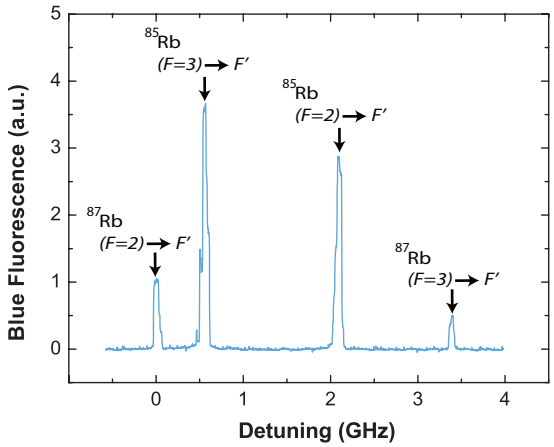

Figure 2.6: **TPA measurement through fluorescence:** Blue fluorescence signal detected by the PMT. Fluorescence peaks corresponding to each of the hyperfine ground states of ^{85}Rb and ^{87}Rb are observed as the pump laser is scanned in frequency. Since the two beams are perfectly counter-propagating in the fiber, all the peaks are Doppler-free. The peaks are homogeneously broadened due to the short transit time (~5 ns) of the Rb atoms across the 6 – μm core of the fiber.

propagating beams. A weak reflection of the foward propagating beam is collected from one end using a photodiode, and it's output is then sent to a lock-in amplifier. The resultant output is then recorded using an oscilloscope.

Results and Discussion:

Measurement of Two-Photon Absorption using Fluorescence:

Figure 2.6 shows the blue fluorescence signal detected by the PMT due to TPA. The four peaks correspond to each of the two hyperfine ground states of ^{85}Rb and ^{87}Rb. We recorded the wavelength of each of the lines using a wavemeter (Burleigh WA-1600) with an uncertainty of ±0.0001 nm in each reading. For the states F = 3 and F = 2 of ^{85}Rb, the wavelengths are 778.1055 nm and 778.1025

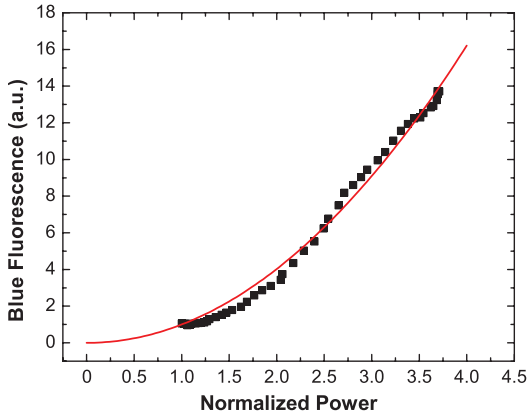

Figure 2.7: **Quadratic dependence of TPA:** Blue fluorescence signal (black dots) detected by the PMT as the pump laser power is varied using AOM-1 when the laser is tuned to the $5S_{1/2} \rightarrow 5D_{5/2}$ (F = 3 to F') two-photon transition of ^{85}Rb. The solid red line shows the expected square dependence of two-photon absorption on intensity.

nm respectively, where as 778.1067 nm and 778.0997 nm correspond to the F = 2 and F = 1 states of ^{87}Rb, respectively. The signal is Doppler free, and the line-broadening is due only to the transit-time effect. As discussed in Sec. 2.3.1, the relatively short transit time of the Rb atoms in comparison to the lifetime of the excited $5D_{5/2}$ level suppresses the number of blue photons emitted, and we estimate the total amount blue fluorescence emitted from the fiber taking into account the collection area of the PMT and assuming the fluorescence to be isotropic over the 4π solid angle. We obtain 30 nW of blue light for 1 mW of pump power, which corresponds to $\sim$ 1% absorption [using Eq. (2.5) and Eq. (2.4)]. This agrees very well with the theoretically calculated value.

We also studied the dependence of TPA on pump intensity. Figure 2.7 shows the measured blue fluorescence versus input pump power, in which the power of the two counter-propagating pump beams are varied from 100 μW to 400 μW using AOM-1. We observe that the blue fluorescence increases quadratically

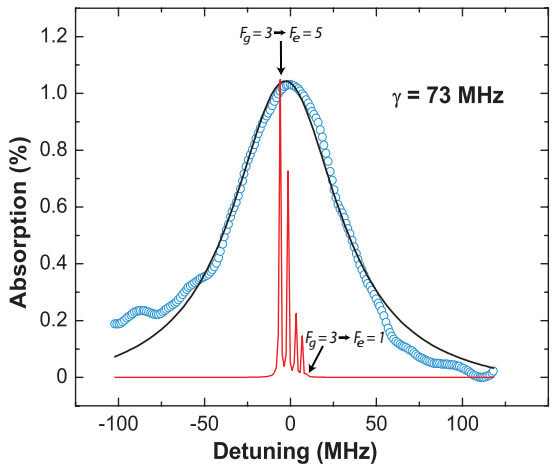

Figure 2.8: **Direct measurement of TPA:** The blue circles show the data from the direct measurement of two-photon absorption from one of the pump beams using a lock-in detector as the pump laser was scanned across the $5S_{1/2} \rightarrow 5D_{5/2}$, $F_g = 3$ to F_e (778.1055 nm) two-photon transition of ^{85}Rb. The solid black line shows a fit of a sum of five Lorentzians which correspond to each of the hyperfine lines. The homogenous linewidth is estimated to be 73 ±10 MHz.

with the intensity of the pump beams, which as expected for TPA. We have observed that there are fluctuations in the optical coupling of the pump beams while the vapor generation beam is coupled to the fiber. These fluctuations are extremely random. This can also lead to deviations in the expected amount of blue fluorescence for a given pump power from shot to shot. Further, there is some nonlinear response of AOM such that a linear volatge ramp on the AOM does not produce an exactly linear power response. This would why the data does not exactly follow the fitted quadratic curve. We experimentally determine the two-photon cross-section, $\sigma^{(2)}$, to be 5×10^{-20} cm^4/W for the ^{85}Rb $5S_{1/2} \rightarrow 5D_{5/2}$ transition, which agrees with the theoretically calculated value taking into account the short transit-time of the Rb atoms as the dominant decay rate.

Direct Measurement of Two-Photon Absorption:

Due to the enhanced TPA in Rb-PBGF system, we can directly measure and quantify the amount of absorption from the pump beams. We use a lock-in dection method since the signal to noise ratio in our system is low. AOM-2 is driven by a square wave at 25 kHz to modulate one of the counter-propagating beams. A pick-off beam from the other beam is detected using a photodiode and the output is sent to a lock-in amplifier. Figure 2.8 shows the result of our measurement, and with an input pump power of 1 mW and an OD ~ 100, we observe 1% absorption. This is in good agreement with our estimation of the amount of TPA from the experimental data of blue fluorescence measurement and with our theoretical estimation of TPA [see Fig. 2.4(a)].

The absorption lines can also be analysed to obtain a measurement of the homogeneous linewidth. We fitted a sum of five Lorentzians corresponding to the hyperfine lines ($F_g = 3$ to $F_e = 1, 2, 3, 4, 5$) of the $5S_{1/2} \rightarrow 5D_{5/2}$ transition. The estimated linewidth is 73±10 MHz, and represents a direct measurement of the homogeneous linewidth of Rb confined to a hollow-core photonic bandgap fiber. We also note that the homogeneous linewidth (which is determined by transit-time broadening) is slightly different from system (Rb-HCPBF) to system[63]. This might be due to the fact that desorption (which is used to generate the Rb vapor) occurs at a slightly different power levels and hence the corresponding temperatures and therefore the thermal velocities of the Rb vapor are slightly different. Nevertheless, the amount of off-resonance two-photon absorption is substantially high for such low pump powers, which demonstrates the potential of the Rb-PBGF system for exploring novel classical and quantum nonlinear effects at low powers.

If we perform an on-resonance non-degenerate TPA[68], with counter-

propagating 780.2 nm and 776 nm beams, we theoretically expect to see a 10^8 enhancement over the off-resonance TPA. This is due to the fact that in Eq. 2.1, $\Delta = 0$; hence $\chi^{(3)}_{Im}$ is given by

$$\chi^{(3)}_{Im} = \frac{N\mu_1^2\mu_2^2}{\varepsilon_o\hbar^3\gamma^3}. \tag{2.7}$$

For $\gamma = 50$ MHz, $\chi^{(3)}_{Im} = 0.18$ esu and $\sigma^{(2)} = 2.9 \times 10^{-11}$ cm^4/W. This implies that one beam can experience 3 dB attenuation with 500 pW power in the other beam which corresponds to 10 photons of switching energy assuming that the pulse duration is equal to the inverse of the homogeneous linewidth. This suggests that with higher ODs, the Rb-PBGF system can be applied to realizing single-photon all-optical switching using TPA.

2.3.2 Non-denegerate two-photon absorption

The previous section provides a route towards demonstrating few photon switching using the Rb-PBGF system. In this section we describe the experimental observation of efficient, Doppler-free non-degenerate TPA at the few photon level in a Rb-PBGF system using the $5S_{1/2} \rightarrow 5D_{5/2}$ two-photon transition [86]. We estimate theoretically the amount of TPA for our system and show that our experimental results are in good agreement with the theoretical predictions.

Theoretical Estimates:

Optimum detuning and dependence on optical depth:

The level scheme for non-degenerate TPA is shown in Fig. 2.9. Once excited to the $5D_{5/2}$ level via TPA, the Rb atoms decays to the $5S\,1/2$ ground state via the

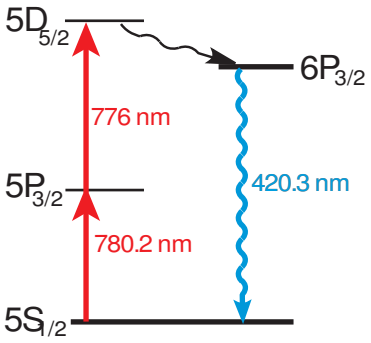

Figure 2.9: **Schematic of energy level for non-degenerate TPA:** TPA level scheme in $_{85}$Rb used for performing all-optical modulation. An atom in the ground $5S_{1/2}$ state can simultaneously absorb a photon each from the 780-nm control and 776-nm signal beams to make a resonant transition to the excited $5D_{5/2}$ state. The signal photon can only be absorbed if the control photon is also present. A small fraction of the excited atoms decay through the $6P_{3/2}$ level emitting blue fluorescence.

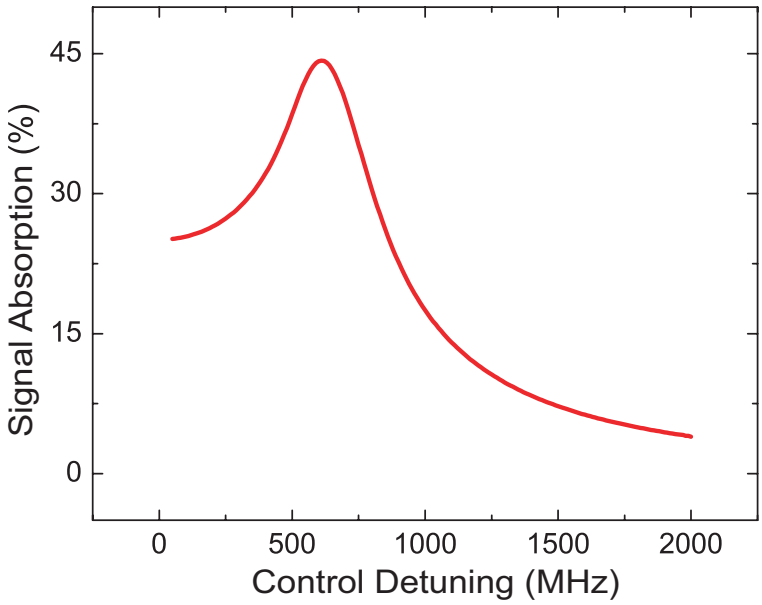

Figure 2.10: **Calculation of optimum detuning:** Optimum detuning for non-degenerate TPA. Absorption of the signal beam at two-photon resonance with varying detuning of the control beam from the intermediate $5P_{3/2}$ level.

intermediate $6P_{3/2}$ level emitting blue photons at 420.3 nm.To maximize TPA, naively one might reduce the detuning from the intermediate level Δ as much as possible to resonantly enhance the interaction. However, since the 780-nm control beam experiences ordinary linear absorption in addition to TPA, the optimal detuning for maximal TPA is non-trivial. We numerically solve the following coupled nonlinear propagation equations for the intensities I_C and I_S of the control and signal beams respectively to theoretically model non-degenerate resonant TPA in a counter-propagating geometry. We take into account the Gaussian velocity distribution of thermal atoms in the fiber,

$$\frac{dI_C}{dz} = -\alpha I_C - \beta I_C I_S, \tag{2.8a}$$

$$\frac{dI_S}{dz} = \beta I_C I_S, \tag{2.8b}$$

for $0 < z < L$, where L ~1 cm is the sample length, α is the linear absorption coefficient and β is the TPA coefficient. We assume α is given by a Doppler broadened Gaussian absorption profile as

$$\alpha(\Delta) = ODexp\left(-\frac{\Delta^2}{w_D^2}\right), \tag{2.9}$$

where OD is the optical depth on resonance for the $5S_{1/2} \rightarrow 5P_{3/2}$(D2) transition, Δ is the detuning of the control beam from line center, and w_D is the Doppler width, which is a function of the temperature of the atoms. For the Rb atoms generated in the hollow core of the PBGF, $w_D \sim 325$ MHz [62]. We compute an average β for a particular detuning Δ by integrating over the Gaussian velocity distribution of thermal atoms in the fiber. For an atom moving at velocity v, the two-photon cross-section [71] at detuning Δ is

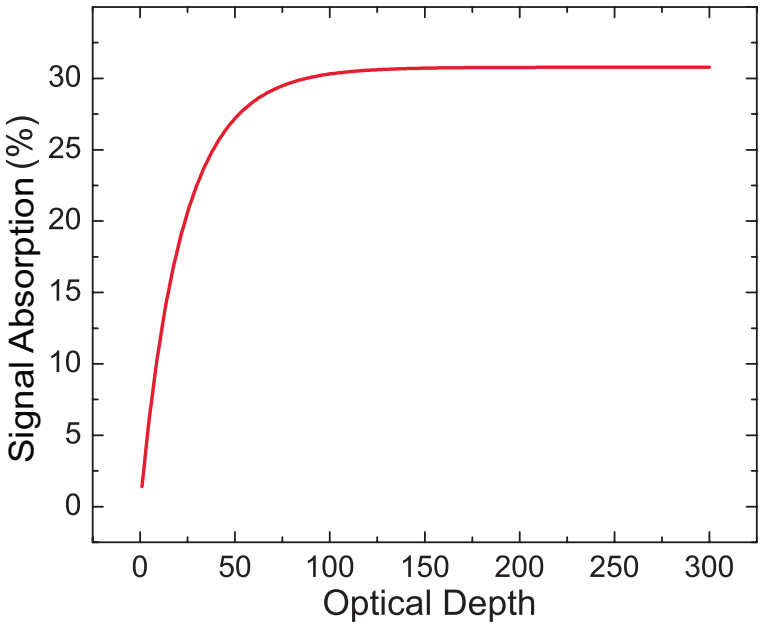

Figure 2.11: **TPA dependence on optical depth:** Absorption of the signal beam at two-photon resonance with varying atomic density.

$$\sigma^{(2)}(\Delta, v) = \frac{\mu_1^2 \mu_2^2}{\epsilon_0 \hbar^3 \gamma((\Delta - kv)^2 + \gamma^2)}, \tag{2.10}$$

where $k = 2\pi/\lambda$ is the wavenumber. The average β is computed by integrating over the thermal velocity profile as

$$\beta(\Delta) = N \int_{-\infty}^{+\infty} \sigma^{(2)}(\Delta, v) f(v) dv, \tag{2.11}$$

where

$$f(v) = \frac{1}{\sqrt{2\pi} v_D} exp\left(-\frac{v^2}{v_D^2}\right) \tag{2.12}$$

is the thermal velocity distribution, $v_D = w_D/k$ and N is the atomic density. We thus compute both the linear [$\alpha(\Delta)$] and two-photon [$\beta(\Delta)$] absorption coefficients for a particular detuning Δ and then numerically simulate the nonlinear propagation equations 2.12 to calculate the amount of TPA expected at that detuning. Figure 2.10 shows the calculated TPA as a function of the detuning from

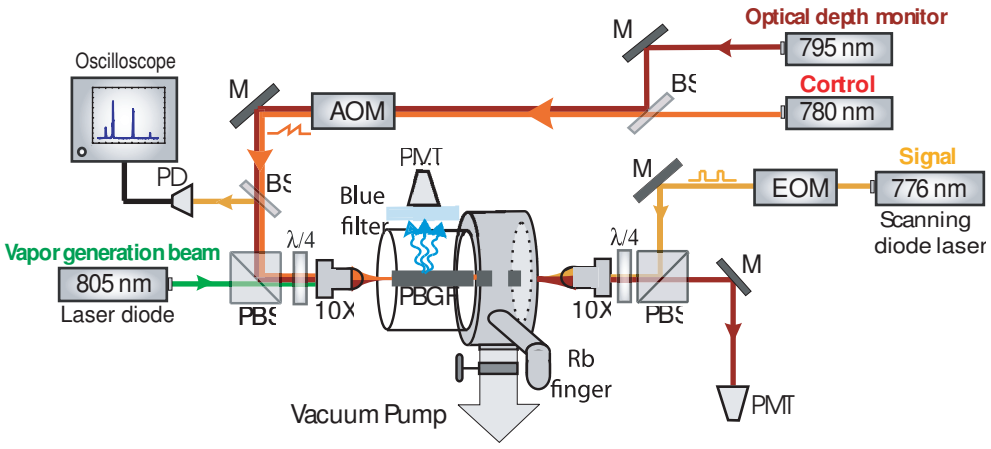

Figure 2.12: **Schematic of experimental setup:** Experimental setup for few-photon all-optical modulation. The polarizations of the signal and control beams are made identical (circular) using polarization beam splitter (PBS) cubes and quarter ($\lambda/4$) waveplates, and the beams are then coupled counter-propagating into the fiber. A pick-off is used to monitor the transmission of the signal beam using a sensitive photodetector (PD). A strong (3 mW) off-resonant vapor generation beam is also coupled into the fiber to generate the desired atomic density and optical depth. The optical depth is monitored during the experiment using a weak 795-nm beam scanning across the D1 resonance of Rb. An electro-optic modulator (EOM) driven by a function/waveform generator is used to make square pulses from the signal beam for the pulsed measurement. An acousto-optic modulator (AOM) driven by another function generator is used to ramp the power of the control beam as a sawtooth wave for the measurement.

the intermediate $5P_{3/2}$ level for an OD = 100. It is evident that maximum TPA is expected at Δ ~600 MHz and going closer to resonance is deleterious because of the dominance of the linear absorption of the 780-nm control beam over the TPA process. Our experimental observation is consistent with this theoretical prediction.

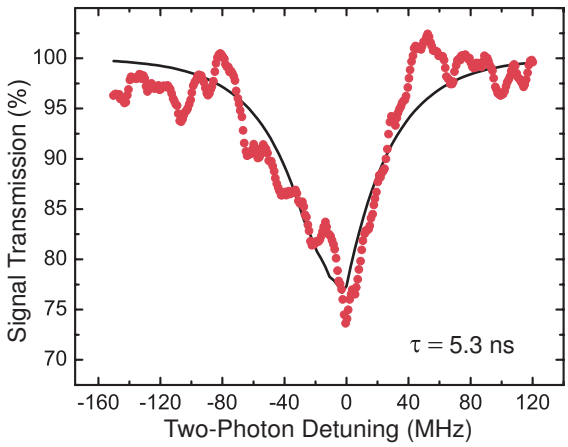

Figure 2.13: **Nondegenerate TPA** Transmission (red dots) versus detuning of the pump beam at 776 nm showing ~25 % absorption with 1.4 nW total power in the fiber. The 780 nm pump beam was tuned close to the $5S_{1/2} \rightarrow 5P_{3/2}$ ($F = 3 \rightarrow F' = 4$) transition. The solid black line shows a fit of sum of three exponentials corresponding to the accessible hyperfine states of $5D_{5/2}$ level, from which the transit time τ was extracted to be 5.3 ns.

Experimental setup:

The experimental setup is shown in Fig. 2.12. We use a 9-cm PBGF (Crystal Fiber AIR-6-800) inside a vacuum chamber with a Rb source attached. The pump lasers (at 776 nm and 780.2 nm) have identical polarizations and are coupled counter-propagating into the core of the fiber using 10X objectives. The 776-nm laser is scanned across the TPA resonances while the 780 nm beam is tuned to the D_2 line of 85Rb. Every Rb atom can simultaneously absorb one photon from each of the two counter-propagating beams, which minimizes Doppler broadening. A 3-mW highly non-resonant desorption beam at 805 nm is also coupled into the fiber to generate a high OD (~100). A pick-off is used to directly measure the absorption from the 776 nm pump beam.

Figure 2.13 shows the transmission signal of the 776 nm pump as its fre-

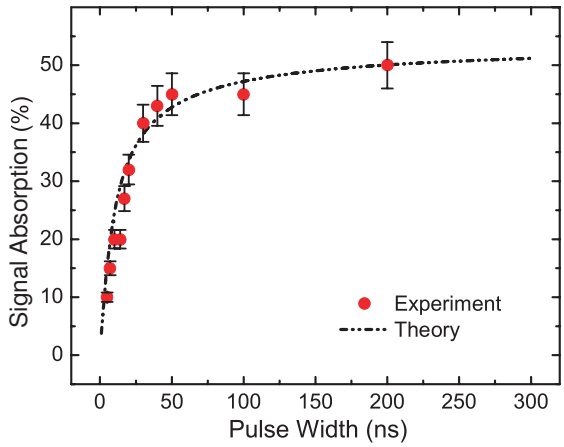

Figure 2.14: **Pulsed TPA measurement:** Absorption (red dots) of the pulsed signal beam at two-photon resonance versus pulse width. Error bars indicate measurement noise (one standard deviation). An amplitude modulator is used to create square pulses of varying duration (from 5 - 200 ns) from the signal beam, and the TPA is measured for each pulse width. The peak power in the signal pulses is kept the same (5 nW) for each measurement run. The control beam is kept CW and at the same power (5 nW) for all the measurements. The experimental data agree very well with the theoretically predicted curve (dotted black line) for a transit time τ = 5 ns of the Rb atoms across the fiber core and corroborates that the response time of the system is determined by the transit time.

quency was scanned across the $5P_{3/2} \rightarrow 5D_{5/2}$ line of Rb-85. The frequency of the 780 nm pump beam was detuned to 600 MHz from the $5S_{1/2} \rightarrow 5P_{3/2}$ ($F = 3 \rightarrow F' = 4$) transition. We observe 25% absorption with just 1.4 nm of total power in the fiber. The powers of the 776 nm and 780 nm beams were 600 pW and 825 pW, respectively. The Doppler-free absorption line is homogeneously broadened due to the extremely short transit-time of the atoms (~5 ns) across the 6 μm core of the fiber in comparison to the lifetime of the excited $5D_{5/2}$ level (~ 240ns). A transit-time limited transmission profile[77] is of the form,

$$T(\Delta) = 1 - Ae^{-\tau|\Delta|} \tag{2.13}$$

where, Δ is the detuning and τ is the transit-time. We fit the data in Fig. 2.13

to a sum of the three exponential functions corresponding to the three accessible hyperfine states ($F\prime = 3, 4, 5$) of the $5D_{5/2}$ level in Rb-85 and extract the transit-time to be 5.3 ns, which agrees well with out previous measurement of the transit-time in the Rb-PBGF system. We calculate the effective number of photons interacting within the response time τ of the system for a particular power P as

$$N = \frac{P\tau}{hc/\lambda} \tag{2.14}$$

where,hc/λ is the energy of one photon. For the 25% modulation shown in Fig. 2.13, the signal (λ = 776 nm) and control (λ = 780 nm) powers P = 600 pW and 825 pW correspond to only 12 and 16 photons, respectively, interacting with the atoms within the transit time. The switching energy is Nhc/λ, which for the 780-nm control beam corresponds to ~5 aJ. We also extract the two-photon absorption cross-section $\sigma^{(2)}$ to be 5×10^{-12} cm^4/W, which agrees with the theoretically calculated value taking into account the transit time of the Rb atoms as the dominant decay rate.

In order to confirm that the response time of our system is comparable to the transit time, we perform a pulsed measurement. An electro-optic modulator (EOM) is used to amplitude modulate the signal beam and produce square pulses of varying duration (from 5 - 200 ns), and the TPA is measured for each pulse width. The powers in the two beams were kept 5-10 times higher than in the previous CW measurement to improve the signal-to-noise ratio. The TPA is found to decrease as pulse width is reduced, as shown in Fig. 2.14.

2.3.3 Cross-phase modulation

As mentioned earlier, a new paradigm for quantum computation has recently been proposed based on weak-nonlinearities, where a strong coherent light field mediates interactions between photons [30, 78]. Weak-nonlinearities can be exploited to build photon-number resolving QND detectors [27, 79], and when coupled with homodyne measurements and classical feed-forward elements, can be used to construct nearly deterministic controlled-NOT (cNOT) gates[80] and nondestructive Bell state detectors [81]. A cross-phase shift (XPS) of 10^{-5} to 10^{-2} radians per photon is typically desired to make these schemes feasible [30, 78, 79, 80, 81]. For comparison, a XPS of 10^{-7} radians per photon was measured recently using a nonlinear photonic crystal fiber[82]. Previous experiments exploring large XPM in atomic vapors have mainly employed EIT-based schemes [33, 83, 84, 85], where the signal field spectrum has to fit within the narrow EIT transmission window, resulting in timescales $> 1\mu$s. Although these schemes provide large values of the nonlinear susceptibility, relatively large optical mode areas have limited the measured XPSs to ~$10^{-}6$ radians per photon.

By detuning slightly away from the two-photon transition, we can produce large XPM with very weak fields. Figure 2.15 shows the level scheme used in the XPM experiment. A nonlinear phase shift ϕ is induced by a weak circularly-polarized signal field, tuned close to the transition $5S_{1/2} \rightarrow 5P_{3/2}$ of Rb-85 with a detuning of Δ_1, on a linearly-polarized meter field, tuned to the $5P_{3/2} \rightarrow 5D_{5/2}$ with a detuning of Δ_2, while passing through a medium of Rb atoms confined to a PBGF. Due to the selection rules of the two-photon transition used, the meter field acquires a slight polarization rotation proportional to the intensity of the signal beam. Since the entire atomic population is in the ground $5S_{1/2}$ state, the

meter beam (tuned to the upper transition) does not experience any self-phase modulation. The real part of the third-order susceptibility,$\chi^{(3)}$ corresponding to XPM [71] is given by

$$\chi^{(3)} = \frac{N\mu_1^2\mu_2^2}{\varepsilon_o\hbar^3\Delta_1^2\Delta_2}. \tag{2.15}$$

The XPS is related to the second-order nonlinear refractive index as

$$n_2 = (2.82 \times 10^6)\chi^{(3)}(cm^2/W). \tag{2.16}$$

Knowing the second-order nonlinear refractive index, we estimate the XPS induced on the meter beam, ϕ, for a given signal beam power, P_S, using

$$\phi = 2k_M n_2 P_S \frac{L_{eff}}{A}, \tag{2.17}$$

where n_2 is the second-order index of refraction, $k_M = 2\pi/\lambda_M$ is the wave-number of the meter, $\lambda_M = 776$ nm is the wavelength of the meter, L_{eff} is the effective interaction length and $A \sim 10^7$ cm^2 is the optical mode area. The XPS thus scales linearly with signal power. The effective interaction length is given by

$$L_{eff} = \frac{1 - e^{\alpha L}}{\alpha} \tag{2.18}$$

where $L \sim$ 1cm is the sample length and α is the absorption coefficient of the signal. We use a Doppler broadened profile for α as mentioned in eq. 2.9. To maximize XPM, naively one might reduce the detunings Δ_1 and Δ_2 as much as possible to resonantly enhance the interaction. However, it is necessary to have $\Delta_2 >> \gamma$ to minimize loss due to two-photon absorption (TPA), where $\gamma \sim 50$ MHz is the TPA linewidth previously measured in our system [69, 86]. Moreover, since the 780-nm signal beam experiences ordinary linear absorption, the optimal detuning Δ_1 is non-trivial. We thus compute $n_2(\Delta), \alpha(\Delta)$ and L_{eff} for a particular detuning Δ, and then calculate the XPS induced at that detuning. For the Rb-PBGF system, using an atomic density $N = 2\times10^{13}$ atoms/cm^3 which

corresponds to an OD ~100, we estimate an effective $n_2 = 3 \times 10^6$ cm^2/W. We estimate that the meter beam must have a fixed frequency such that $\Delta_1 = \Delta_2$ and the maximum XPS is obtained at $\Delta = 700$ MHz.

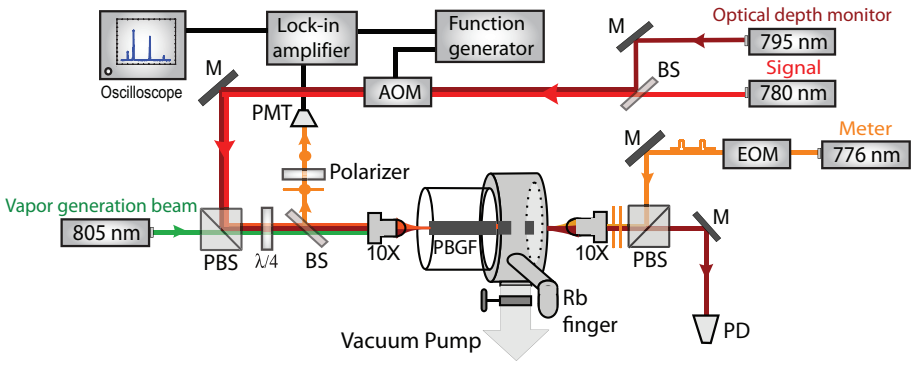

Figure 2.15: **XPS level scheme and experimental setup**(a) (b)The linearly polarized meter and circularly polarized signal beams are coupled counter-propagating into the fiber. The meter beam undergoes slight polarization rotation due to crossphase modulation from the weak signal beam. A polarizer is used at the output to select the meter polarization orthogonal to that at the input, and measured with a photomultiplier tube (PMT). An acousto-optic modulator (AOM) is used to amplitude modulate the signal at 25 kHz, and a lock-in amplifier detects the cross-phase shift imparted on the meter at the same frequency. A strong (3 mW) off-resonant vapor generation beam is also coupled into the fiber to generate the desired atomic density and optical depth. The optical depth is monitored during the experiment using a weak 795-nm beam scanning across the D1 resonance of Rb. An electro-optic modulator (EOM) is used to make square pulses of varying duration from the meter beam for pulsed measurements.

The experimental setup is shown in Fig. 2.15. The meter and signal lasers (at 776nm and 780.2 nm) are coupled counter-propagating (to eliminate Doppler broadening) into the core of the fiber using 10X objectives. A 3-mW highly non-resonant vapor generation beam at 805 nm is also coupled into the fiber to generate a high OD (100). The signal is circularly polarized (σ^+) and the meter is linearly polarized ($x = \sigma^+ + \sigma^-$) at the input. Due to the selection rules of the

$5S_{1/2} \rightarrow 5D_{5/2}$ two-photon transition [87], only the σ^+ component of the meter experiences XPS. As a result, the polarization of the meter at the output of the fiber is $x = \sigma^+ + e^{i\phi}\sigma^- \approx \mathbf{x} + (\phi)\mathbf{y}$ (for $\phi << 1$), where ϕ is the XPS in radians. A polarizer selects only the y-component of the meter polarization for detection. The power in the meter beam is kept between 1 and 10 μW for all measurements.

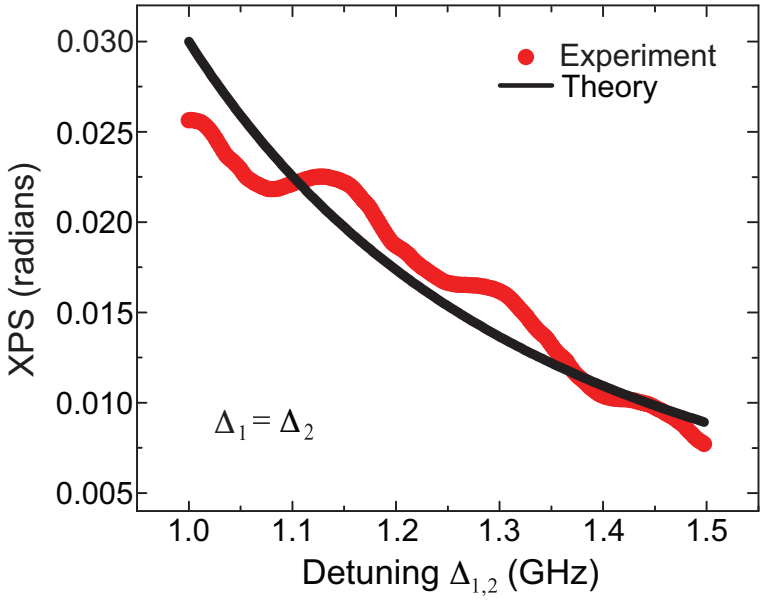

Figure 2.16: **XPS Measurement:** (a) Cross-phase shift (XPS) imparted on the meter beam (red dots) versus detuning from two-photon resonance. The data are shown for one continuous scan of the laser. Tens of milliradians of phase shift are observed even for detunings greater than 1 GHz from line center. The signal absorption at these detunings is < 1%. The signal power is 50 nW, and the OD in the fiber is ~50. The power in the meter beam is 2 μW. The solid black line shows the theoretical calculation taking into account the Doppler absorption profile of the atoms in the fiber core. The deviation of the experimental data from theory is due to slow drifts in the coupling and polarization maintenance of the PBGF as the laser is scanned in frequency at a rate of ~10 Hz.

The meter beam has a fixed frequency such that $\Delta_1 = \Delta_2$ to maximize XPS. The XPS increases closer to resonance as expected from theory, and the maximum XPS was observed at a detuning of ~700 MHz. Further tuning closer to

resonance resulted in significant absorption of the signal. Figure 2.16 shows the measurement of XPS imparted on the meter as the signal is scanned in frequency to the blue of the $5S_{1/2} \rightarrow 5P_{3/2}(F = 3 \rightarrow F' = 4)$ transition. The data are shown for one continuous scan. Tens of milliradians of phase shift are observed even for detunings greater than 1 GHz from line center. The signal absorption at these detunings is $< 1\%$, so this is truly a non-demolition measurement of the signal intensity. The deviation of the experimental data from theory is due to slow drifts in the coupling and polarization maintenance of the PBGF as the laser is scanned in frequency at a rate of ~10 Hz. The signal power was 50 nW, while the meter power was 2 μW, and the OD in the fiber was 50.

We verified that the response time of our system by measuring the XPS imparted on square pulses of the meter beam of varying duration. XPS remains close to the CW value for pulse widths down to 5 ns as expected. Finally, we performed XPS measurements at the few photon level. The XPS induced on the meter as a function of signal power for an OD~100 in the fiber is shown in Fig. 2.17. We calculate the average number of signal photons present in a 5-ns pulse from the corresponding signal power, and a 5 milliradian phase shift is measured with only ~16 signal photons. The number of photons per atomic cross-section is calculated as $(N/A)(3\lambda^2/2\pi)$ (where A~10^{-7} cm^2 is the optical mode area). Thus P~0.8 nW corresponds to an energy density much less than one photon per atomic cross-section. From the slope of the solid black line in Fig. 2.17, we infer an XPS of 0.3 milliradian per signal photon, which to our knowledge, represents the largest such nonlinear phase shift induced in a single-pass through a room-temperature medium [88].

Validity of the semi-classical approximation: It is to be noted that through-

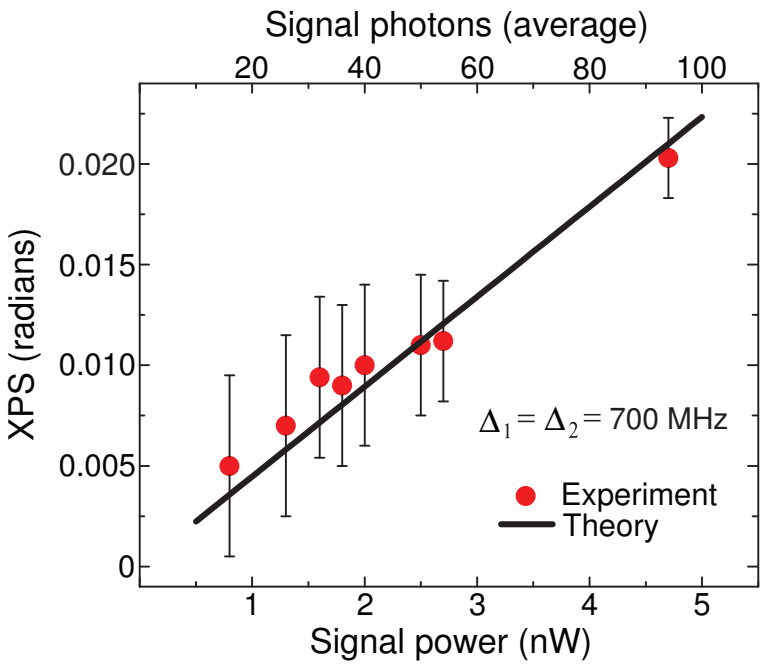

Figure 2.17: **XPS Measurement:** Large cross-phase modulation at the few-photon level. Cross phase shift (XPS) imparted on the meter (red dots) as a function of average signal power (and average number of signal photons in a 5-ns pulse). Error bars indicate measurement noise (one standard deviation). An OD~100 is produced in the fiber for each measurement. The power in the meter beam was 10 μW for each measurement. A ~5 mrad phase shift is measured for ~16 signal photons, corresponding to ~5 aJ of energy. The solid black line shows the theoretical prediction, and the slope corresponds to an XPS of ~0.3 mrad per signal photon, which to our knowledge, represents the largest such nonlinear phase shift induced in a single-pass through a room temperature medium.

out this chapter we have used coherent state light fields for all experiments and the expectation value of the annihilation operator for a coherent state is the square root of the average number of photons. Therefore all calculations/estimation of photon numbers are on-average and validates the use of semi-classical expressions for estimating two-photon absorption and cross-phase modulation. The use of purely quantum mechanical expressions via quantization of the light field are required to estimate the cross-phase modu-

lation for non-classical states eg. a single photon Fock state. The experiments demonstrated in this chapter are still an order of magnitude away from the true single photon regime. This type of modelling is consistent with XMP measurements reported in the literature [82] where they also measured XPM in fibers caused by light fields at the single photon level and use the semi-classical expression for XPM scaling linearly with average number of photons. However there have been full-blown quantum mechanical theoretical investigations into the phase shifts caused by true single photon Fock states [29], but there still is no consensus amongst the research community as to what really happens in the single photon regime. Thus experiments that enable to probe that regime can provide insight and answer fundamental questions. These TPA experiments are a small step towards that direction.

2.4 Summary and Conclusion

In summary, the strong optical confinement along with long interaction lengths in a hollow-core photonic bandgap along with the ability to confine atoms, provides a suitable platform for exploring extremely strong light-matter interactions. Leveraging on these, we demonstrate few-photon all-optical modulation using non-degenerate TPA in thermal Rb atoms confined to a hollow core PBGF. We show 25% attenuation of a signal beam with a switching energy of only 5 attojoules, corresponding to about 16 photons. The switching energy density is less than one photon per atomic cross-section. We also characterize the time response of the system to be 5 ns, which enables large modulation bandwidths up to 50 MHz for a highly sensitive atomic vapor-based scheme. In addition, we observe cross-phase modulation with less than 20 photons using TPA resonances

in Rb vapor confined to a PBGF. A XPS of 0.3 milliradian per signal photon is induced on a meter beam with a fast response time of less than 5 ns. We infer a nonlinear refractive index value $n_2 = 3 \times 10^6$ cm^2/W. This system enables us to explore a wide space of atomic densities and optical intensities in a controllable manner and holds promise for integration with fiber-optic communication networks. These results show the potential of a Rb-PBGF system for exploring quantum nonlinear effects at ultralow powers such as single-photon all optical switching, generation and measurement of non-classical states of light, and accessing higher-order nonlinear susceptibilities.

CHAPTER 3

SILICON NITRIDE MICRORESONATOR BASED OPTICAL FREQUENCY COMBS

3.1 Introduction

In this chapter we show that nanofabricated silicon nitride microresonators can be used to demonstrate extreme nonlinear optics. This silicon nitride platform is complementary-metal-oxide-semiconductor (CMOS) process compatible, and the devices are monolithic and sealed, such that pump coupling to the resonator and system operation are insensitive to the environment. Additionally this platform allows for dispersion engineering the waveguides to efficiently generate optical frequency combs via cascaded four-wave mixing. We demonstrate the generation of an octave spanning comb with 226 GHz repetition rate pumping at 1560 nm. Next we show that by dispersion engineering the waveguide dimensions, we can generate combs by pumping at 1064 nm. The advantage of this platform is that we can independently tune the free spectral range (FSR) and the dispersion. We exploit this property of the silicon nitride microresonator platform to generate microcombs with various FSRs such as 20-, 40-, 80-, 100-GHz. Next we go on to characterize the spectral and temporal dynamics of the microresonator based combs and demonstrate that such parametric frequency combs can generate modelocked ultra-short pulses.

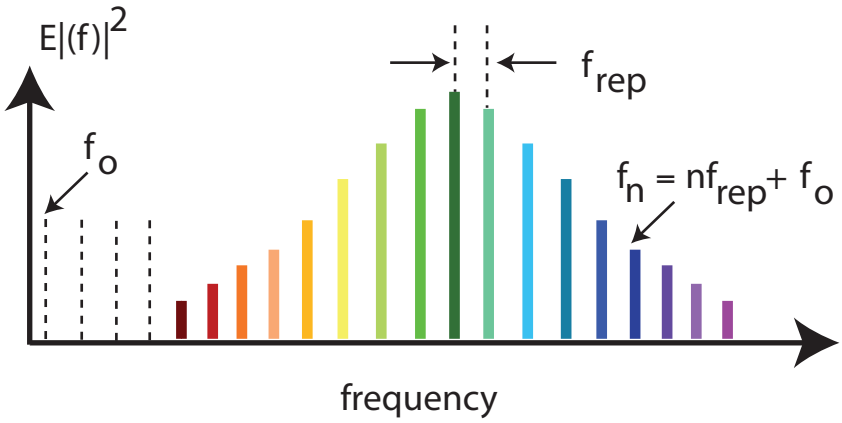

Figure 3.1: **Illustration of a frequency comb:** Power spectrum of a frequency comb.

3.2 Generation of frequency comb

An optical frequency comb consists of a discrete series of "comb" lines which are equally spaced by the repetition frequency, f_{rep}. It is characterized by the carrier envelope offset frequency and the comb spacing or the repetition rate as shown in Figure 3.1. Additionally, a series of discrete lines in the frequency domain leads to short pulses in the time domain. Figure 3.2 shows a schematic of a train of pulses with a shift in phase between the carrier sinusoid and the envelope. This shift in phase is given by $\Delta\phi = \phi_1 - \phi_2$. The separation between pulses is simply the round trip time for the cavity or the inverse of the repetition frequency. The difference in phase $\Delta\phi$ between the envelope and carrier for successive pulses is a result of dispersion in the gain medium and nonlinear phase that the pulse picks up as it makes a round trip. Since the properties of the cavity are not time dependent, the phase difference between successive pulses stays the same at $\Delta\phi$ the result of this carrier envelope phase offset is that the comb shifts by a fixed constant frequency i.e. the carrier envelope offset frequency f_o given by $f_o = \frac{1}{2\pi}\Delta\phi f_{rep}$. Thus an optical frequency comb is not only

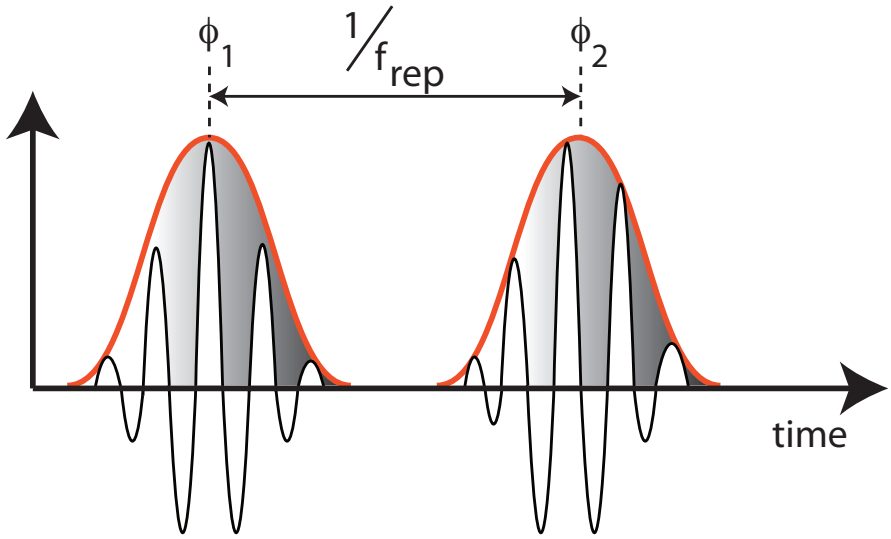

Figure 3.2: **Pulses:** Power spectrum of pulses generated from an optical frequency comb.

a source of multiple optical frequencies but also ultrashort mode-locked pulses.

The most common source of frequency combs has been modelocked Ti Sapphire lasers. A femtosecond laser based on a mode locked Ti:Sapphire laser was first reported in [91] with 60 fs pulses at a repetition rate of 75-100 MHz with a tunable cavity. While Ti:Sapphire-based frequency combs have become a mature technology and repetition rates as high as 10-GHz has been reported, there has been significant recent interest in comb generation using ultrabroadband parametric oscillation based on four-wave mixing (FWM) pumped by a continuous-wave (cw) pump field in high-Q cavities such as silica microtoroids, CaF_2, MgF_2 and quartz resonators, silica microspheres, and high-index silica-glass microrings[92, 41, 93, 42, 94, 95, 96, 97, 98]. Thus, microresonator-based frequency comb generation has been an area of intense research in the past few years, particularly because of its potential as a platform for the realization of compact, integrated stabilized comb sources. This chapter discuses the

advancement of the microresonator-based technology to generate optical frequency combs in a CMOS-compatible silicon-nitride platform. Using this platform we demonstrate the generation of optical frequency combs with pumps at different wavelengths and characterize the spectral and temporal dynamics of the same.

3.2.1 Silicon based microresonator

The emerging field of silicon photonics allows us to develop more efficient networks that go beyond the capabilities and limitations of existing systems. Integrated photonics may provide a route towards keeping pace with Moore's Law [99, 100]. Expertise in silicon fabrication has advanced by leaps and bounds due to its applications in the semiconductor electronics industry. This expertise can be applied directly to fabricating photonic devices using silicon as a medium of propagation for light. Silicon has high nonlinear optical response with moderate intensities. The research in the area of nanofabricated silicon devices has been directed towards more efficient and low-power nonlinear optics. The high intensities required to see non linearity can be achieved by using waveguides which confine light to a small mode volume thus increasing spatial overlap. The interaction length, another important factor in determining the strength of nonlinear processes, is traditionally determined by the diffraction limit of the focused beam. Since beams with a smaller focal area have a shorter diffraction length, there is an intractable trade-off between intensity and length. By using an optical waveguide, we can increase the interaction length beyond the diffraction limit. Much work has been done exploiting the low-loss of optical fibers to show a rich array of potential nonlinear processes. More recently, work

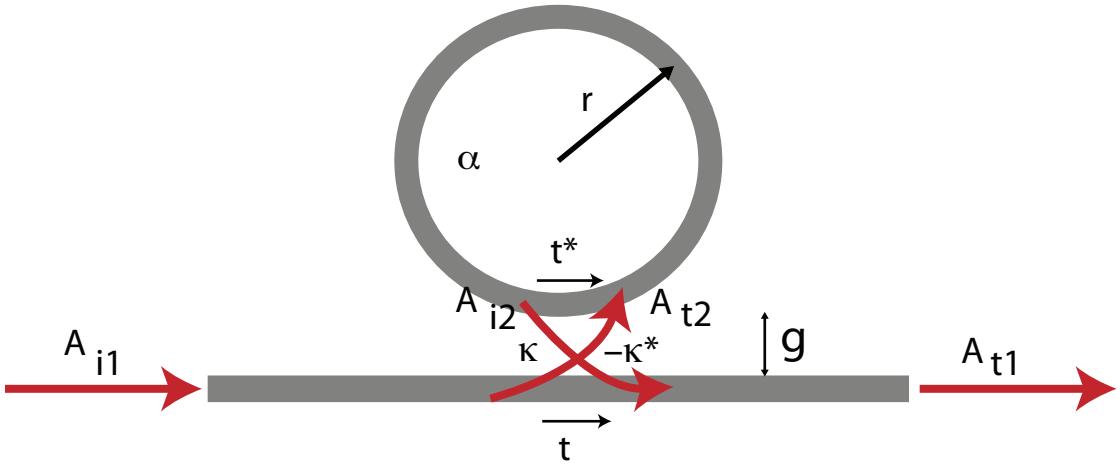

Figure 3.3: **Schematic of ring resonator:** Illustration of ring resonator coupled to a bus waveguide. The ring resonator has radius, r, and a coupling gap, g, from ring to waveguide. The diagram shows the coupling,κ, and transmission, t, coefficients for the input and output fields of the device along with the round-trip loss factor, α.

has been done on integrated photonic devices, which confine light to an even smaller scale. Silicon-based nonlinear devices have already enabled [36], parametric amplification [37], signal regeneration [38], demultiplexing [151], and utlra-fast signal detection [40]. However, nonlinear loss mechanisms limit the efficiency of many processes in silicon. One can overcome the effect of nonlinear losses by using silicon nitride devices instead of silicon devices and use silicon nitride based microresonators for the development of on-chip optical frequency combs. The next section provides a summary of the working principles of a ring resonator. Following which we demonstrate how this microresonator is applied to generate optical frequency combs.

The ring resonator system

Figure 3.3 shows the basic configuration [101], which consists of unidirectional coupling between a ring resonator with radius r and a waveguide. We assume that a single unidirectional mode of the resonator is excited with a single polarization, and the coupling is lossless, none of the waveguide segments and coupler elements couple waves of different polarization, the various kinds of losses occurring along the propagation of light in the ring resonator filter are incorporated in the attenuation constant, the interaction can be described by the matrix relation:

$$\begin{pmatrix} A_{t1} \\ A_{t2} \end{pmatrix} = \begin{pmatrix} t & \kappa \\ -\kappa* & t* \end{pmatrix} \begin{pmatrix} A_{i1} \\ A_{i2} \end{pmatrix}. \tag{3.1}$$

The complex mode amplitudes A are normalized, and the squared magnitude corresponds to the modal power. The coupler parameters t and κ depend on the specific coupling mechanism used. The $*$ denotes the conjugated complex value of t and κ, respectively.

$$| \kappa^2 | + | t^2 | = 1. \tag{3.2}$$

We assume that the field inside the cavity undergoes a roundtrip loss and the relate incoming and outgoing field in the cavity as

$$A_{i2} = \alpha e^{j\theta} A_{t2}. \tag{3.3}$$

where α is the loss coefficient of the ring (zero loss: $\alpha = 1$) and $\theta = \omega L/c$, L being the circumference of the ring which is given by $L = 2\pi r$, r being the radius of the ring measured from the center of the ring to the center of the waveguide, c the phase velocity of the ring mode ($c = c_0/n_{eff}$) and the fixed angular frequency

$\omega = kc_0, c_0$ refers to the vacuum speed of light. The vacuum wavenumber k is related to the wavelength λ through:$k = 2\pi/\lambda$. Using the vacuum wavenumber, the effective refractive index n_{eff} can be introduced easily into the ring coupling relations by

$$\beta = kn_{eff} = \frac{2\pi n_{eff}}{\lambda}, \tag{3.4}$$

where β is the propagation constant. This leads to

$$\theta = \frac{\omega L}{c} = \frac{kc_0 L}{c} = kn_{eff}2\pi r = 4\pi^2 n_e f f \frac{r}{\lambda}. \tag{3.5}$$

Using these we derive the transmitted power P_{t1} in the output waveguide as

$$P_{t1} =\mid A_{t1} \mid^2= \frac{\alpha^2+ \mid t \mid^2 -2\alpha \mid t \mid cos(\theta + \phi)}{1 + \alpha^2 \mid t \mid^2 -2\alpha \mid t \mid cos(\theta + \phi)} \tag{3.6}$$

where $t =\mid t \mid exp(j\phi), \mid t \mid$ is the coupling losses and ϕ is the phase of the coupler. The power circulating in the ring is given by

$$P_{i2} =\mid A_{i2} \mid^2= \frac{\alpha^2(1- \mid t \mid^2)}{1 + \alpha^2 \mid t \mid^2 -2\alpha \mid t \mid cos(\theta + \phi)}. \tag{3.7}$$

On resonance $\theta + \phi = 2\pi m$, where m is an integer. Thus we obtain,

$$P_{t1} =\mid A_{t1} \mid^2= \frac{(\alpha^2- \mid t \mid^2)^2}{1 - 2\alpha \mid t \mid)^2}, \tag{3.8}$$

and

$$P_{circ} = P_{i2} =\mid A_{i2} \mid^2= \frac{\alpha^2(1- \mid t \mid^2)}{(1 - \alpha^2 \mid t \mid)^2}. \tag{3.9}$$

Now there could be three possible coupling situations:

Undercoupled: In this regime the cavity coupling rate is smaller than the intrinsic cavity loss rate. Thus the field transmitted through the external waveguide is higher than the field coupled from the resonator to the waveguide. The phase shift of the field leaking out of the cavity is less than 180°. This regime can experimentally be reached by increasing the coupling gap between the waveguide and the resonator.

Crtically coupled: In this regime the cavity coupling rate is equal to the intrinsic cavity loss rate. On resonance, the field that leaks out of the cavity and the field in the waveguide are 180° out of phase, leading to destructive interference.

Overcoupled: In this case, the cavity coupling rate is larger than the intrinsic cavity loss rate. Most of the power couples directly into the cavity, leading to a cavity leakage field that is higher than the field transmitted through the waveguide. The phase shift of the cavity leakage field is more than 180°. This regime can be experimentally reached by reducing the coupling gap between waveguide and resonator.

To estimate the amount of power built up inside a cavity we can measure the quality factor, Q. The Q of an optical resonator, which is a dimensionless parameter, is the ratio of the stored energy to the energy dissipated per oscillation cycle, or equivalently the ratio of the stored energy to the energy dissipated per radian of the oscillation and can be expressed as

$$Q = \omega_0 \frac{U}{-dU/dt}, \tag{3.10a}$$

$$Q = \frac{\omega_0}{\Delta\omega_{FWHM}} \approx \frac{\lambda_0}{\Delta\lambda_{FWHM}} \tag{3.10b}$$

where U is the stored energy in the cavity and FWHM is the full bandwidth at half maximum of the transmitted power from equation and is referred to as the cavity linewidth. The Q is related to the photon lifetime τ_p as

$$Q = \omega_0 \tau_p, \tag{3.11}$$

where τ_p arises from absorption, scattering, bending and coupling losses. The Q defined in eq. 3.10 takes into account all the losses of the system: from the ring and from the coupling. This is defined as the loaded Q, Q_L, and can be directly measured from the transmission spectrum.

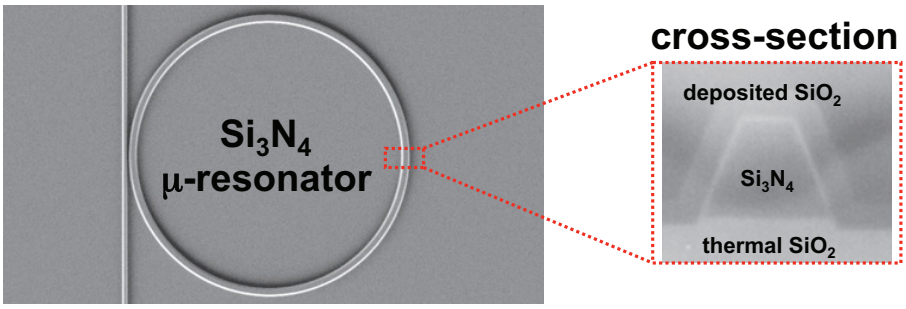

Figure 3.4: **SEM of silicon nitride microresontor:** A scanning electron micrograph of a silicon-nitride microresonator resonator with a zoomed-in viewgraph of the waveguide cross-section.

In a microcavity, the power circulating inside the cavity on resonance can be related to the Q as,

$$\frac{P_{circ}}{P_{in}} = \frac{\lambda}{2\pi nL} Q \tag{3.12}$$

and it can be written in terms of the finesse as

$$\frac{P_{circ}}{P_{in}} = \frac{F}{2\pi}. \tag{3.13}$$

The silicon nitride ring resonators (fig. 3.4) are fabricated on a silicon wafer, and a 4-μm thermal oxide layer is initially grown for the undercladding. Next, a nitride film is deposited, and both the microring and the coupling waveguide are patterned and etched monolithically in the silicon nitride layer. Finally, an oxide layer is deposited to form the top cladding [96]. The relatively high index contrast between the nitride core and the oxide cladding allows for dispersion engineering through modification of the waveguide cross-section [102, 103], and, since the dispersion is dependent on the cross-sectional size and shape, such engineering can be accomplished without changing resonator parameters such as the cavity free spectral range (FSR).

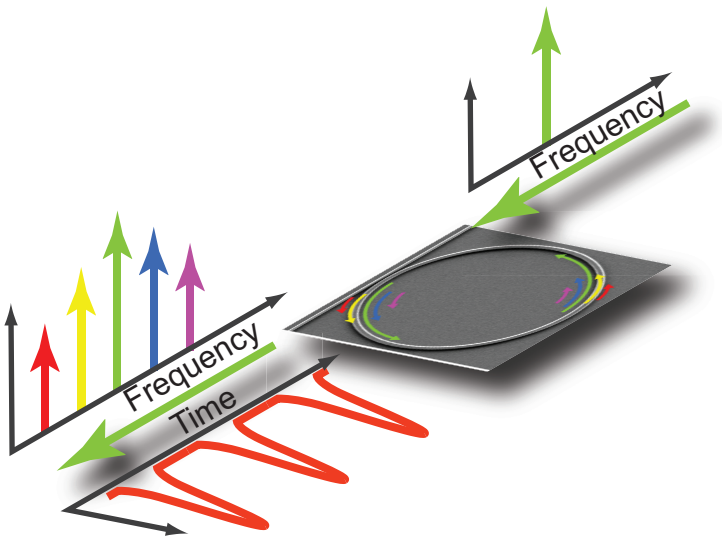

Figure 3.5: **Illustration of a microresontor based frequency comb:** Figure shows the general scheme for generating optical frequency combs and ultra-short pulses using cascaded parametric oscillation in a high-Q silicon-nitride microresonator. Pumping with a single frequency continuous-wave laser, a wide-band frequency comb is generated.

3.2.2 Parametric oscillation

In a silicon nitride microresonator an optical frequency comb is generated via cascaded four-wave mixing (FWM). FWM is a third order nonlinear process involving four waves, two pump waves, a signal and an idler wave. The process is parametric when the two pump photons are annihilated, strict energy conservation dictates the frequencies of the converted signal and idler waves. Degenerate FWM occurs when the pump photons are the same frequency and provide both photons for the nonlinear interaction. FWM arises from the nonlinear polarization induced by $\chi^{(3)}$ in the material when the interactions between the four waves are considered. The nonlinear polarization can be expressed in terms of

the interacting fields as [71, 4]

$$P_n^{NL} = \sum_{i,j,k} \epsilon_0 \chi^{(3)} \left(\omega_n = \omega_i + \omega_j + \omega_k : \omega_i, \omega_j, \omega_k\right) \mathbf{E}_i \mathbf{E}_j \mathbf{E}_k, \tag{3.14}$$

where P^{NL} is the nonlinear polarization, $\chi^{(3)}$ is the third-order nonlinearity, $\omega_{i,j,k}$ are the frequencies of the interacting fields and $\mathbf{E}_{i,j,k}$ are the amplitudes of the interacting fields. The coupled field equations then have a general form:

$$\frac{dE_n}{dz} = \frac{j2\pi\omega_n}{nc} P_n^{NL}. \tag{3.15}$$

where E_n is th field amplitude at frequency ω_n. In the limit of a strong pump the field amplitudes for degenerate FWM can then be expressed as

$$\frac{dE_p}{dz} = -\frac{\alpha_p}{2} E_p + j\gamma \mid E_p \mid^2 E_p, \tag{3.16a}$$

$$\frac{dE_s}{dz} = -\frac{\alpha_s}{2} E_s + j\gamma \mid E_p \mid^2 E_s + j\gamma \mid E_p \mid^2 E_i^* e^{-j\Delta kz}, \tag{3.16b}$$

$$\frac{dE_i}{dz} = -\frac{\alpha_s}{2} E_i + j\gamma \mid E_p \mid^2 E_i + j\gamma \mid E_p \mid^2 E_s^* e^{-j\Delta kz}, \tag{3.16c}$$

where γ is the nonlinear coefficient, $E_{p,s,i}$ are field amplitudes of the pump, signal and idler respectively and Δk is the phase mismatch and is expressed as

$$\Delta k = 2\gamma P_p + 2k_p - k_i - k_s, \tag{3.17}$$

where $k_{p,s,i}$ are the wavevectors of the pump, signal and idler respectively and $2\gamma P_p$ is the nonlinear phase shift arising from self phase modulation (SPM) and cross phase modulation (XPM). For efficient FWM, it is necessary to satisfy the phase-matching condition as well as the energy conservation condition $2\hbar\omega_p = \hbar\omega_i + \hbar\omega_s$ must also be satisfied. Since the phase-matching condition is dependent both on pump power and the propagation constants at each wave, in order for it to be zero, we must achieve anomalous group velocity dispersion. Since the material dispersion is normal, we must use the waveguide dispersion (or modal dispersion) as counterbalance this effect.

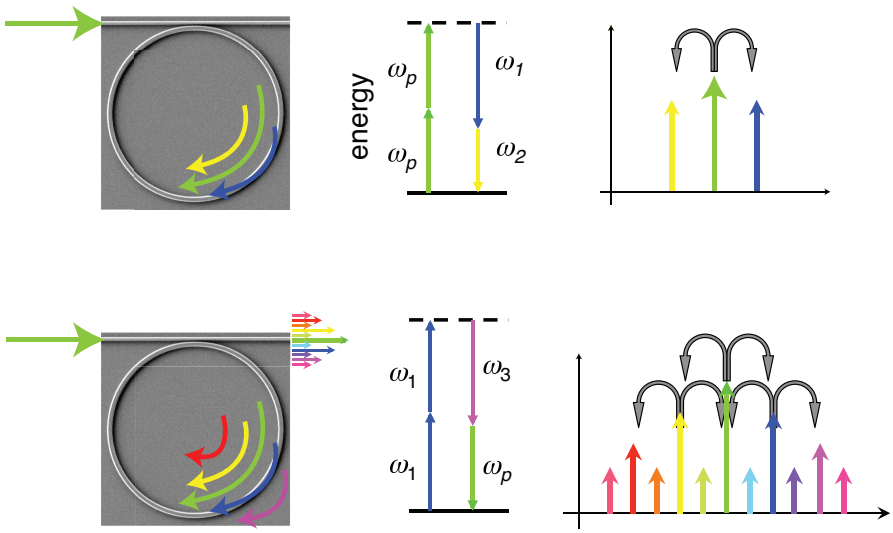

Figure 3.6: **Schematic of comb generation dynamics:** Illustration of how a frequency comb is generated via cascaded four-wave mixing(FWM) in a silicon nitride microresonator. As we tune into resonance of the cavity, a single frequency pump is coupled into the microresonator and the power builds up proportional to its quality factor. When the phase matching condition is satisfied, two pump photons are converted into a signal and idler via degenerate FWM. When more power is coupled into the resonator, the signal and idler act as pumps themselves and generate minicombs via several degenerate and non-degenerate FWM processes.

In the parametric FWM process in a microresonator, as the pump is tuned into the cavity resonance, two pump photons are initially converted to a signal and idler photon pair [96, 49, 104, 105]. As more power is coupled into the resonator, and the FWM gain is enhanced by the cavity geometry and transverse confinement, leading to cascaded parametric oscillation, enabling the generation of a broadband comb. Figure 3.5 shows an illustration of the general scheme for generating optical frequency combs using a silicon nitride microresonator.

Recently a lot of research has been focussed on theoretical understanding of the comb generation dynamics [106, 107]. The focus has been on simulating

the comb dynamics via modal-expansion as this allows the electric field to be defined not as a function of frequency but as a summation of the modes of the resonator [108, 109, 110]. This is because the frequency comb is composed of very narrow, discrete frequency lines spanning a broad frequency range, but it is difficult to simulate all frequencies at a resolution fine enough to accurately define each comb line. However, as shown in eq. 3.15 the nonlinear Kerr term involves a triple-summation over the interacting modes, resulting in a computational time with a cubic dependence on the number of modes being considered. A new approach involves applying the Lugiato-Lefever(LL) equation for simulating full temporal and spectral dynamics of a microresonator based comb [104]. The advantage of this technique is that, in this model the fields are treated both in time and in frequency and includes higher-order dispersion and self-steepening to enable simulations of comb spectra that span an octave with 4 orders of magnitude increase in computational speed. The experimental demonstrations of comb generation dynamics in the spectral and temporal domain, as described in this chapter, closely agree with the theoretical predictions of the LL model.

3.2.3 Octave spanning comb

The generation of broadband optical frequency combs is of great interest for numerous applications including spectroscopy, precision frequency metrology and optical clocks [89]. Many of the previous comb generation techniques rely on supercontinuum generation spanning 100's of THz in optical fibers using high-power mode-locked lasers [113]. The generation of comb spectra spanning an octave is highly desirable for full stabilization of the frequency comb

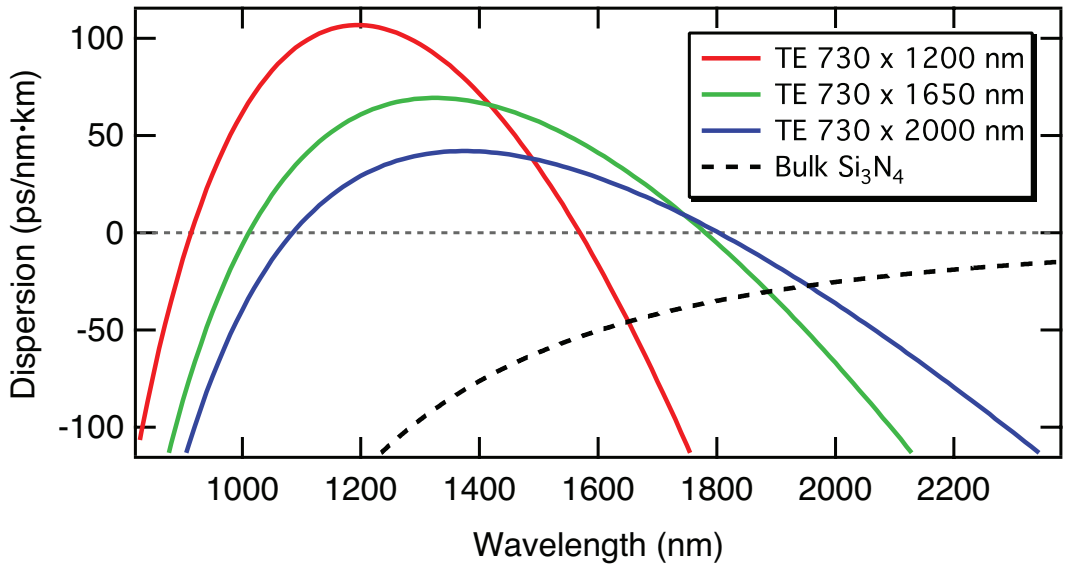

Figure 3.7: **Dispersion engineering for generating octave spanning comb:** Dispersion simulations for the fundamental TE mode of a silicon-nitride waveguide with the height fixed at 730 nm and widths of 1200, 1650, and 2000 nm. The dashed curve indicates the dispersion for bulk silicon nitride.

through the well-established self-referencing technique [111]. An octave spanning comb allows for full calibration of the comb, i.e. know the f_{rep} and the f_o. If a comb is octave spanning, i.e. it has a bandwidth such that there are comb lines at frequencies f_n and f_{2n}, then we can determine the offset frequency by frequency doubling the lower comb line (using a SHG crystal) and looking at the beat frequency with the higher frequency comb line. If $f_n = f_o + nf_{rep}$, then the doubled frequency is: $2f_n = 2f_o + 2nf_{rep}$ and if we have a comb line $f_{2n} = f_o + 2nf_{rep}$ at the other end of the octave, the beat frequency is simply the offset frequency. This can be used as a feedback to stabilise the cavity and maintain the offset frequency at a specific value.

In this section, we report the first demonstration of an octave-spanning parametric frequency comb in a silicon-based microring resonator [112]. As men-

tioned before, this silicon nitride platform is CMOS process compatible, and the devices are monolithic and sealed, such that pump coupling to the resonator and system operation are insensitive to the environment. Additionally, high-Q silicon nitride resonators can be fabricated with Q-factors as high as 3×10^6 [114]. This demonstration represents a significant step towards a stabilized, integrated frequency comb source that is robust and can be scaled to other wavelengths.

Recently, high Q-factor optical microcavities have shown enormous potential as a platform for efficient nonlinear optical processes. To achieve efficient phase matching, the pump laser is operated in the anomalous-GVD regime to compensate for the nonlinear phase mismatch [42, 104]. The cavity geometry results in an additional restriction, such that the pump, signal, and idler must each overlap with a cavity resonance. As mentioned in section 3.2.2 to achieve overall anomalour-GVD the waveguide dispersion has to be controlled since the material dispersion can't be controlled. The advantage of the silicon-nitride platform is that it the dispersion can be controlled by changing the width and the height of the waveguide [102]. To understand the waveguide conditions necessary to achieve broadband parametric comb generation, we theoretically calculate the GVD using a finite-element mode solver. Figure 3.7 shows the simulated dispersion for silicon nitride waveguides with a height of 730 nm, and widths of 1200, 1650, and 2000 nm. The curves indicate that large anomalous-GVD bandwidths spanning nearly an octave are possible with appropriate cross-section engineering. The signal/idler pair that oscillate at threshold are those that satisfy the energy conservation and phase matching conditions required for FWM. The resonator is pumped at 1562 nm using a single-frequency pump laser, and we generate a parametric comb spanning from 1170 nm to 2350 nm, corresponding to a 128-THz span.

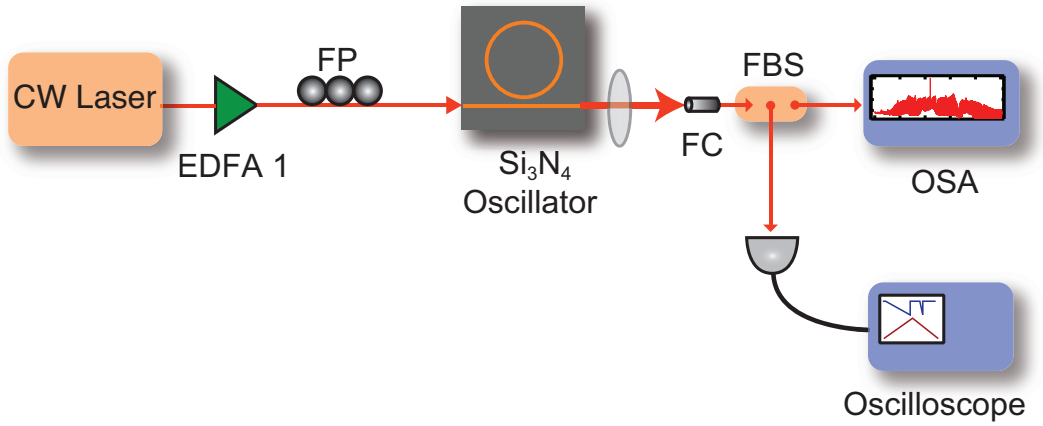

Figure 3.8: **Experimental setup for generating octave spanning comb:** The experimental setup used for generating an octave spanning microresonator based comb. A single-frequency diode laser centered at 1562 nm is amplified with a erbium-doped fiber amplifier (EDFA) and inject it into a nanowaveguide using a lensed fiber. The input polarization is adjusted to quasi-TE using a fiber polarization controller. The output is collected with a free-space objective, fiber coupled (using FC) and sent to an optical spectrum analyser (OSA) for measuring the output spectrum. A small portion of the transmitted beam is initially also used for monitoring the optical resonance while tuning in to generate the comb.

Experiment and discussion

Figure 3.8 shows the experimental setup used for generating an octave spanning microresonator based comb. In our experiment, we amplify a single-frequency diode laser centered at 1562 nm with a erbium-doped fiber amplifier (EDFA) and inject it into a nanowaveguide using a lensed fiber. The input polarization is adjusted to quasi-TE using a fiber polarization controller. The nanowaveguide acts as the coupling waveguide for the microring resonator. Both the coupling waveguide and the microring have cross-sections of 725 nm by 1650 nm, and the microring has a 200-μm diameter. The power inside the coupling waveguide is 400 mW when the pump wavelength is detuned from a cavity resonance.

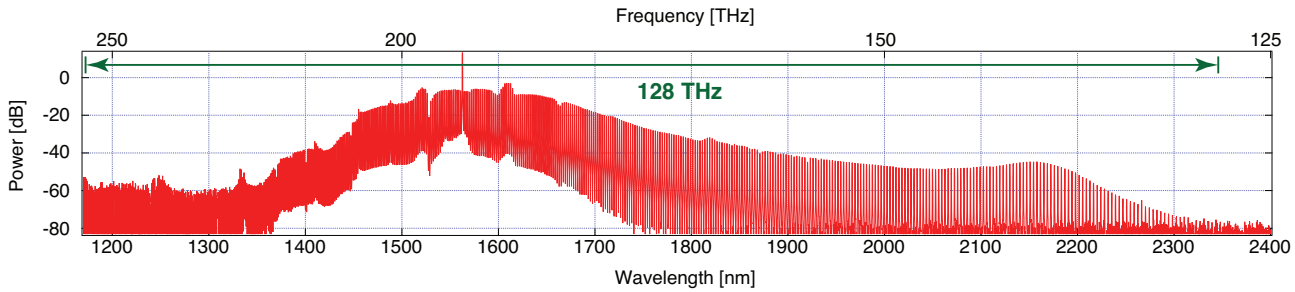

Figure 3.9: **Octave spanning comb at 1550 nm:** Optical spectrum of octave-spanning parametric frequency comb generated in a silicon nitride ring resonator.

The output is collected using an aspheric lens and sent to an optical spectrum analyzer (OSA).

The pump wavelength is tuned into a cavity resonance, such that a stable "thermal lock" is achieved [115]. As the power in the microring is increased above threshold, the oscillation of a signal/idler pair occurs. Further increases in power lead to cascaded FWM, resulting in the generation of comb lines, and higher-order degenerate and nondegenerate FWM processes filling in adjacent cavity modes and increasing the comb line density. The parametric frequency comb spectrum from the microring resonator is shown in Fig. 3.9. The total spectrum is acquired using two OSA's, with spectral ranges of 600-1700 nm and 1200-2400 nm. The comb lines are generated over a wavelength span of 1180 nm, from 1170 nm to 2350 nm, which corresponds to an octave of optical bandwidth.

Next, we investigate the tuning performance of the parametric comb by monitoring a 5-nm section of the comb centered at 1650 nm using an optical spectrum analyzer. Figure 3.10 shows that the three comb lines are red-shifted as the incident power is varied from 1.3 W to 2.1 W. As the pump power is increased, the resonance experiences a red-shift, which is primarily due to ther-

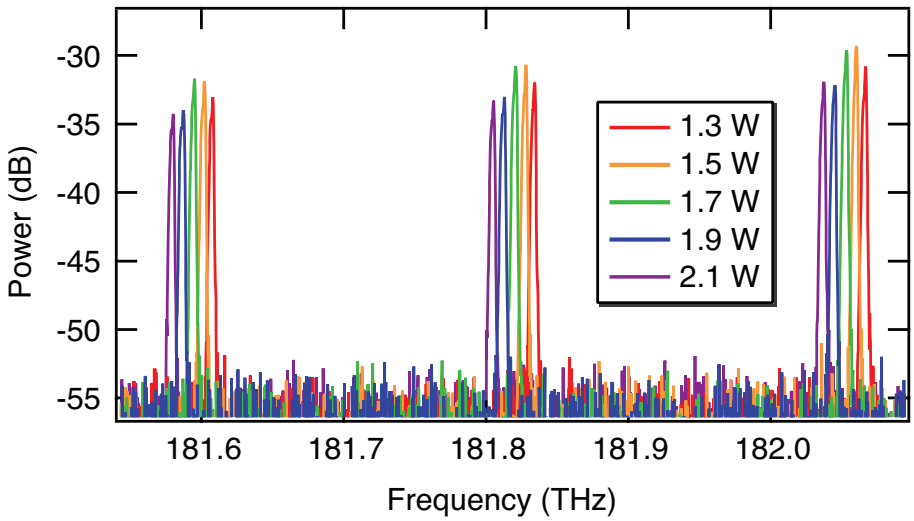

Figure 3.10: **Tuning:** Demonstration of tuning performance of the parametric comb. A 5-nm segment of parametric comb is monitored at various incident powers from 1.3 to 2.1 W. The frequency tuning range for this range of powers is 29 GHz, and we estimate the change in the comb spacing to be 36 MHz..

mal effects. We observe a frequency tuning range of 29 GHz and estimate that the comb spacing undergoes a 36-MHz shift over the range of incident powers used. This tuning range can be further increased with higher pump powers and higher Q-factor resonators.

Lastly, we characterize the RF noise of the parametric comb. The experimental setup is shown in fig. 3.11. We use a wavelength division multiplexer to filter a 9-nm section of the comb spectrum that does not include the pump wavelength. The filtered portion is detected by a fast photodiode, and the electrical signal is sent to an RF spectrum analyzer. We simultaneously monitor the remaining spectrum using an optical spectrum analyzer, and Fig. 3.12 shows the RF and optical spectra. As the pump wavelength is red-shifted into resonance, the RF noise decreases by 30 dB (red curve to yellow curve), and we observe modulations in the optical spectrum [Fig. 3.12(c) and (d)]. We observe a peak

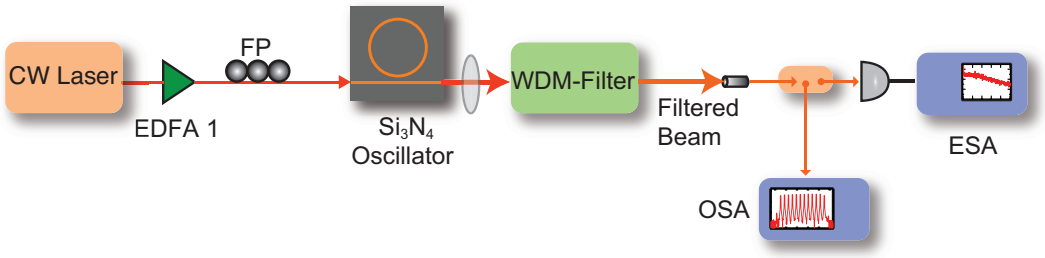

Figure 3.11: **RF characterization setup:** The experimental setup used for generating an octave spanning microresonator based comb and characterizing the radio-frequency (RF) spectrum as the comb is generated. A single-frequency diode laser centered at 1562 nm is amplified with a erbium-doped fiber amplifier (EDFA) and inject it into a nanowaveguide using a lensed fiber. The input polarization is adjusted to quasi-TE using a fiber polarization controller. The output is collected with a free-space objective, fiber coupled (using FC) and sent to a wavelength division multiplexer (WDM) to filter a 9-nm section of the comb spectrum that does not include the pump wavelength. The filtered portion is detected by a fast photodiode, and the electrical signal is sent to an RF spectrum analyzer. We simultaneously monitor the remaining spectrum using an optical spectrum analyzer (OSA).

near 11 MHz, which we attribute to relaxation oscillations of the pump laser and we are currently investigating this issue further. As the pump is further red-shifted into the resonance, the the power in adjacent comb lines equalizes [Fig. 3.12(e)], while maintaining the low-noise state. The cause of this drop in noise is an indication of the comb transitioning into a phase-locked state as is described later in this chapter.

In conclusion, we demonstrate octave-spanning parametric frequency comb generation in a monolithically integrated silicon nitride microring resonator from a single-frequency cw laser. We achieve a 128-THz comb bandwidth with a comb spacing of 226 GHz. Although, we have been able to successfully generate an octave spanning comb, it is not possible to do an *f-2f* measurement with

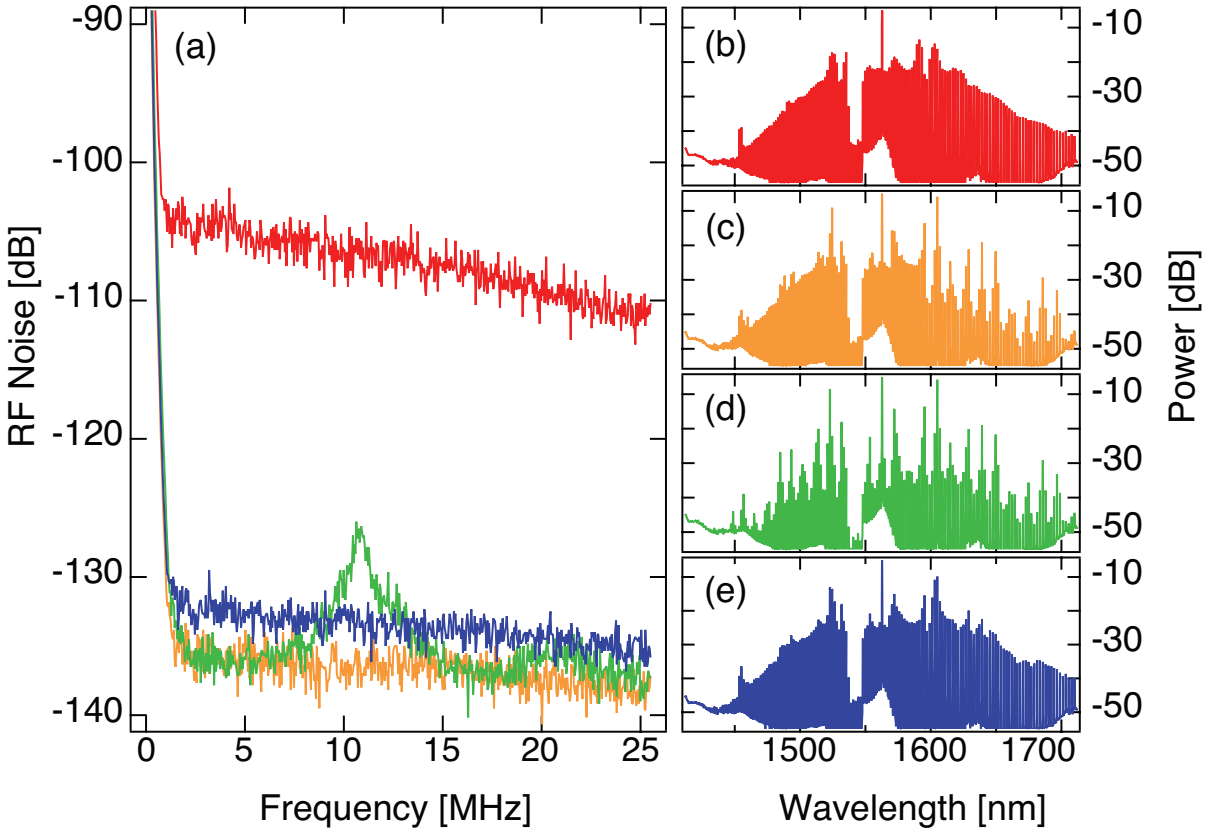

Figure 3.12: **RF dynamics:** (a) RF noise spectral of parametric frequency comb. A 9-nm portion of the optical spectrum is filtered from the comb for RF measurement. The noise is measured at four different pump detunings over 10 GHz as the pump is tuned into the cavity resonance. (b)-(e) show the corresponding optical spectra after the 9-nm section is filtered.

this comb. As we have reported, the comb lines at the far end have significantly lower optical power than the lines in the center. This implies that external amplifiers will have to used for increasing the power in the corresponding lines such that frequency doubling is possible. The addition of external amplifiers also mean there is addition of extra noise that might lead to loss of coherence and low-noise properties of the comb. Theoretical simulations using the LL equation model (as mentioned in section 3.2.2 of this octave spanning comb system reveals that a comb wider than an octave is necessary for $f - 2f$ locking [104]

and that the far ends of the comb are not necessarily coherent due to dispersive wave generation.

For a microresonator based comb to be applied to applications in spectroscopy and metrology, the comb must first be fully stabilized and the noise properties characterized. Though, the results described in this section provide a proof of principle demonstration that broadband comb generation on-chip offers potential for a fully integrated, stabilized, compact optical frequency comb source with applications in spectroscopy, metrology, high-speed communications, and on-chip optical clocks. While the combs generated here were in the near IR, dispersion engineering of the silicon nitride ring resonator should enable generation of frequency combs at visible and at mid-IR wavelengths, allowing for unmatched flexibility in selecting the operating pump wavelength.

3.2.4 One micron comb

It has been established that dispersion engineering of microresonator geometries allow for using a pump at a different wavelength for generating a frequency comb [116, 117], but it still remains a challenge to design a device using the same device platform with the flexibility of pumping at different wavelengths and generating an ultra-broadband frequency comb in the visible or near-IR wavelength range with a desired comb spacing. For example, parametric comb generation was demonstrated in a CaF_2 cylindrical and spheroid resonators with a 794-nm pump but with a relatively narrow ~2 THz [116] bandwidth. In a microtoroid [117] or microsphere [42] geometry, the dispersion is dependent on the size and shape of the cavity. Since the free spectral range (FSR) is

determined by the cavity size, it is difficult to design a structure where the pump wavelength and FSR can be freely determined. In contrast, in a silicon-nitride microring resonator, the dispersion and FSR can be controlled separately. In the previous section we have shown ultra-broadband(octave-spanning) comb generation with pump at 1550 nm [112]. In this section, we report the multi-wavelength pumping functionality of the silicon-nitride microresonator platform and report the first demonstration of optical parametric oscillation and generation of an ultra-broadband frequency comb at 1-μm in a silicon nitride ring resonator by dispersion engineering FWM gain in the 0.8-1.5 μm wavelength range [118].

Dispersion engineering for comb generation

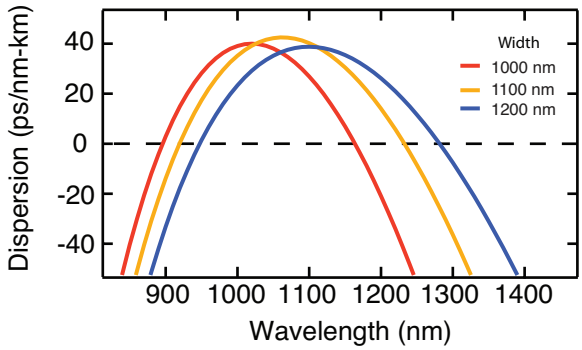

Figure 3.13: **Dispersion engineering for 1-μm comb:** Simulated dispersion curves for the fundamental TE-mode of a silicon-nitride waveguide with 600-nm height and with widths of 900, 1000, 1100, and 1200 nm.

The dispersion is determined by the material and the waveguide cross-sectionional geometry, and the FSR is determined by the circumference of the microring. Figure 3.13 shows the simulated dispersion curves for silicon-nitride waveguide with varying cross-sections for the fundamental TE mode. The

curves show that decreasing the width of the waveguides, shifts the anomalous dispersion region to lower wavelengths. The peak of the anomalous GVD occurs for a width of 1100 nm and then decreases with further reduction in waveguide widths, which is detrimental for wide bandwidth phase-matching and FWM.

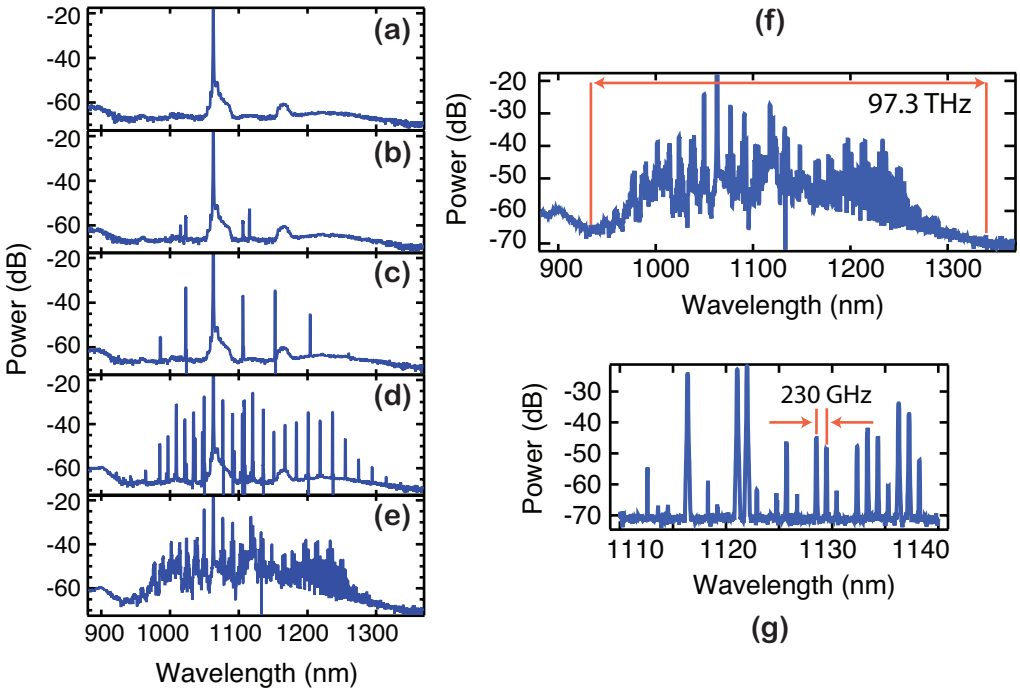

Figure 3.14: **Comb dynamics:**(a-e) Comb generation dynamics (from top to bottom). As the power oscillating inside the microring increases and threshold is reached, cavity modes which are maximally phase-matched experience gain and grow. When the pump is tuned deeper into resonance and power in the side modes increase further, cascaded four-wave mixing takes place, leading to multiple cascaded oscillations and development of a wide bandwidth comb. (f) Optical spectrum of frequency comb generated pumping at 1064-nm. The comb spans 97.3 THz with a spacing of 230 GHz. (g) A zoomed in spectrum of the higher wavelength end. Comb teeth do not appear at every FSR due to lack of proper phase-matching and power buildup.

Experiment and discussion

In our experiment, we use a single-frequency continuous wave laser centered at 1064 nm and amplified to 2 W using an Ytterbium doped fiber amplifier (YDFA). The polarization of the laser is adjusted to quasi-TE and sent into a bus-waveguide for coupling into the microring resonator. Both the coupling waveguide and the microring are monolithically fabricated. The coupling waveguide and the ring have a cross-section of 600 nm by 1150 nm, which gives a broad region of anomalous GVD, centered at the pump wavelength of 1064 nm. The ring has a 115-μm radius which corresponds to a 230-GHz FSR. The loaded-quality factor$Q$ of the resonator is 200,000. The output light is collected using an objective and sent to an optical spectrum analyzer. Figure 3.14(a-e) shows the optical spectrum of the comb generation dynamics as the pump wavelength is tuned into a cavity resonance. As the power oscillating in the microring increases, the cavity modes that are multiple FSRs away from the pump, experience the maximum FWM gain and oscillate at a threshold power of 80 mW. With further increase in power cascaded FWM occurs resulting in multiple oscillations and minicomb formation [Fig. 3.14(d)]. The density of comb lines increases as the pump frequency is tuned deep in the cavity resonance and adjacent cavity modes are filled through multiple higher-order degenerate and non-degenerate FWM processes [Fig. 3.14(e)].

The optical spectrum of the fully formed comb is shown in Fig. 3.14(f). The 230-Ghz-spaced comb lines are generated over a wavelength span of 406 nm which corresponds to 97.3 THz. Figure 3.14(g) shows the zoomed in optical spectrum of the higher wavelength side of the frequency comb. We observe that the comb teeth are not formed at every FSR. This can be explained by analysing

the relation between the threshold power for oscillation and the intrinsic-Q of the resonator, which is given by

$$P_{th} = \frac{2\pi^2 n_g^2 R A_{eff}}{\lambda n_2 Q_i^2}, \tag{3.18}$$

where, P_{th} is the threshold power, n_g is the group index, R is the radius of the resonator, A_{eff} is the effective area of the mode, λ is the pump wavelength, n_2 is the nonlinear refractive index, and Q_i is the intrinsic quality factor of the resonator. We have previously observed that successive resonances of a ring resonator neither have the same Q or extinction [119]. Therefore, the relatively low Q-factor of the resonances lead to less power build-up in the corresponding side modes as the power inside the ring is directly proportional to the Q. This prevents the modes from reaching threshold and acting as pump modes for further frequency conversion which leads to missing comb lines. Further, the low anomalous dispersion leads to improper phase-matching in the side modes which causes insufficient FWM mixing gain and preventing further comb line formation. To investigate this issue further, we dispersion engineer and fabricate devices with larger anomalous dispersion.

Figure 3.15(a) shows the dispersion curves for a silicon-nitride waveguide with a cross-section of 725 nm by 1000 nm with TE and TM modes. With the pump at 1064 nm, the generated frequency comb is shown Fig. 3.15(b). The polarization of the pump was set to quasi-TM in this case due to the lower coupling and waveguide losses as compared to the quasi-TE polarization input for the microring resonator. The loaded-Q is 250,000 which is higher than the previous case and as expected, we observe a lower threshold power of ~40 mW for oscillation. The frequency comb spans 55 THz with an FSR of 230 GHz. In com-

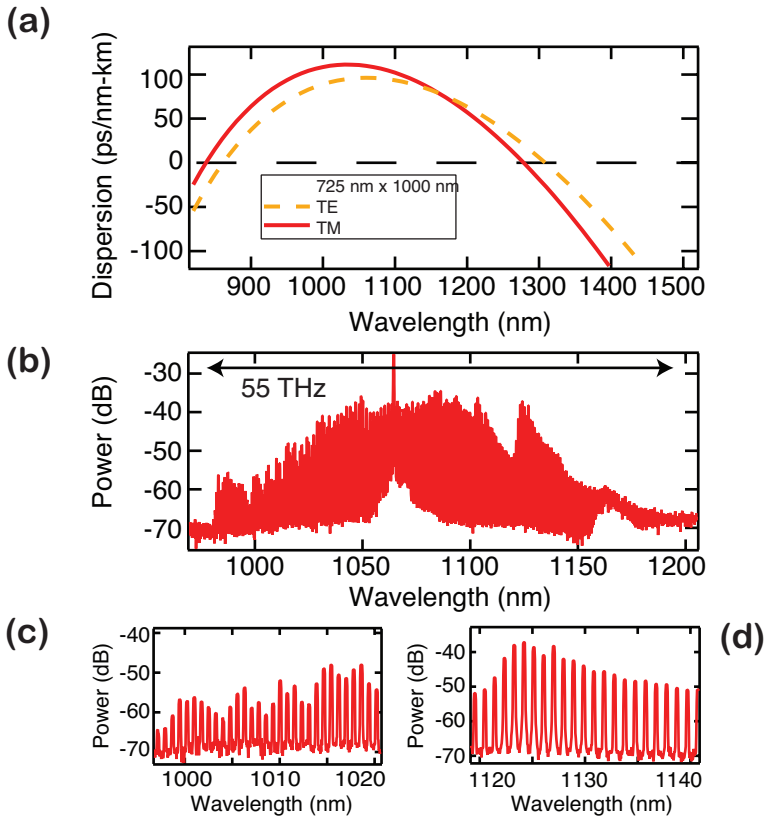

Figure 3.15: **Dispersion engineering for fully-filled 1-μm comb:**(a) Simulated dispersion curves for the fundamental TE-mode (dashed yellow) and TM-mode (solid red) of a silicon-nitride waveguide with 725-nm height and 1000-nm width. (b) Broadband frequency comb at 1 micron spanning 55 THz and 230-GHz comb spacing. (c-d) Zoomed in of low wavelength and high wavelength region of the frequency comb showing fully developed comb lines at every cavity mode.

parison to the previous case, the obtained comb bandwidth is smaller. Due to the higher anomalous dispersion, cavity modes require more power for phase-matching and FWM gain. The zoomed in viewgraphs [Fig. 3.15(c-d)] show that comb lines are formed at every FSR due to proper phase-matching and power buildup at the lower and higher wavelength ends of the frequency comb.

In conclusion, we demonstrate broadband frequency comb generation in

a monolithically integrated silicon-nitride microring resonator using a single-frequency laser at 1064 nm. We achieve a 55-THz comb bandwidth with a FSR of 230 GHz. Dispersion engineering a wider anomalous region around 1064-nm, in a microresonator with higher Q-factor will allow for generation of an octave spanning comb for comb stabilization using existing frequency stabilization equipment and techniques. Our results illustrate how the microring geometry in silicon nitride can be readily extended to broadband frequency combs pumped at near-IR wavelengths centered at 1 μm that can offer several advantages such as the existence of commercially available technology for *f-2f* stabilization, the potential spectral overlap with optical frequency standards and to generate frequency-doubled comb in the visible spectrum for astronomical applications [**?**].

3.2.5 Low repetition rate comb

Optical frequency combs find application in direct frequency synthesis. As mentioned in section 3.2, microresonator-based frequency combs can form a direct link between microwave and optical frequency. Generation of microwave signals ≥10 GHz is challenge using standard microwave technology. Optical frequency combs provide an easy route towards low-noise, ultrastable microwave sources. The silicon nitride platform for generating microwave signals via optical frequency combs is advantageous since the dispersion and FSR are independently tunable parameters. Although, in order to directly link the optical regime and the microwave regime, the repetition rate of the comb must be within the detection range of fast photo-diodes (generally a maximum of 50 GHz). To achieve FSRs 100-GHz and below, we redesigned the microresonators, as shown

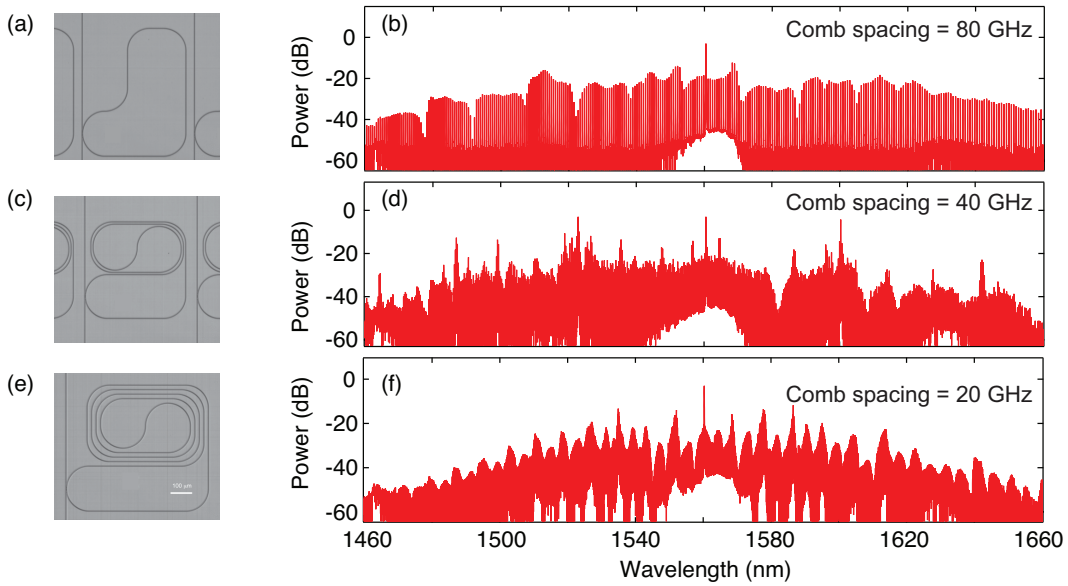

Figure 3.16: **Microresonators designs for low-repetition rate combs:**(a, c, e)Figure shows micrographs of spiral resonators and the corresponding optical frequency combs. (b, d, f) Optical spectrum of frequency combs with FSRs of 20-, 40-, 80-GHz are shown.

in fig. 3.16(a, c, e), from the traditional ring geometry to a spiral geometry [119]. To ensure that the dispersion is not influenced by the curved sections compared o the straight portions of the resonator, the minimum bend radius was kept to be more than 100 μm. Additionally, keeping a semi-ring at the coupling region ensures precise control over the coupling parameter to enable critically coupled devices. Further, the enclosed spiral loop reduces device footprint and helps avoid waveguide losses due to stitching errors. The spiral microresonators were then used to generate frequency combs as shown in fig. 3.16(b, d, f).

3.3 Frequency and time dynamics of frequency comb

In this section, we report the simultaneous investigation of the temporal and optical and radio-frequency spectral properties of a parametric frequency combs generated in an integrated silicon-nitride microresonators and observe that the system undergoes a transition to a mode-locked state and that ultrashort pulse generation is occurring [120]. From a 25-nm filtered section of the 300-nm comb spectrum, we observe sub-200-fs pulses at a 99-GHz repetition rate. To illustrate the flexibility of this platform in terms of controlling the pulse repetition rate, we show that by operating with a shorter microresonator, similar duration pulses can be produced at a 225-GHz repetition rate. Simulations using the LL model and calculations indicate that the pulse generation process is consistent with soliton modelocking, which is consistent with very recent work involving comb generation in MgF_2 microresonators [105]. These results demonstrate that such parametric frequency combs can serve as a source of ultrashort laser pulses that, depending on the pump laser and material system, could produce ultrashort pulses from the visible to the mid-infrared at repetition rates in the GHz to THz regimes.

3.3.1 Temporal measurement technique: Intensity autocorrelation

For measuring a periodic signal, such as the temporal response of an optical frequency comb, or an optical pulse, the detector should have a resolution far better than the width of the pulse. The accuracy of our measurement is then limited

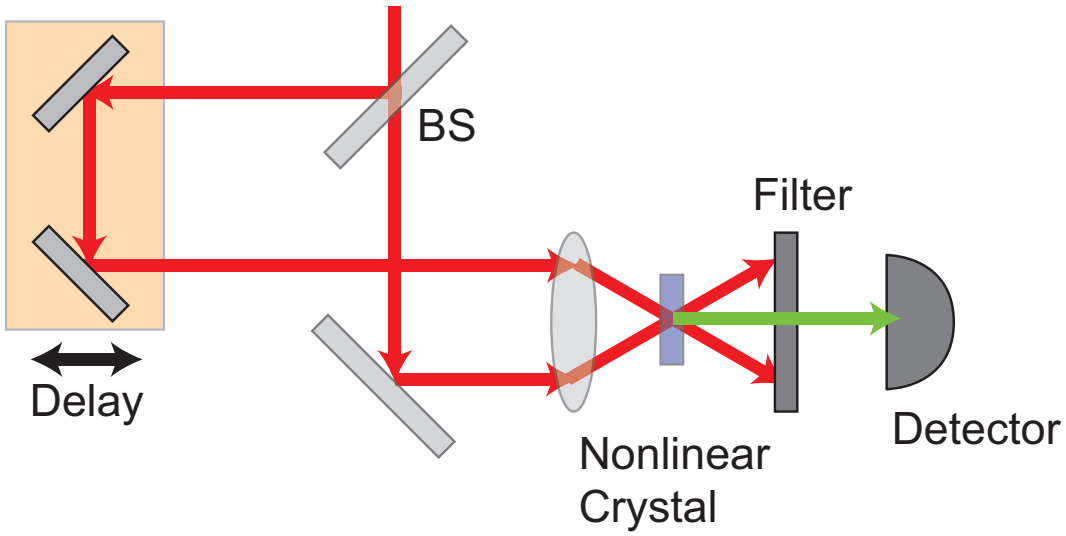

Figure 3.17: **Intensity autocorrelator:** Schematic of an intensity autocorrelator.

to the width of the detector window. Ultra-short pulses that are generated from modelocked lasers and supercontinuum-based frequency combs are among the shortest ever temporal signals that have been generated [121]. Measuring such pulses are a challenge. A lot of research has been devoted to developing techniques and methods for such temporal measurement [121, 122]. At the heart of each measurement technique is simply the measurement of the correlation between two pulses[123, 122]. The correlation function provides a measure of how similar two functions are for different values of an independent variable. Mathematically a correlation of two functions is given by:

$$(a \star b)(t) = \int_{-\infty}^{\infty} a * (\tau) b(t + \tau) d\tau \tag{3.19}$$

where a^* is the complex conjugate of the function a. From eq. 3.19, if $a(t) = b(t)$ the integral is a measure of the similarity of a function with a time delayed copy of itself. This is the "autocorrelation" function for $a(t)$. An optical autocorrelation is a measure of the similarity of a pulse with itself. Optical autocorrelations as a method for characterising optical pulses was first reported in 1966-67

[124, 125]. Typical detectors have rise and fall time ~1 ns due to limitations in the associated electronics. Any pulse shorter than ~1 ns needs a specialised detection scheme [121].

In an intensity autocorrelator as shown in fig. 3.17, a beam splitter splits an incoming pulse into two pulses, which are then focused and sent into a crystal with a $\chi^{(2)}$ nonlinearity. The arm length difference and thus the relative timing of the pulses can be mechanically adjusted via the variable delay line. Different kinds of delay lines can be used, e.g. using rotating glass blocks or mirrors mounted on loudspeakers. If the arm length difference is made small, so that the pulses meet in the nonlinear crystal, the process of sum frequency generation occurs, leading to an output with a shorter wavelength. If the relative time delay is increased, so that the overlap of the two pulses in the crystal is reduced, the mixing product becomes weaker. For measuring the pulse duration, the power of the mixing product is recorded as a function of the arm length difference. The second harmonic generation (SHG) crystal will produce light that is at a frequency twice that of the input light with a field given by. [71]

$$E_{SHG} \propto E(t)E(t-\tau), \tag{3.20}$$

where τ is the delay. Since the intensity is given simply by $2cn\varepsilon_0|E|^2$ the intensity of the second harmonic signal is proportional to the intensities of each of the pulses.

$$I_{SHG} \propto I(t)I(t-\tau) \tag{3.21}$$

Note here that only the cross term for the two pulses appears because we selectively measure the second harmonic light that is emitted along the optical axis. This is a non-collinear autocorrelation measurement and generates pulses with zero background. In a collinear autocorrelation measurement, the pulses have

background with a peak to background ratio of 3:1. The background level of the intensity autocorrelation provides important information about the coherence of the pulse. A collinear autocorrelation is similar to the autocorrelation of the sum of two uncorrelated functions but with an extra background term. Therefore, the measurement of the phase of the pulse is as important as the width of the pulse with an intensity autocorrelation to determine the properties of a temporal signal. Determining the pulse width from the intensity autocorrelation, I_{SHG}, requires some previous knowledge of the pulse shape. If a pulse shape is assumed, the autocorrelation width, τ_{ac}, is related to the pulse width, τ_{pulse}, by some deconvolution factor [126], k,

$$\tau_{ac} = k\tau_{pulse} \tag{3.22}$$

The deconvolution factor can be calculated for analytical pulse shapes or computed numerically for complicated pulses.The deconvolution factor is given in table 3.3.1 [126]. Typically a soliton modelocked laser generates pulses with a sech^2 pulse shape.

Pulse Shape	I(t)	$A^{(2)}(\tau)$	τ_{AC}/τ_p
Square Pulse	$1; \lvert t\rvert \leq \tau_p/2$ $0; \lvert t\rvert \geq \tau_p/2$	$1 - \lvert\frac{\tau}{\tau_{AC}}\rvert; \lvert t\rvert \leq \tau_{AC}$ $0; \lvert t\rvert \geq \tau_{AC}$	1
Gaussian	$e^{-[\frac{2\sqrt{ln2}t}{\tau p}]^2}$	$e^{-[\frac{2\sqrt{ln2}t}{\tau_{AC}}]^2}$	1.41
sech^2	$sech^2[\frac{1.7627t}{\tau_p}]$	$\frac{3}{sinh[\frac{2.7196\tau}{\tau_{AC}}]}[\frac{2.7196\tau}{\tau_{AC}}coth[\frac{2.7196\tau}{\tau_{AC}}] - 1]$	1.54

Table 3.1: Pulse shapes, pulse widths, autocorrelation trace widths for different pulse shapes

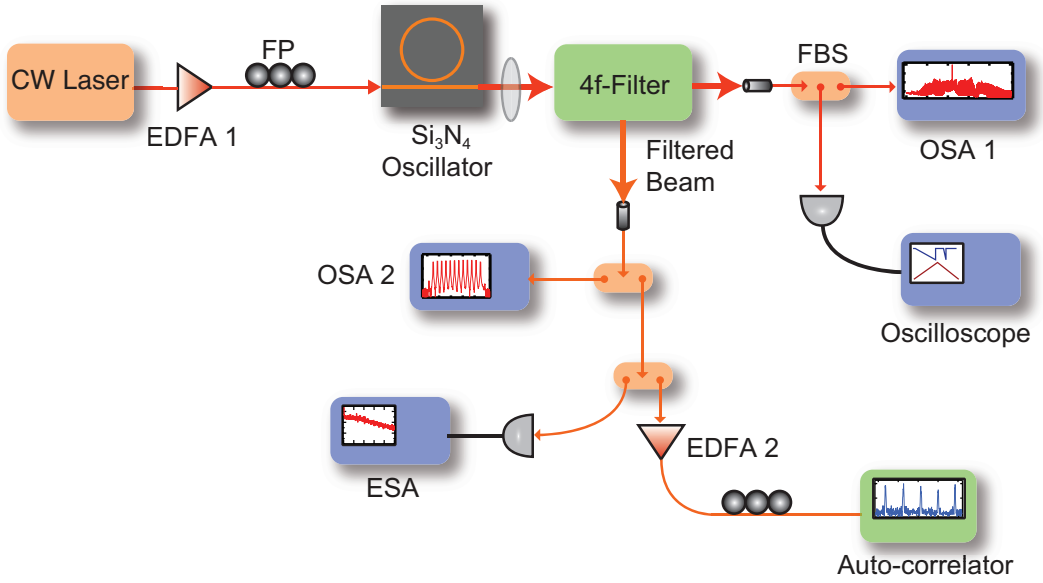

Figure 3.18: **Experimental setup for spectral and temporal characterization:** Figure shows the experimental setup for simultaneous spectral and temporal characterization of a microresonator-based optical frequency comb. The pump wave is derived by amplifying a single-frequency tunable diode laser at 1560 nm to 2.5 W using an erbium-doped fiber amplifier (EDFA) and coupling it into the bus waveguide using a lensed fiber. A 4-*f* shaper is used to filter a 25-nm section of the comb. The optical spectrum of this 25-nm section is measured using an OSA. This signal is then sent to an intensity autocorrelator for temporal characterization. An electronic spectrum analyser (ESA) was used to measure the RF spectrum.

Experiment and discussion

Development of ultrashort pulse sources has had an immense impact on condensed-matter physics, biomedical imaging, high-field physics, frequency metrology, telecommunications, nonlinear optics, and molecular spectroscopy [127, 128, 129, 126]. Numerous advancements of such sources have been made[130, 131, 132, 133, 134, 135], and in recent years there has been development of compact solid-state [136, 137] and semiconductor-based systems that

enable high-repetition-rate pulse generation [138, 139, 140, 141, 142]. However it remains a challenge to create a highly compact, robust platform capable of producing femtosecond pulses over a wide range of wavelengths, durations, and repetition rates. This section describes the experimental observation of mode-locked pulses generated from silicon nitride microresonator-based combs.

The experimental schematic is shown in Fig.3.18. The pump wave is derived by amplifying a single-frequency tunable diode laser at 1560 nm to 2.5 W using an erbium-doped fiber amplifier (EDFA) and coupling it into the bus waveguide using a lensed fiber. Both the microresonator and the bus waveguide are fabricated monolithically in a single silicon-nitride layer, allowing for robust and environmentally stable operation. We use a resonator with a cavity length of 1.44 mm, which corresponds to a 99-GHz FSR. A micrograph image of this resonator is shown in Fig. 3.19(a). The input polarization is adjusted to quasi-TE using a fiber polarization controller. As the coupled power in the resonator is increased the threshold for parametric oscillation of a signal/idler pair is reached. Further increases in the power coupled into the microresonator lead to cascaded FWM and higher-order FWM processes, resulting in the generation of numerous comb lines. The output is collected using an aspheric lens and sent to a 4-f shaper, which is used as an adjustable wavelength filter. The zero-order signal of the 4-f shaper is sent to an optical spectrum analyzer (OSA) to monitor the entire comb spectrum. The generated frequency comb spanning >300 nm is shown in Fig. 3.19(b).

To characterize the pulse dynamics, we filter a 25-nm section (32 comb lines) of the comb centered at 1546 nm and amplify it with an EDFA to sufficiently high power levels to allow for autocorrelation measurements. Our choice of

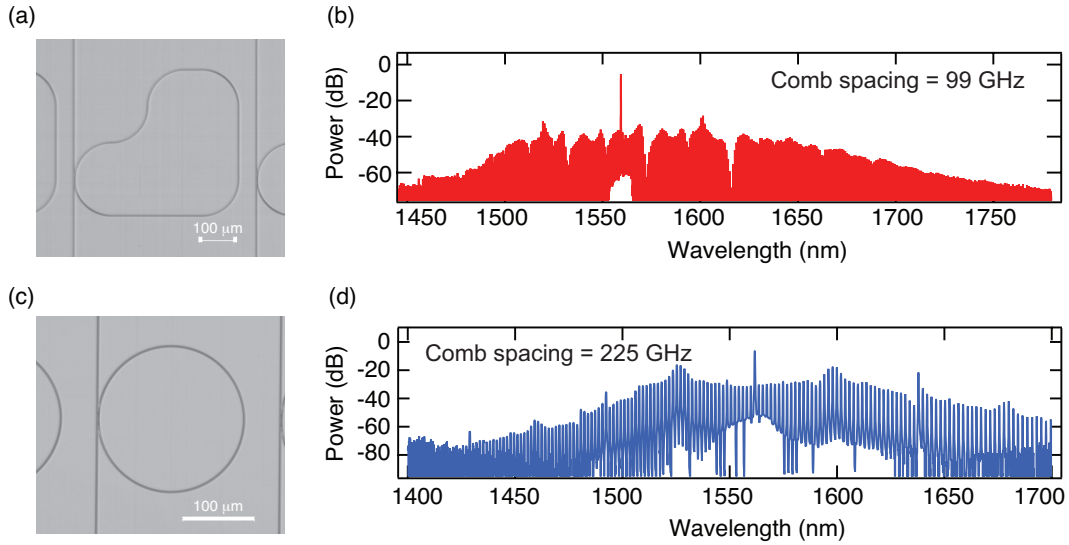

Figure 3.19: **SEM of microresonator and spectrum of generated comb:** (a) A scanning electron micrograph of a silicon-nitride resonator of length 1.44 mm coupled to a bus waveguide. The free-spectral range (FSR) is 99 GHz. (b) Optical spectrum of 99-GHz FSR frequency comb. (c) Micrograph of a silicon-nitride microresonator resonator of radius 112-μm with an FSR of 225 GHz. (d) Optical spectrum of a 225-GHz FSR frequency comb.

the 25-nm bandwidth corresponds to the bandwidth over which we could amplify the signal for characterization. An OSA trace of the filtered spectrum of the frequency comb is shown in Fig. 3.20(a). If the generated comb lines have a definite phase relationship, then a periodic pulse train in the time domain with a repetition rate given by the comb spacing should be observed. We investigate the temporal properties of the generated comb using an intensity autocorrelator, and Fig. 3.20(b) shows the normalized autocorrelation trace of the observed pulse train for the filtered comb shown in Fig. 3.20(a). The amplified output propagates through a length of single-mode fiber (SMF-28) for group-velocity dispersion compensation and is sent to the autocorrelator. The background noise due to amplified spontaneous emission due to optical amplifiers has been subtracted out. The pulse train has a 10.1-ps pulse period, which corre-

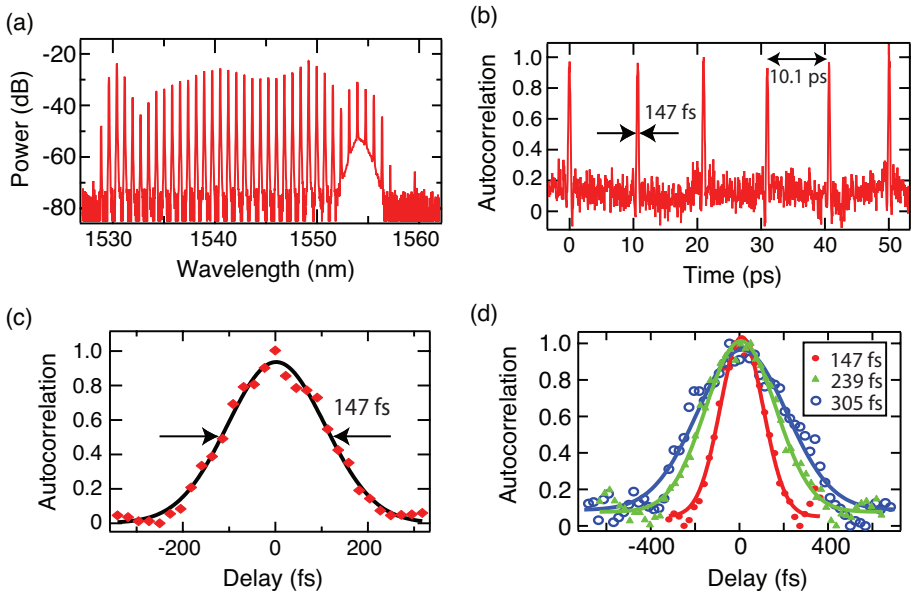

Figure 3.20: **Autocorrelation of 99-GHz-FSR comb:**(a) Filtered optical spectrum of a 99-GHz FSR frequency comb. The filter bandwidth is 25 nm. (b) Normalized autocorrelation trace of the pulse train obtained from the filtered comb. The pulse separation is 10.1 ps. (c) Zoomed-in view of a single pulse with a 147-fs FWHM pulse width. (d) Autocorrelation traces of pulses undergoing additional dispersive propagation through additional lengths of SMF. The observed broadening is consistent with that associated with coherent pulses.

sponds to the microresonator FSR of 99 GHz. Figure 3.20(c) shows a zoomed-in viewgraph of a single pulse. We measure pulse-widths as short as 147-fs (full-width half maximum, FWHM), which is close to the transform limit of 129 fs for the filtered bandwidth, assuming temporal sech^2 pulses. Using the entire comb bandwidth offers potential for generating single-cycle pulses with even shorter pulse-widths (i.e. 12 fs). We estimate the peak power of the pulses to be 1.2 W, and the temporal output is stable as long as the pump wavelength is on-resonance and there is no variation in coupling to the resonator. These results confirm our previous observation that the frequency comb transitions to a low-noise, phase-locked state [112], and we address this issue in greater de-

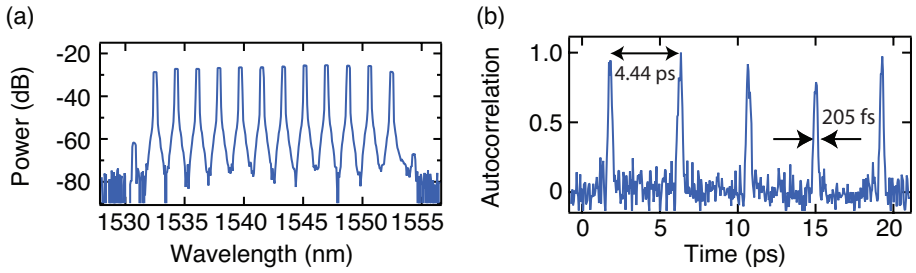

Figure 3.21: **Autocorrelation of a 225-GHz-FSR comb:**(a) Filtered optical spectrum of a frequency comb with 225-GHz free spectral range. (b) Normalized autocorrelation trace of pulse train obtained from the filtered comb. The pulse separation is 4.44 ps and the FWHM pulsewidth is 205 fs.

tail below. Passive modelocking and sub-200-fs pulse generation has since been observed in MgF_2 crystalline resonators [105].

To confirm that we are indeed generating pulses and not incoherent spikes from the microresonator-based frequency combs, we utilize temporal broadening in a dispersive media. We send the amplified 25-nm filtered section of the frequency comb output from the 1.44-mm-long microresonator cavity (corresponding to a 99-GHz FSR) through a few meters of single mode fiber (SMF) and temporally characterize the generated pulses using an intensity autocorrelator. Figure 3.20(d) shows the result of this measurement. We clearly observe temporal broadening of the pulses from 147 fs to 305 fs due to dispersive propagation through the additional lengths of SMF.

The silicon-nitride platform allows for unmatched flexibility in terms of controlling FSR, without changing the cavity dispersion. This allows for design and fabrication of multiple high-repetition-rate pulse sources with a specified pulse repetition rate all on a single chip. As an example, we use a 112-μm-radius ring-resonator, which corresponds to a 225-GHz FSR [see Fig. 3.19(c)-(d)]. The

optical spectrum of the corresponding comb is shown in Fig. 3.19(d) for the case in which we pump at 1559 nm. After filtering out a 25-nm section of the comb (14 lines) centered at 1543 nm [Fig. 3.21(a)], we amplify and measure the pulse train with the autocorrelator. We observe uncompressed 205-fs pulses at the expected 4.44-ps time interval [Fig. 3.21(b)], which corresponds to a 225-GHz repetition rate.

Next, we investigate the pulse formation dynamics in the parametric comb. Similar to our previous measurements, we filter a 25-nm section of the 225-GHz FSR comb. After splitting the filtered output, we monitor simultaneously the autocorrelation trace, the RF amplitude noise, and the optical spectrum of the generated comb. The results of the measurement are shown in Fig. 3.22. The leftmost column shows the autocorrelation traces of generated temporal waveforms [Fig. 3.22(a)], the middle column [Fig. 3.22(b)] shows the RF amplitude noise spectrum measured with an RF spectrum analyzer, and the rightmost column shows the optical spectrum [Fig. 3.22(c)] of the generated frequency comb corresponding to each stage of pulse formation as the pump wavelength is tuned into the microcavity resonance (top to bottom). The 25-nm filtered section of the frequency comb that is used for temporal characterization is represented in red color in each optical spectrum trace. As we tune the pump wavelength into resonance and more power is coupled into the microresonator, cascaded FWM takes place and comb lines are generated several FSRs away from the pump where the cavity modes experience the maximum FWM gain due to the interplay between the group velocity dispersion and nonlinearity. Similar comb generation dynamics in other platforms have also been observed [105]. Gradually, small clusters of comb lines (mini-combs) begin to appear centered at each of the cascaded FWM peaks. Simultaneously, a sinusoidal pulse train

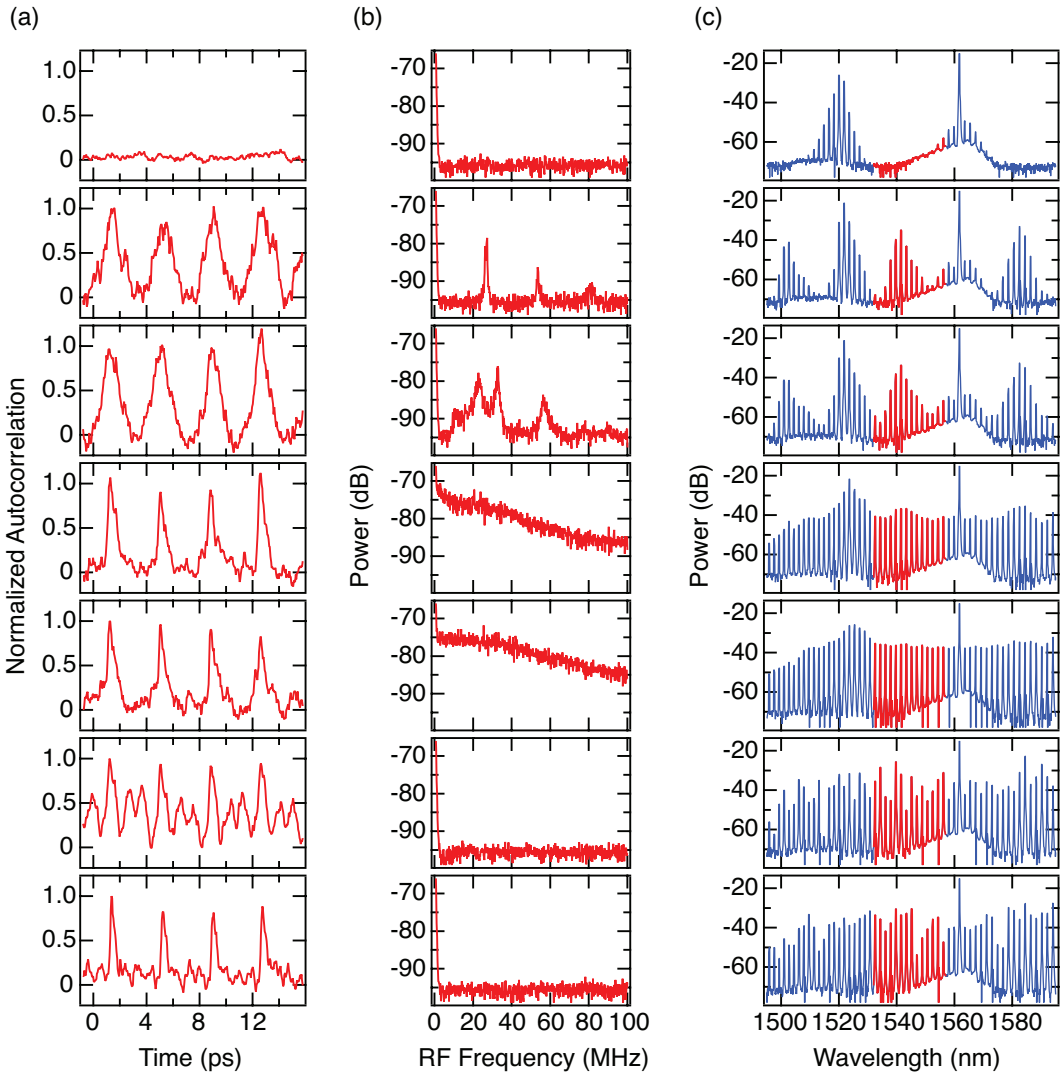

Figure 3.22: **Spectral and temporal dynamics:** (a) From top to bottom, pulse formation dynamics as the laser is tuned into resonance of the microresonator, thereby increasing the power coupled into the microresonator. (b) RF amplitude noise corresponding to each stage of pulse formation shown in column a to its left. (c) Optical spectrum of comb generation dynamics. Full comb is represented in blue, the filtered section of the comb used for pulse generation is shown in red.

appears, and several low-frequency peaks are observed in the RF domain. Further tuning into resonance leads to gradual equalization of the amplitude of the comb lines and reduction of pulse duration. However, at the same time, the number of peaks in the RF domain increases, and the linewidth of each peak broadens until it becomes a broad plateau. We attribute these peaks to beating between adjacent mini-combs due to the fact that, at this point in the generation process, the mini-combs are uncorrelated and could have different comb spacings and/or dc offsets [105]. As the comb lines equalize, the spectral overlap between the mini-combs becomes more extensive, resulting in a significant increase in the RF noise. However as we tune deeper into the resonance, the comb reaches a sudden transition stage where the RF noise suddenly decreases by >20 dB, which is a signature of phase-locking of the comb akin to modelocking in a femtosecond laser. The temporal waveform at this point is very sensitive to the amplitude of the individual comb lines, and we observe modulations in both the autocorrelation and the optical spectrum. Finally, as the pump is tuned further into resonance, we again observe equalization of the comb line amplitudes, and pulses with the shortest durations are generated.

To support the claim that this system exhibits soliton modelocking behavior similar to that in laser systems, we calculate the nonlinear length $L_{NL} = 1/\gamma P$ and dispersion length $L_D = \tau_p^2/|\beta_2|$ within the resonator for the pulses generated from a 100-nm bandwidth of the 99-GHz-FSR comb, where $\lambda = 1560$ nm is the center wavelength, γ =1.09 $\mathrm{W^{-1}m^{-1}}$ is the nonlinear parameter, $\tau_p = 14.5$ fs is the pulse duration, and $\beta_2 = -0.064$ $\mathrm{ps^2/m}$ is the group-velocity dispersion. The peak power $P = 633$ W for determining L_{NL} of the 100-nm section for this calculation is estimated based on the peak power of the filtered 25-nm section of the comb and by taking into account the spectral shape of the comb excluding the pump.

The estimated average power circulating in the ring is consistent with the theoretically calculated value including all possible losses. The calculated soliton number $N = \sqrt{L_D/L_{NL}}$ is 1.5, which strongly suggests that the system is operating under soliton modelocking conditions. Although there have been previous investigations for modelocking in microresonator-based combs [107, 143], the underlying mechanism in our system remains unknown. One possible mechanism could be that the relatively high optical intensities circulating inside the cavity lead to local changes in the nonlinear refractive index resulting in greater spatial confinement of the pulse and reduced losses since there is less absorption at the core-cladding interface. Alternatively, the pulse train may be produced due to the formation of temporal cavity solitons [144], where contributions from dispersion and loss are compensated by nonlinearity and a coherent driving beam [144], and recent experiments using MgF_2 microresonators support this conclusion [105]. Theoretical simulations using the LL equation model for this system further confirm that modelocking indeed occurs in this system [104].

3.3.2 Time-lens technique

We further confirm that the temporal waveforms obtained from the intensity autocorrelation using the 99-GHz FSR comb are indeed coherent, mode-locked pulses and not coherence spikes utilizing a temporal magnifier. This is an independent measurement technique based on time-lens technology that allows for single-shot characterization of ultrafast temporal waveforms using a GHz-bandwidth real-time oscilloscope through temporal stretching of the input waveform [145, 146]. We send a 7-nm filtered section of a 99-GHz-FSR frequency comb to the time-magnifier. The temporal magnifier system outputs tempo-

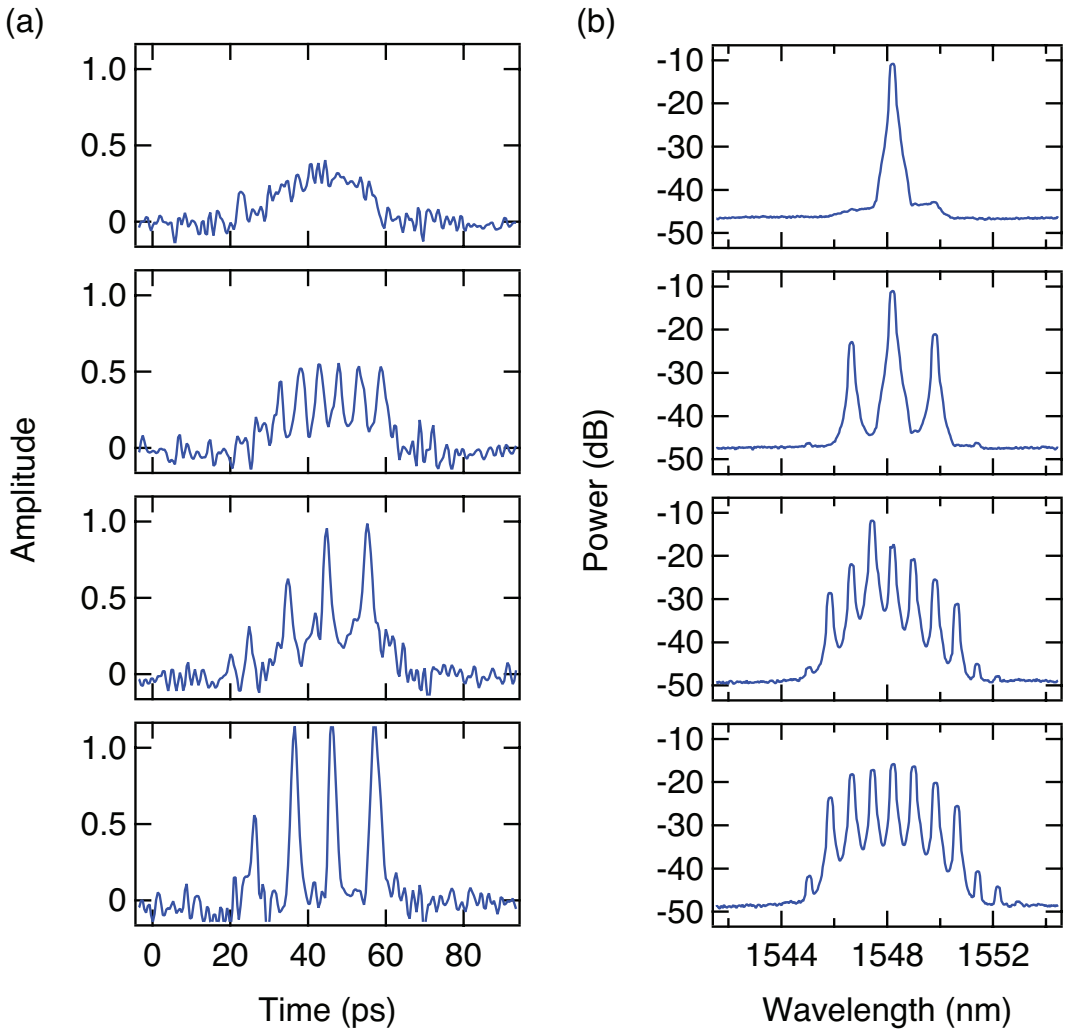

Figure 3.23: **Time dynamics using time magnification technique:** (a) Single-shot characterization of temporal evolution (top to bottom) of pulses generated in a microresonator with 99-GHz FSR measured with an ultrafast temporal magnifier and a real-time oscilloscope. (b) Spectral evolution of the generated frequency comb as the pump is tuned into resonance and the power inside the microresonator increases.

rally stretched snap-shots of the input waveform, which are recorded using a real-time oscilloscope. The system is further detailed in Okawachi, *et al.* [146]. Figures 3.23(a) and 3.23(b) (from top to bottom), respectively, show the temporal and spectral evolution of a frequency comb generated using a 99-GHz-FSR microresonator. We observe that, as the pump wavelength is tuned into resonance and a single comb line is generated, there is a cw temporal output. When the pump is tuned further into resonance, we observe three comb lines in the spectral domain, corresponding to a pulse repetition rate that is twice the FSR of the microresonator. As the pump is further tuned in, we see that every adjacent comb line is filled in. However, at this point, in the time domain, we observe a distorted pulse train with a significant background, indicating that the pulse train is not phase-locked. Finally, as we tune into the deepest point of the resonance, we observe narrow pulse-width with no background, indicating the onset of modelocking. These results clearly validate the existence of coherent and mode-locked pulses generated from microresonators pumped with a single-frequency cw pump.

In conclusion, we have investigated the temporal and spectral properties of parametric combs generated in silicon-nitride microresonators and observe a transition to passive modelocking of the comb consistent with soliton-pulse formation, resulting in the generation of 160-fs pulses at a 99-GHz repetition rate. This platform offers the prospect of producing pulses from 10 fs to a few ps at repetition rates from 10 GHz to > 1 THz and over a wavelength range of 0.8 6 μm.

3.4 Summary and Conclusion

In summary, by utilizing the strong confinement of light in nanofabricated silicon nitride microresontors along with the enhancement due to the high-optical-Q, we report the first demonstration of an octave spanning optical frequency comb via cascaded four-wave mixing. Next, we show the unparalleled flexibility of this platform to independently tune the dispersion and the FSR to generate combs with pumps at different wavelengths and have different FSRs. Finally, we demonstrate the first observation of sub-200-fs pulses from an on-chip, silicon-based frequency comb source. We observe that as the frequency comb develops, a transition occurs into a stable, low-noise phase-locked state similar to that in a mode-locked femtosecond source. This demonstration represents a significant advancement towards the development of integrated, stabilized, and compact ultra-high repetition-rate femtosecond sources. Furthermore, since the FSR and the cavity dispersion can be independently controlled, this system allows for building numerous ultrafast sources on the same chip with unparalleled flexibility in repetition rates and operating wavelengths from the near visible to the mid-infrared.

CHAPTER 4

INTEGRATING RUBIDIUM WITH MICRORESONATORS

4.1 Introduction

The previous chapters describe the applications of two different kind of material platforms for performing nonlinear optics at low and high power levels. This chapter describes an effort towards integrating the silicon nitride microresonator platform with rubidium vapor to exploit the resonant enhancement due to the high-Q of the resonators and the high nonlinearity of Rb [147]. We design microresonators suitable for integration with Rb and report the first evanescent interaction of Rb with silicon nitride nanowaveguides.

4.2 Experimental setup

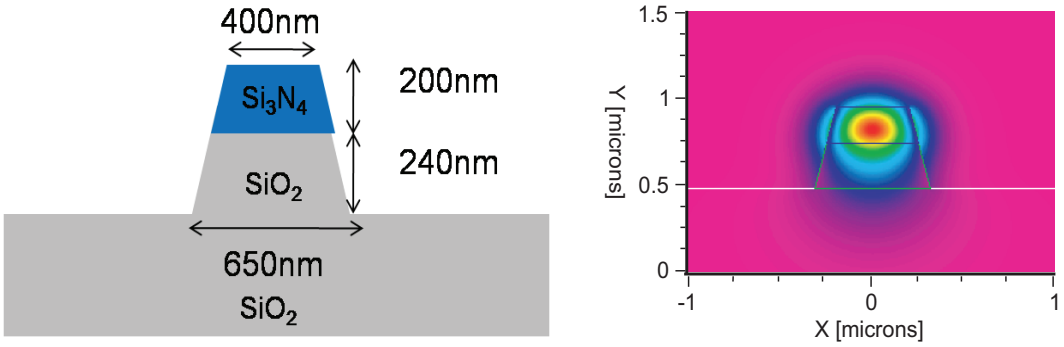

Figure 4.1: **Silicon nitride waveguide for evanescent interaction with rubidium:** (a) Illustration of waveguide design. The silicon nitride waveguide is 400 nm in width and 200 nm in height. (b) Optical mode profile of the of waveguide showing 13.2% light outside such that interaction with Rb is possible.

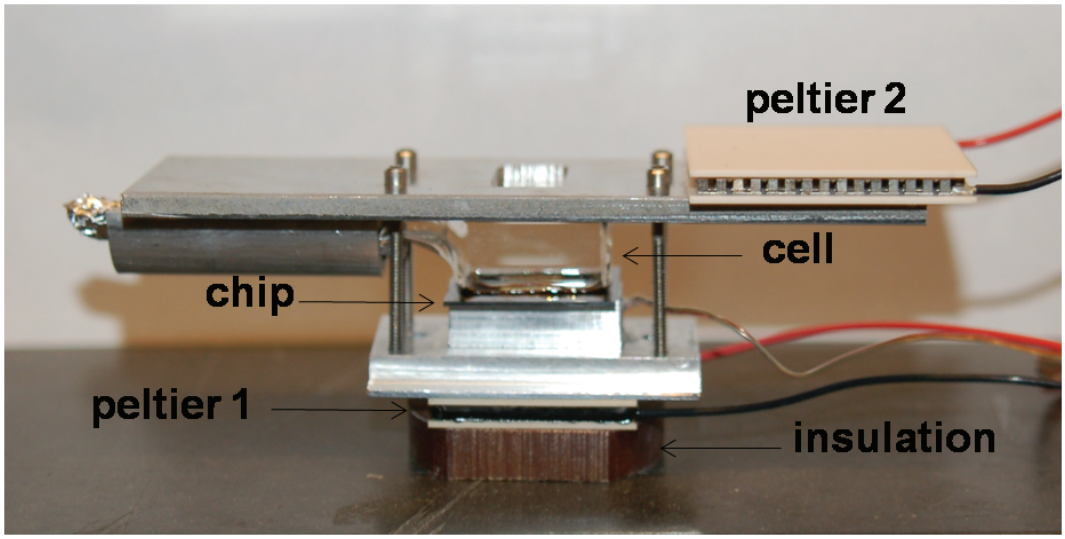

Figure 4.2: **Schematic of Rb-chip experimental setup:** Photograph of the cell-chip unit. A small glass dome is bonded to a chip with waveguides fabricated on it. The cell-chip is then evacuated by a turbo pump through the small glass stem. Rubidium is then loaded via the same stem, and the cell-chip is sealed by heating and pinching off the stem. The coupling ends of the waveguide lie outside the dome, enabling simple coupling to the waveguides via an objective or a fiber lens. The vapor density inside the cell is regulated using a small oven that does not interfere with external objectives or fiber lenses.

The design and field mode of the silicon nitride nanowire is shown in fig. 4.1(a, b). The nanowaveguide has a 200 nm thick silicon nitride layer as shown in fig. 4.1(a). The waveguide is 400 nm in width at the top with 650-nm width at the bottom. This difference is due to the etching process which leads to angled waveguide sides. A 240-nm thick oxide layer is used to isolate the high-index guiding region from the silicon chip surface. Integrating the simulation of the guided mode shows that 13.2% of the guided intensity is outside of the waveguide and capable of interacting with ambient vapor. This interaction is observed using the cell-chip design shown in fig. 4.2. A small glass dome is bonded to a chip with waveguides fabricated on it. The cell-chip is then evac-

uated by a turbo pump through the small glass stem. Rubidium is then loaded via the same stem, and the cell-chip is sealed by heating and pinching off the stem. The coupling ends of the waveguide lie outside the dome, enabling simple coupling to the waveguides via an objective or a fiber lens. The vapor density inside the cell is regulated using a small oven that does not interfere with external objectives or fiber lenses. The oven typically operates between 100-150°C. We have found that optical depths >100 cm^{-1} can be generated. Spectroscopy is performed using an external cavity diode laser (ECDL) that is scanned across the D1 line of the Rb vapor, and we monitor the transmission of the collected output with a photodiode. A pick-off of the ECDL beam is directed into the cell, above the chip, and also monitored on a photodiode. In this manner spectroscopy of the vapor in free space and from the guided mode can be performed simultaneously.

4.3 Results

A spectroscopic measurement of the D2 lines of Rubidium is shown in fig. 4.3. Absorption from the Rb lines is considerably greater for the free-space beam due to the fact that most of the guided light is inside of the silicon nitride waveguide. The waveguide-measured resonances also exhibit noticeable broadening and shifting with respect to their free-space counterparts. These features are consistent with the homogeneous broadening due to transit-time effects, inhomogeneous broadening, and shifting due to Van der Waals interactions between the atoms and the surface of the waveguide.The maximum observed on-resonance absorption for light passing through the nano-waveguides corresponds to an optical depth of 2. Further optimization of the cell should allow for larger op-

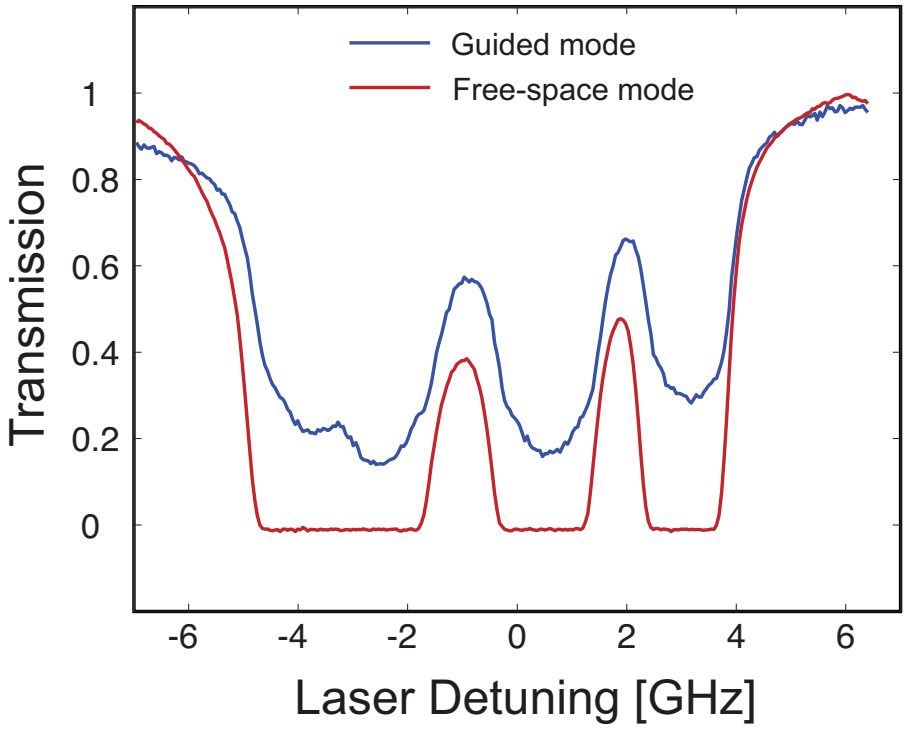

Figure 4.3: **Waveguide transmission:** Transmission spectrum of the waveguide showing evanescent optical interaction with Rb.

tical depths. We have also excited ring resonators that are coupled to these waveguides. The effective interaction length and the intensity of light would increase by the factor of the finesse the resonators and this would allow for demonstrating nonlinear optics at very low powers in this on-chip.

One problem that we have encountered thus far with this system is that Rb very strongly interacts chemically with the waveguides. This leads to extremely high increase of losses in the waveguides. The transmission through the waveguides is seen to progressively deteriorate over a period of several days until the waveguides completely degrade. We are currently working to figure out this issue and build a more sustainable system.

4.4 Summary

In summary, we realized a compact system for evanescent coupling between Rb vapor and light guided in sub-micron silicon nitride nanowires. Spectroscopy of the vapor from the guided mode exhibits broadened resonances which are consistent with the transit-time and Van der Waals effects expected from such a system. Such a system leverages the recently developed photonic capabilities to greatly expand the potential interactions of atoms with light.

CHAPTER 5

OPTICAL ISOLATION VIA BRAGG SCATTERING FOUR WAVE MIXING

5.1 Introduction

This chapter focuses on the utilization of nanophotonic structures for optical isolation via Bragg scattering four wave-mixing. Optical isolators are critical components of photonic infrastructure that allow light to travel only in one direction while blocking light reflected from or scattered by interactions in other parts downstream in the system. The thrust towards miniaturization of photonic devices has necessitated the integration of chip-scale, cost-effective optical isolators into existing photonics platforms, which is challenging since the time-reversal symmetry of light must be broken while maintaining material compatibility with existing platforms. The conventional route to optical isolation utilizes the magneto-optic effect using Faraday rotation in bulk materials. While there has been a recent demonstration of an on-chip magneto-optic device [153], there continues to be a push towards creating other types of optical devices that can be easily integrated with the existing complimentary metal-oxide semiconductor (CMOS) platform [154]. Recently, researchers have demonstrated (both theoretically and experimentally) chip-scale optical isolators using indirect interband photonic transitions[155], the opto-acoustic effect[156], stimulated Brillouin-scattering[157], optomechanical cavities [158, 159], and ring resonators [160]. To date, most studies have focused on demonstrating a large isolation ratio (i.e., ratio of the powers of the attenuated and unattenuated signal waves) along with material compatibility. Although broadband optical isolation has been recently demonstrated in a bulk material platform [161], the reported

bandwidths in chip-scale device platforms are typically a few GHz with the best reported being 200 GHz [158].

5.2 Experiment and discussion

We report the first demonstration of broadband silicon-chip optical isolation of a beam by using Bragg scattering four-wave mixing (BS-FWM). Isolation is achieved over a bandwidth of 8 nm (1 THz), and the measured isolation ratio is 9-dB. In principle, this device can be dispersion engineered to offer greater than 20 dB isolation over 30 nm limited by the pump tuning range and amplifier bandwidth, and competing processes such as modulation instability.

The BS-FWM process involves two pump beams detuned in frequency by $\Delta\omega$ that interfere with a weak signal leading to the generation of an idler detuned by $\Delta\omega$ from the signal [162, 163]. The Bragg scattering process can occur over a widebandwidth range [162, 165, 166] and can translate frequencies without adding noise [164]. The signal and idler field amplitudes evolve along the propagation direction z according to the equations,

$$A_s(z) = A_{s,0}\left[\cos(gz) - \frac{i\kappa}{2g}\sin(gz)\right], \tag{5.1a}$$

$$A_i(z) = A_{s,0}\frac{2i\gamma A_{P1,0}A^*_{P2,0}}{g}\sin(gz), \tag{5.1b}$$

where $g^2 = (\kappa/2)^2 + (\gamma P_0)^2$, $\kappa = \Delta\beta + \gamma(P_1 - P_2)$ is the phase mismatch parameter, A_s, A_i, A_{P1} and, A_{P2} are the amplitudes of the signal, idler, and pump 1 and 2, respectively, $\Delta\beta = \beta_{P_1} + \beta_s - \beta_{P_2} - \beta_i$ is the phase mismatch, and $\gamma = 2\pi n_2/\lambda A_{eff}$ is the effective nonlinear coefficient. The motivation for employing BS-FWM for optical isolation is that, unlike other FWM interactions, the signal can completely

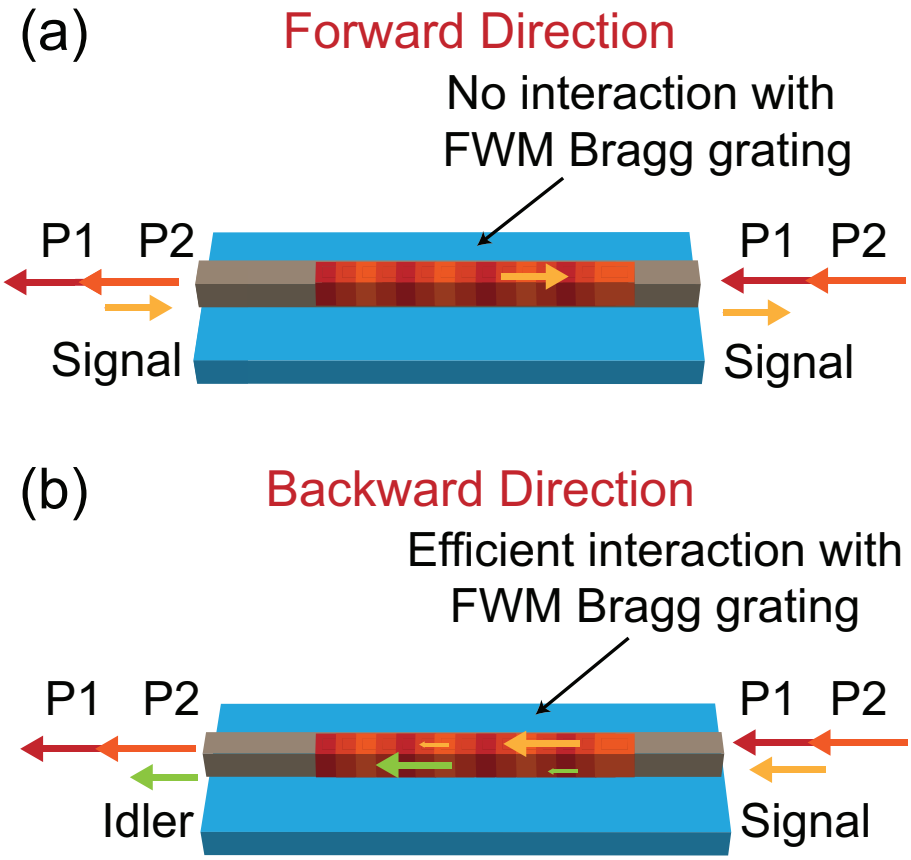

Figure 5.1: **Schematic for optical isolation via Bragg scattering four-wave mixing (BS-FWM) in a silicon-on-insulator platform:** In the BS-FWM process, the two pumps form a grating from which the signal can scatter off depending on its propagation direction. (a) When the signal is counter-propagating with respect to the pump waves (P1 and P2), the BS-FWM process is not phase matched, and the signal passes unattenuated. (b) When the signal co-propagates with the two pumps, the phase matching condition is satisfied and the signal is extinguished generating an idler. With appropriate filters, the two pumps and the generated idler can be removed for the system to work as an isolator.

exchange energy with the idler and consequently be extinguished as the idler is generated. Efficient BS-FWM occurs only when the phase matching $\kappa = 0$ and the energy conservation conditions are satisfied ($\omega_{P_1} - \omega_s = 2\omega_c$, $\omega_{P_2} - \omega_i = 2\omega_c$) where $\omega_{P_1}, \omega_{P_2}, \omega_s$, and ω_i correspond to the frequencies of pump 1, pump 2,

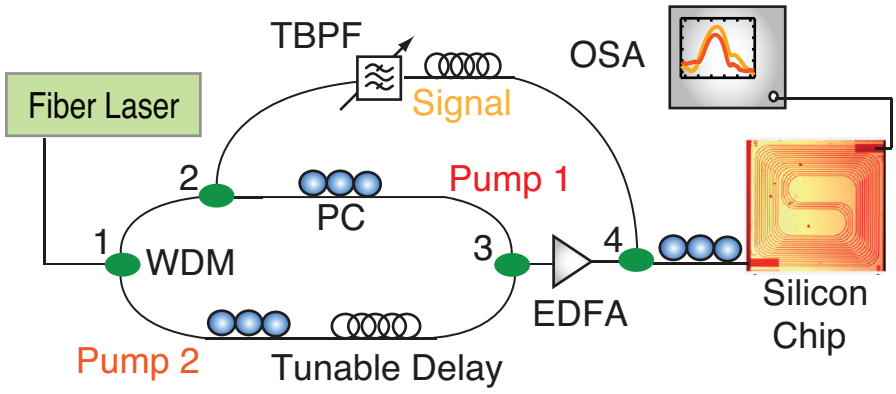

Figure 5.2: **Schematic of the experimental setup:** WDM-wavelength division multiplexer, PC-polarization controller, EDFA-erbium doped fiber amplifer, TBPF-tunable bandpass filter, OSA-optical spectrum analyzer.

signal, and idler, respectively, and the center frequency ω_c coincides with the zero group-velocity dispersion (GVD) point. Maximum conversion efficiency occurs for $gL = \pi/2$ where L is the effective path length. For a silicon waveguide with height of 300 nm and width of 720 nm, $L = 1$ cm, $\gamma = 75$ W^{-1}m^{-1} assuming $n_2 = 4\times10^{-18}$ m^2/W, the power required for 100 % conversion is 2.3 W assuming a propagation loss of 1 dB/cm. The power requirement for efficient optical isolation can be further reduced to a few hundred mW by increasing the effective path length using longer waveguides ($\sim$ 10 cm). Through proper dispersion engineering of Si waveguides, the fabrication of dynamically controlled on-chip tunable and wide bandwidth optical isolators is possible.

Figure 5.1(a-b) shows the schematic for optical isolation via BS-FWM in a Si nanowaveguide. In this scheme, the two pump waves form a Bragg grating from which the signal wave can scatter depending on the direction in which it travels. When the pump and the signal waves are counter-propagating, as shown in Fig. 1 (a), the BS-FWM is not phase matched and no frequency conversion occurs, thereby allowing the signal to pass through the device un-

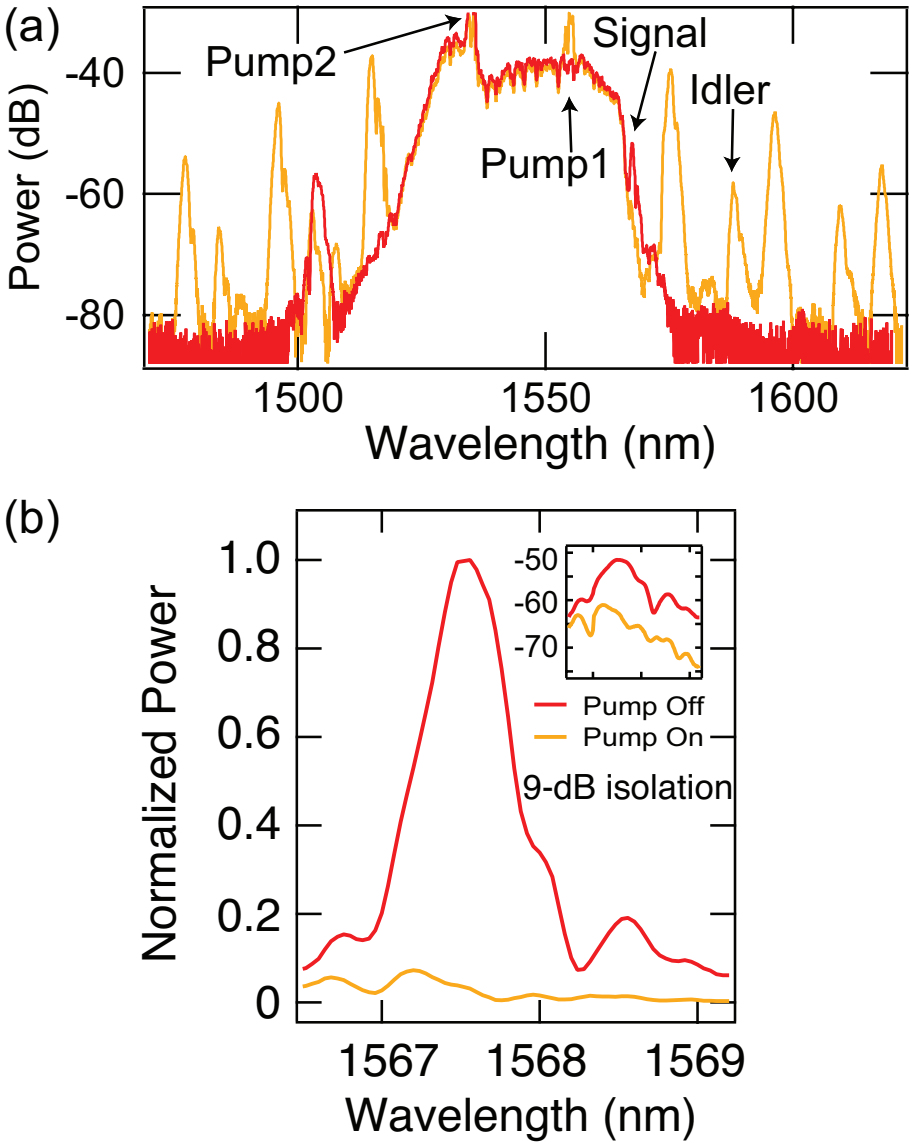

Figure 5.3: **Optical spectrum of Bragg scattering in a Si waveguide:** (a) Measured optical spectra showing Bragg scattering in a Si nanowaveguide with 720-nm width and 300-nm height with pump waves centered at 1555.7 nm and 1535.5 nm and signal at 1567.5 nm. The idler is generated at 1587.9 nm. (b) Optical spectra of the signal (for which the background from the SPM of the two pumps has been removed along with the ASE of the EDFA) showing 9 dB isolation ratio.

attenuated. In contrast, when the two pump waves and the signal co-propagate in the Si-waveguide Fig. 1 (b), efficient phase-matching ensures energy transfer of the signal to an idler, which under ideal conditions (i.e. $gL = \pi/2$) results in complete extinction of the signal, and the bandwidth of the device is determined by the phase matching conditions. The pump and idler can be removed using a fixed bandpass filter. This scheme is analogous to the optical isolation techniques utilizing indirect interband photonic transitions[155], opto-acoustic effect[156] and stimulated Brillouin-scattering[157] since all these schemes also exploit the interaction of the signal wave with a dynamically created refractive index profile to create non-reciprocity in the waveguide. However, the BS-FWM interaction can operate over an inherently much broader bandwidth than via any of these other mechanisms. We experimentally realize a BS-FWM isolator using a silicon-on-insulator (SOI) nanowaveguide with a 720-nm width and 300-nm height and a 30-nm Si slab surrounding it. The nanowaveguide has a zero-GVD point near 1565 nm. The insertion loss per facet is ~7 dB. Suitable design of the nanotaper coupling region can reduce this loss below 1 dB [167]. Figure 5.2 shows an illustration of the experimental setup. We spectrally filter out three separate sections from a broadband modelocked fiber laser operating at 38-MHz. The two pump waves are generated by using 0.5-nm bandpass filters centered at 1535.5 nm and 1555.75 nm. The signal is produced from the fiber laser using a separate tunable 1-nm bandpass filter as shown in Fig. 5.2. The filtered regions of the fiber laser spectrum yield 3.5-ps signal pulses and 7-ps pump pulses. The pump pulses are then amplified and temporally overlapped with each other and the signal in the Si nanowaveguide.

In the forward direction, the signal travels unattenuated as BS-FWM does not occur due to lack of phase matching. In addition, any potential generation

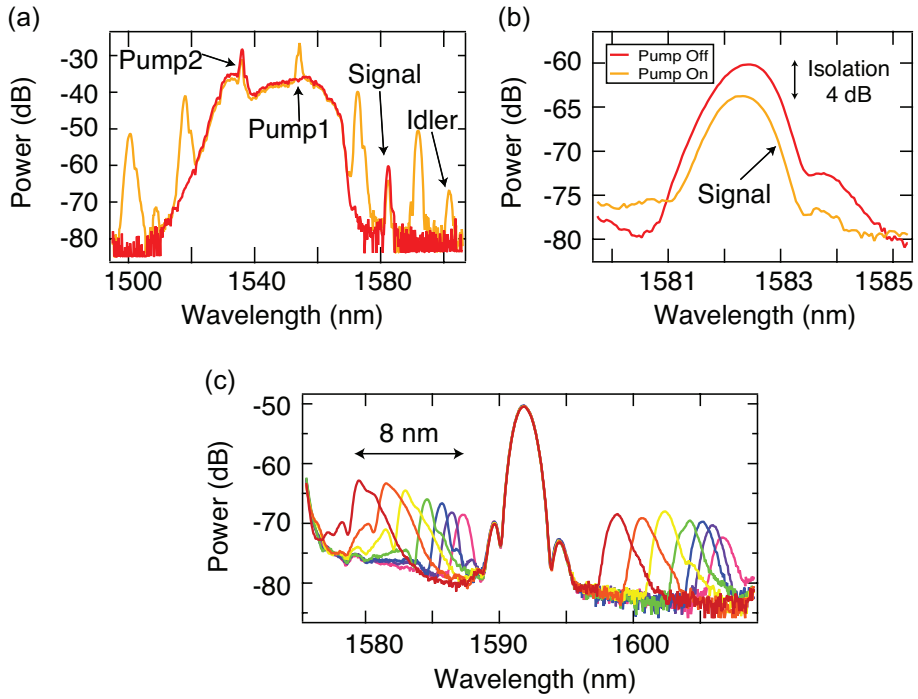

Figure 5.4: **Tuning:** (a) Measured optical spectra showing Bragg scattering in a Si nanowaveguide with pump waves centered at 1554.1 nm and 1536 nm and the signal at 1582.3 nm. The idler is generated at 1601.7 nm. The red curve is the spectra in the absence of pump 1 whereas the orange curve corresponds to the case of both pump waves. (b) Optical spectra of the signal showing a 4 dB isolation ratio. (c) As the signal is tuned, the idler is simultaneous tuned while maintaining the isolation ratio. The isolation bandwidth is 8 nm corresponding to ~1 THz.

of an idler is decreased due to the reduced temporal overlap between the signal and pump waves in the counter-propagating geometry. In the backward direction, the signal would also pass unaltered in the absence of BS-FWM if only one pump is present in a co-propagating geometry. Assuming similar insertion losses at both facets, the difference in signal power in the presence or absence of a pump pulse quantifies the isolation ratio. Figure 5.3(a) shows the full spectrum along with the generated idler in the presence and absence of a pump (orange and red, respectively). We observe cascaded FWM between the two strong

pump fields as well as spectral broadening due to self-phase modulation (SPM) of each pump. Figure 5.3(b) shows the zoomed-in spectrum of the signal in the presence and absence of BS-FWM, which was obtained after subtracting out the background from the SPM and the amplified spontaneous emission (ASE) from the EDFA. We measure an isolation ratio >9 dB. With suitable optical filters, the cascaded FWM peaks and the generated idler can be removed for the device to work as an isolator as shown in Fig. 5.1(a-b). The peak power of the combined pump waves is estimated to be 1.8 W inside the waveguide. As mentioned earlier, higher pump power is required for 100 % conversion efficiency. The presence of SPM and ASE noise at higher pump powers limits the experimental demonstration of maximal optical isolation in the present system. The experimental setup was modified to determine the bandwidth of isolation. We shifted pump 1 to a lower wavelength (1554.1 nm), and the signal was tuned to 1582.3 nm to reduce the background due to SPM and the ASE from the EDFA. We use 1-nm bandpass filters to create the pump waves from the fiber laser. Figure 5.4(a) shows the complete spectrum due to cascaded FWM and the generated idler in the presence and absence of a pump (orange and red, respectively). The zoomed-in spectrum of the signal in the presence and absence of the pump is shown in Fig. 5.4(b). Figure 5.4(c) shows the spectrum of the signal and the idler as the signal is tuned. The signal can be tuned by 8 nm (i.e. ~1 THz) while maintaining the extinction ratio. Although the demonstrated isolation ratio is lower in comparison to other chip-scale isolators [153, 156, 157], the isolation bandwidth is an order of magnitude larger than previously demonstrated.

Finally, we test the true forward and backward isolation of this isolator. Figure **??**(a-b) shows the experimental setup to measure the forward and backward propagation of the signal through the isolator. In the forward direction for isola-

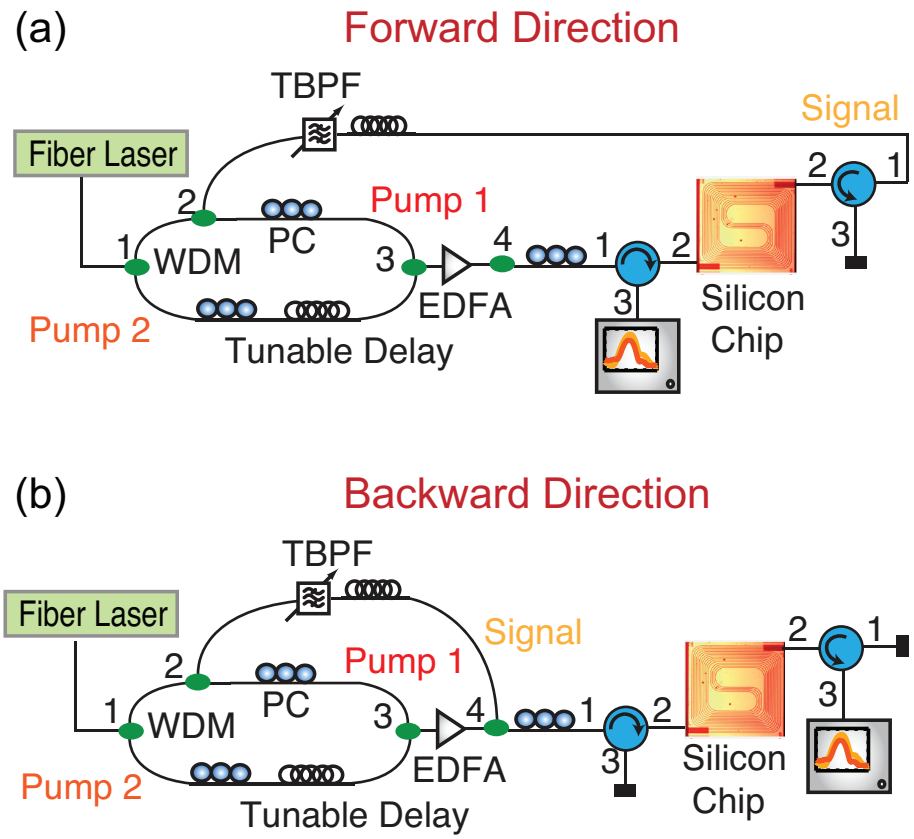

Figure 5.5: **Experimental setup:** Schematic of the experimental setup for measuring the forward and backward direction of the isolator simultaneously. (a) Forward direction for isolator: The pump and the signal travel counter-propagating to each other. A circulator on either side was added to the setup to simultaneously couple the signal and pumps from each side of the silicon chip. The signal is sent through port 2 via port 1 of the circulator on the right side of the chip. It is measured on port 3 of the circulator on the left side of the chip. (b) Backward direction for isolator: The pump and the signal travel co-propagating to each other. The signal and pumps were temporally overlapped and sent into the chip through port 2 via port 1 on the left side of the chip. The output was measured on port 3 of the circulator on the right side of the chip.

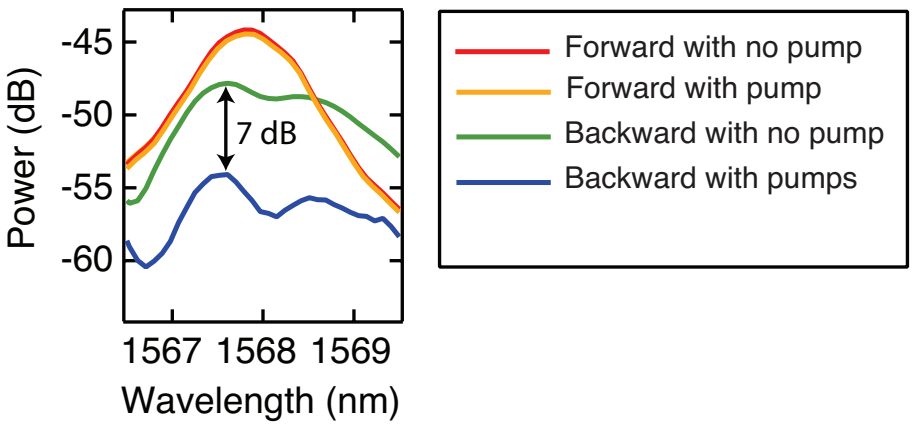

Figure 5.6: **BS-FWM based isolator:** Measured optical spectrum of the signal travelling in the forward and backward through the BS-FWM-based isolator. In the forward direction, the transmission of the signal through the waveguide is shown in red in the absence of pumps. In the presence of counter-propagating pumps, the signal(shown in yellow) travels unattenuated, while in the backward direction the signal (shown in blue) gets converted to an idler via BS-FWM, hence is extinguished by ~7 dB. The signal shown in green is measured when the pumps are turned off in co-propagating scheme such that no BS-FWM can occur. The difference of ~3 dB between the signals shown in green and red is due to the difference in coupling loss on either side of the chip.

tor (shown in fig. 5.5(a)), the pump and the signal travel counter-propagating to each other. A circulator was added on either side of the chip to simultaneously couple the signal and pumps in a counter-propagating fashion. The signal is sent into the chip through port 2 via port 1 of the circulator on the right side of the chip. It is measured on port 3 of the circulator on the left side of the chip. Figure 5.5(b) shows the backward propagation of the signal through the isolator. The pump and the signal travel co-propagating to each other. The signal and pumps were temporally overlapped and sent into the chip through port 2 via port 1 on the left side of the chip. The output was measured on port 3 of the circulator on the right side of the chip. The measured optical spectrum of

the signal travelling in the forward and backward through the BS-FWM-based isolator is shown in fig. 5.6. In the forward direction, the transmission of the signal through the waveguide is shown in red in the absence of pumps. In the presence of the pumps travelling counter-propagating, the signal (shown in yellow) travels unattenuated, while in the backward direction the signal (shown in blue) gets converted to an idler via BS-FWM, hence is extinguished by ~7 dB. The signal shown in green is measured when the pumps are turned off in co-propagating scheme such that no BS-FWM can occur. The difference of ~3 dB between the signals shown in green and red is due to the difference in coupling loss on either side of the chip. Thus, these results constitute a proof of principle demonstration for optical isolation via Bragg-scattering for scalable and integrated nanophotonics and prove that with lower insertion losses and better dispersion engineering of the nanowaveguides, efficient dynamic on-chip optical isolation is a realistic goal.

5.3 Conclusion

In conclusion, we demonstrate optical isolation via Bragg-scattering FWM in a Si-nanowaveguide. We observe 4-dB isolation with an isolation bandwidth of 8-nm. The maximum isolation ratio observed was 9 dB. These results offer a promising approach towards creating a dynamically controlled, broadband chip-scale optical isolators for nanophotonic platforms.

CHAPTER 6

SUMMARY AND FUTURE DIRECTIONS

6.1 Summary

The work in this thesis has focused on demonstrating nonlinear optics in two starkly different class of material systems, namely photonic bandgap fibers and silicon nitride microresonators. Leveraging the technology developed in the past, a plethora of experiments have been explored in the Rb-PBGF system, demonstrating nonlinear optics at the few photon level [69, 86, 88]. This system enables us to explore a wide space of atomic densities and optical intensities in a controlled manner and promises integration with fiber-optic communication networks. These experimental results show the potential of a Rb-PBGF system for exploring quantum nonlinear effects at ultralow powers such as single-photon all optical switching, generation and measurement of nonclassical states of light, and accessing higher-order nonlinear susceptibilities. On the other hand, the silicon nitride microresonator platform allows for exploring extreme nonlinear optics on chip scale. The work in this thesis has focused on utilizing this CMOS compatible material medium for generating ultrawide bandwidth frequency combs and characterizing the spectral and temporal properties thereof. While the microresonator based frequency comb technology has progressed by leaps and bounds in the past couple of years, there is vast unexplored territory that needs to be experimentally verified and accomplished before it can be directly applied to spectroscopy, astronomical applications and precision metrology. Nevertheless the set of experiments discussed in this thesis has shown promise for the microresonator based frequency combs

to become a robust and chip-scale device and has advanced the state-of-the-art towards making future applications a reality [112, 118, 119, 120]. Additionally, a route towards potentially integrating Rb with microresonators has been discussed and demonstrated [147]. The following sections shed light on some of the possible future experiments that can be carried out in either systems and in a more integrated Rb-chip platform.

6.2 Experiments related to photonic bandgap fiber

Currently, the experiments in Rb-PBGF system show that only the first few mm of the fiber contributes towards desorption. Direct measurement is necessary to confirm this observation and monitor the longitudinal distribution of adsorbed Rb atoms. Desorption currently occurs due to the interaction of the wings of the Gaussian light mode with the adsorbed atoms. Instead if the entire beam can illuminate the fiber walls, significantly lower optical powers will be required. This indicates that desorbing the fiber with a Lagguere beam might be helpful. The next logical steps would involve investigating techniques for pushing the atoms further down the length of the fiber to further enhance the interaction length.

As discussed in this thesis, the Rb-PBGF system allows for demonstration of few-photon nonlinear optics. The ultimate limit is single-photon nonlinear optics - the limit where individual photons strongly interact with each other. Realization of such nonlinear processes would not only facilitate peak performance of classical nonlinear devices, but also create a unique resource for implementation of quantum networks and other applications that rely on the generation

and manipulation of non-classical light. Building a cavity around the current Rb-PBGF system with a finesse ~20 should be enough to improve the intensity and cross-phase modulation via TPA such that it may be measurable at the single-photon level since the effective interaction length and in the intensity of light would increase by the factor of the finesse.

A new direction being pursued in the Rb-PGBF system is coherent photon conversion (CPC). This scheme has been recently proposed for realizing efficient quantum computing [148]. CPC combines a third-order nonlinearity $\chi^{(3)}$ with an intense coherent field (pump) leading to a large effective second-order nonlinearity $\chi^{(2)}_{eff}$. Using this large engineered $\chi^{(2)}_{eff}$, photons can be coherently converted from one mode into two new modes. This directly translates to new effective ways of generating and processing states for photonic quantum computing. The extremely high nonlinearity of the Rb-PBGF systems allows for exploring yet another new direction, namely Bragg-scattering four-wave mixing, wherein two non-degenerate pump photons interact with a weak signal photon to create an idler photon [149]. In this wavelength exchange process, the total power in the signal and idler beams is conserved, vacuum fluctuations are not amplified and quantum states of single-photons can noiselessly be translated from one frequency mode to another.

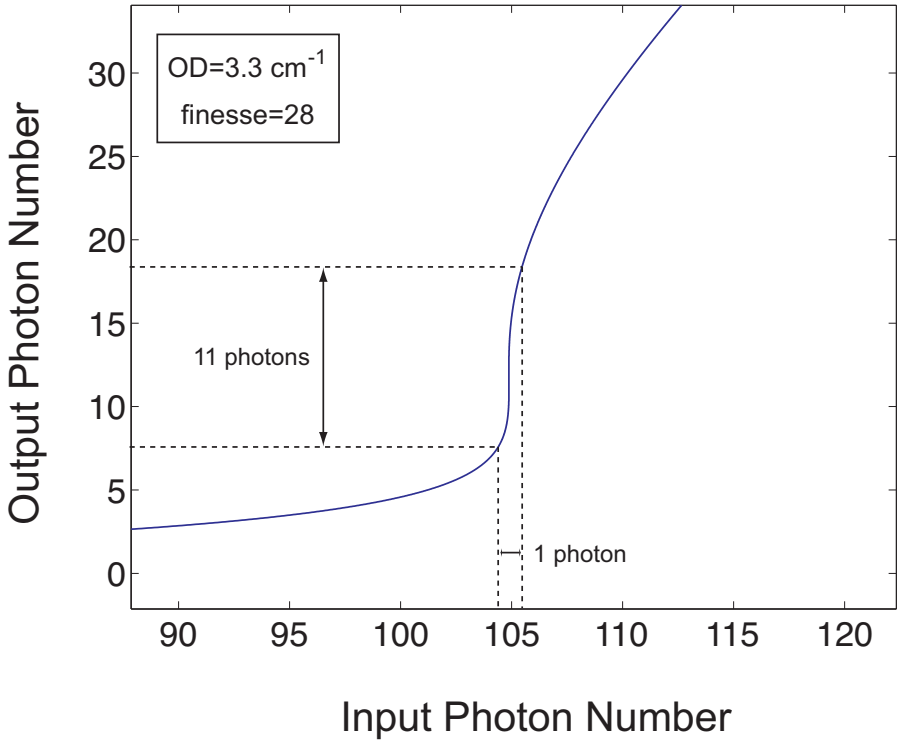

Figure 6.1: **Optical switching using silicon nitride microresonator:** Illustration of bistable behavior for an s-shaped intensity response function.

6.3 Experiments related to silicon nitride platform

6.3.1 Integrated Rb-SiN platform

The interactions observed between Rubidium vapor and the guided light mode in a silicon nitride waveguide could be exploited by optimizing these structures for all-optical switching. Specifically, this entails optimizing the geometry of the ring resonators in order to switch a bright, many-photon laser field with a weak control beam containing as little as one photon. One of the disadvantages of using tapered fibers or fabricated ring resonator structures is that hot atoms enter and leave the spatial evanescent field at a fast rate, giving rise to very

large transit-time decoherence. The typical switching procedure is illustrated using the bistability curve in Figure 6.1. Initially the switch is in the off position. The resonator absorbs light with a photon number below the critical threshold value, and the resultant intra-cavity field does not build up power in the cavity nor couple out of it. A small number of photons could then be added, for example via a weak control pulse. This will cause the input field to exceed the input intensity threshold, thus coupling the signal beam to a drop port. Once the pulse has transmitted, the remaining intensity build-up is sufficient to self-sustain the on position. The switch can then be turned off in a deterministic manner by removing the same small number of photons in a pulsed fashion. The system then remains in the off-state until the procedure is repeated. Assembling a cold-atom cloud near the ring resonator to reduce the decoherence could lead to a silicon-compatible on-chip device for performing low-light-level nonlinear interactions. Additionally, designing and fabricating suspended structures in silicon nitride would increase the interaction between the Rb atoms and the resonator.

6.3.2 Microresonator based frequency combs

Stabilization and phase noise characterization

Microresonator-based frequency comb generation has been an area of intense research in the past few years, particularly because of its potential as a platform for the realization of compact, integrated stabilized comb sources. However, unlike frequency comb generation via supercontinuum using femtosecond lasers, microresonator-based frequency comb generation is not a ma-

ture technology and requires extensive theoretical and experimental studies in order to understand the dynamics and the underlying physics that determine the properties of the comb such as the overall bandwidth of the comb and linewidth of individual comb lines.

One of the major factors that limits the stability of microresonator-based combs is the frequency jitter of the pump laser due to mechanical perturbations. This instability can be removed through active stabilization of the laser frequency by locking it to a stable frequency reference via a RF feedback loop. This will enable probing the intrinsic stability dynamics of microresonator-based frequency combs and generation of optical combs with comb linewidth on the order of the pump laser linewidth. Additionally, the pump power fluctuations lead to significant thermal fluctuations in the chip. This effect causes the resonance wavelength to shift due to change in refractive index, thereby making the microresonator-based combs significantly unstable. Therefore, active stabilization of the laser power in addition to wavelength is required with the help of a laser noise eater.

The next step would then be to characterize the phase noise properties of frequency combs. Low phase noise is characteristic of an oscillator with minimal random and rapid fluctuations in the frequency domain and low jitter in the time domain. Therefore, the ability to generate optical frequency combs with low phase noise will allow for the generation of waveforms of the purest quality in the optical and temporal domain. Further, since the optical frequency comb forms a direct link between the optical and microwave domain, and the phase noise of the microwave signal is inversely proportional to the square of the optical-to-microwave-frequency division ratio, this allows for generation of ex-

tremely stable microwave signals as well. Therefore, low-phase-noise frequency combs are relevant for a number of scientific and signal processing applications such as high speed analog-to digital conversion, remote synchronization, local oscillators for fountain clocks, coherent control over quantum mechanical processes, and photonically enabled generation and processing of ultra-broadband radio frequency (RF) electrical signals.

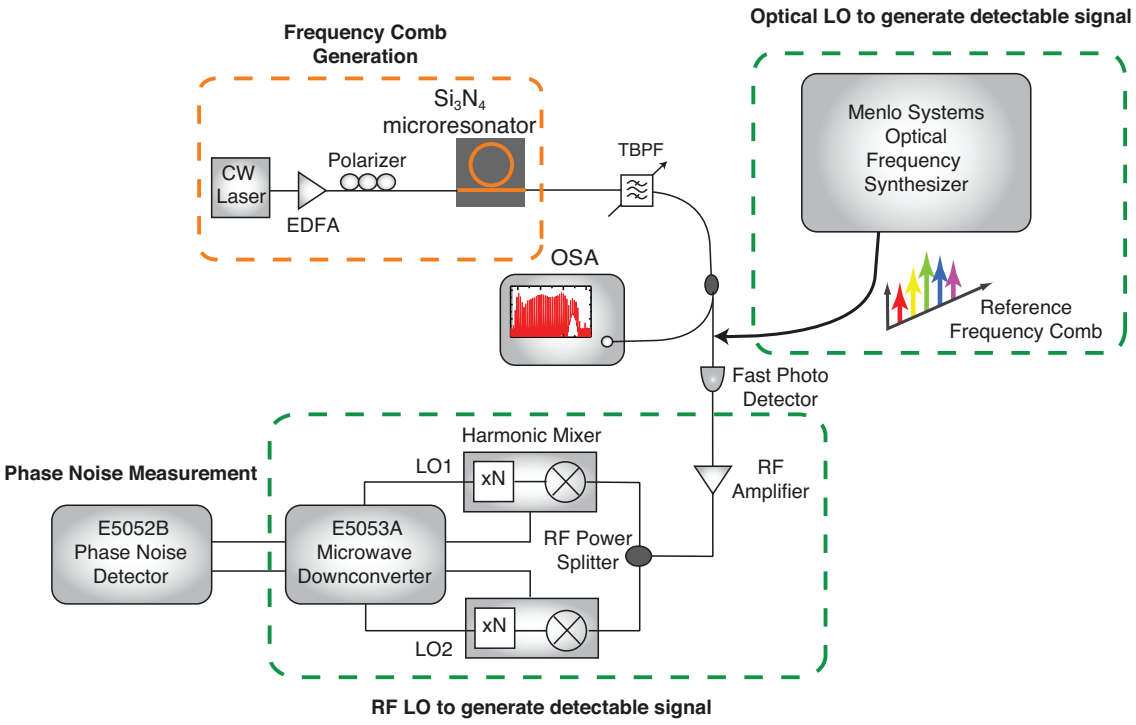

Figure 6.2: **Phase noise measurement:** Schematic of experimental setup for measurement of phase noise.

Although the generation of mode-locked pulses is an indicator of phase coherence and spectral purity of the frequency comb lines, phase noise characterization provides the necessary piece of information to estimate the overall frequency stability and timing jitter of the frequency comb. Characterizing the comb with respect to both a stabilized electrical and optical reference will also provide quantitative evidence for whether such optical frequency combs can

improve upon existing technology for applications in metrology, signal processing, and spectroscopy.

Figure 6.2 shows the experimental setup for phase noise characterization using a stabilized RF reference. A single-frequency cw pump is amplified and used to generate a comb in a silicon-nitride microresonator. A section of the comb is then filtered using a tunable bandpass filter, and the RF beatnote is detected using a fast photodetector. The resulting electrical signal corresponds to the FSR of the comb. Depending on the frequency of the beatnote and the phase-noise detection bandwidth of the phase-noise detector, the electrical signal is then amplified and either routed directly or down converted using harmonic mixers and then sent to the phase noise detector. This key measurement will allow for characterizing the stability and phase noise of the microwave signal generated from the microresonator-based frequency comb derived from the comb line spacing. Further, to understand the overall dynamics and fundamental physics and the short and long term stability of frequency combs, it is not only essential to measure the phase noise from the RF tone generated by beating two adjacent comb lines but also to characterize the absolute stability of individual comb lines. For this measurement, the filtered comb lines are interfered with an ultra stable external reference frequency comb generated using the Menlo systems optical frequency stabilizer. The beatnote is detected, filtered, and routed directly to the phase-noise detector.

This thesis shows the first demonstration of an octave spanning frequency comb pumped at 1550 nm. However, due to the very small power in the comb lines at the edges and possibly incoherent lines, this comb cannot be utilized for self-referencing or *f-2f* locking. This self-referencing technique is not only

critical for the full characterization of the comb's f_{CEO} and f_{rep}, but also for the microresonator-based frequency combs to become a viable technology. This necessitates the generation of frequency combs with bandwidths larger than an octave such that there is sufficient power in the wings. Additionally, although modestly wide-bandwidth combs have been demonstrated pumping at 1 μm as discussed in chapter 3, the microresonator dispersion can be carefully re-engineered to generate ultra-wide bandwidth combs starting from the visible part of the optical spectrum to the near-IR region. This will allow for $f - 2f$ locking with the help of readily available optical components.

Frequency combs applied to astronomical spectroscopy

Astro-combs are optical frequency combs with typical repetition rate of >10 GHz, referenced to atomic clocks and have recently been optimized for wavelength calibration of ground based astrophysical spectrographs [150, 151]. These astro-combs are expected to increase the accuracy and long-term stability of astrophysical spectrographs, with applications including the detection and characterization of extra-solar planets (exoplanets), direct measurement of the acceleration of the universe, and red-shift of galaxies. In particular, searches for Earth-like exoplanets around Sun-like stars using precision stellar radial velocity measurements require <5 cm/s radial velocity accuaracy and long-term stability, which is equivalent to 100 kHz and 50 kHz accuracy of Doppler shift measurement of stellar light at 500 nm and 1 μm, respectively, over several-year observation periods. Currently, these astro-combs are built to have the requisite repetition rate by filtering out comb lines from a densely spaced optical frequency comb generated via supercontinuum. To calibrate the spectrograph

with an accuracy of 100 kHz with an astrocomb, the intensity of the side modes must be suppressed or controlled to $<10^{-4}$ of the astro-comb's peak intensity [151]. Therefore significant effort has to be spent to generate the desired astro-combs. Alternatively, microresonator-based frequency combs can provide an easy route towards generating chip-scale astro-combs with the desired comb spacing.

Others

There is a growing demand for visible and mid-infrared frequency combs that find direct application in precision spectroscopy of molecules [152]. Material platforms such as silicon and silicon carbide can be explored to develop such frequency combs. These platforms might provide intriguing prospects for molecular spectroscopy and gas trace sensing on a chip-scale. Additionally, extension of precision spectroscopy in the extreme ultraviolet regions may be envisioned. As sources of phase-stabilized femtosecond pulses, microresonator-based frequency combs might provide an easier route towards production of high repetition rate attosecond pulses along with intense few-cycle long-wavelength laser systems.

Ultimately, one can build upon the work in presented in this thesis to explore development of numerous exciting technologies based on the material platforms discussed and find solutions to multiple fundamental physical problems.

APPENDIX A

GROUP VELOCITY DISPERSION

Throughout chapter 3, dispersion engineering has been crucial for the generation of optical frequency combs in silicon nitride microresonators. This appendix provides a simple description of the concept of dispersion.

When an electromagnetic wave interacts with the bound electrons of a dielectric, the medium response, in general, depends on the optical frequency ω. This property, referred to as chromatic dispersion, manifests through the frequency dependence of the refractive index $n(\omega)$. Chromatic dispersion is related to the characteristic resonance frequencies at which the medium absorbs the electromagnetic radiation through oscillations of bound electrons. Far from the medium resonances, the refractive index is well approximated by the Sellmeier equation [4],

$$n^2(\omega) = 1 + \sum_{j=1}^{m} \frac{B_j \omega_j^2}{\omega_j^2 - \omega^2}, \tag{A.1}$$

where ω_j is the resonance frequency and B_j is the strength of j^{th} resonance.

Thus the light travels with a speed slower than c by a factor of the index of refraction of the medium, or the speed is $v = c/n(\omega)$. The phase velocity of the plane wave is defined as the speed at which the phase of a single frequency component travels. The phase velocity defined in terms of the angular frequency and wavevector is given by:

$$v_p = \frac{\omega}{k}, \tag{A.2}$$

where $k = 2\pi/\lambda$. In a waveguide the light is confined and propagates in a specific direction defined by the waveguide geometry. In this case, the phase velocity is

defined as,

$$v_p = \frac{\omega}{\beta} \tag{A.3}$$

where the wavevector is substituted by the mode-propagation constant β. This mode-propagation constant can be expanded in a Taylor series about a central frequency ω_0 as

$$\beta(\omega) = n(\omega)\frac{\omega}{c} = \beta_0 + \beta_1(\omega - \omega_0) + \frac{1}{2}\beta_2(\omega - \omega_0)^2 + ..., \tag{A.4}$$

where

$$\beta_m = \left(\frac{d^m\beta}{d\omega}\right)_{\omega=\omega_0} (m = 0, 1, 2, ..). \tag{A.5}$$

Thus the phase velocity must also change for different wavelengths. If we consider an optical pulse composed of multiple frequencies, we can define the group velocity v_g as the speed at which the envelope travels:

$$v_p = \frac{d\beta}{d\omega}. \tag{A.6}$$

Thus, β_1 and β_2 can be written as

$$\beta_1 = \frac{1}{v_g} = \frac{n_g}{c} = \frac{1}{c}\left(n + \omega\frac{dn}{d\omega}\right), \tag{A.7a}$$

$$\beta_2 = \frac{1}{c}\left(2\frac{dn}{d\omega} + \omega\frac{d^2n}{d\omega^2}\right). \tag{A.7b}$$

where n_g is the group index and β_2 is known as the group-velocity dispersion parameter. Physically, the group velocity is the speed at which information is carried. In a waveguide,n_{eff} is effective index that changes with wavelength. β_1 is also related to the parameter D called the dispersion parameter as

$$D = \frac{d\beta_1}{d\lambda} = -\frac{2\pi c}{\lambda^2}\beta_2 = -\frac{\lambda}{c}\frac{d^2n}{d\lambda^2}. \tag{A.8}$$

Due to the phase-matching requirements for many of the nonlinear processes involving waves at non-degenerate frequencies, these parameters become very

important for a waveguide. n_g and D are very sensitive to waveguide geometry and this is the property that is exploited to engineer the dispersion for generating broadband frequency combs.

BIBLIOGRAPHY

[1] P. A. Fraken, A. E. Hill, C. W. Peters, and G. Weinreich, Phys. Rev. Lett. **7**, 118 (1961).

[2] J. F. Young, G. C. Bjorklund, A. H. Kung, R. B.Miles, and S. E. Harris, Phys. Rev. Lett. **27**, 1551 (1971).

[3] T. Miya, Terunuma, T. Hosaka, and T. Miyashita, Electron. Lett. **15**, 106 (1979).

[4] Govind P. Agrawal, *Nonlinear Fiber Optics*, Academic Press, New York, 3rd edition, 2001.

[5] R. H. Stolen and C. Lin, Phys. Rev. A **17**, 1448 (1978).

[6] M. N. Islam, L. F. Mollenauer, R. H. Stolen, J. R. Simpson, and H.-T. Shang, Opt. Lett. **12**, 625 (1987).

[7] E. P. Ippen and R. H. Stolen, Appl. Phys. Lett. p. 539 (1972).

[8] R. H. Stolen and E. P. Ippen, Appl. Phys. Lett. p. 276 (1973).

[9] R. Stolen and J. Bjorkholm, IEEE Journal of Quantum Electronics **18**, 1062 (1982).

[10] A. R. Bhagwat and A. L. Gaeta, Opt. Express **16**, 5035 (2008).

[11] D. G. Ouzounov, F. R. Ahmad, D. Muller, N. Venkataraman, M. T. Gallagher, M. G. Thomas, J. Silcox, K. W. Koch, and A. L. Gaeta, Science **301**, 1702 (2008).

[12] F. Benabid, J. C. Knight, G. Antonopoulos, and P. S. J. Russell, Science **298**, 399 (2002).

[13] S. Ghosh, J. E. Sharping, D. G. Ouzounov, and A. L. Gaeta, Phys. Rev. Lett. **94**, 093902 (2005).

[14] F. Couny, F. Benabid, P. J. Roberts, P. S. Light, and M. G. Raymer, Science **318**, 1118 (2007).

[15] F. Benabid, P. S. Light, F. Couny, and P. S. J. Russell, Opt. Express 13, 5694 (2005).

[16] P. Yeh and A. Yariv, Opt. Commun. **19**, 427 (1976).

[17] R. F. Cregan, B. J. Mangan, J. C. Knight, T. A. Birks, P. S. J. Russell, P. J. Roberts, and D. C. Allan, Science **285**, 1537 (1999).

[18] C. J. Hensley, D. G. Ouzounov, A. L. Gaeta, N. Venkataraman, M. T. Gallagher, and K. W. Koch, Opt. Express **15**, 3507 (2007).

[19] A. Cerqueira S Jr, Rep. Prog. Phys. **73** 024401 (2010).

[20] S. E. Harris and Y. Yamamoto, Phys. Rev. Lett. 81, 3611-3614 (1998).

[21] D. A. B. Miller, Nat. Photon. **4**, 3-5 (2010).

[22] D. M. Greenberger, M. A. Horne, A. Shimony, and A. Zeilinger, Am. J. Phys. **58**, 1131-1143 (1990).

[23] E. Knill, R. Laflamme, and G. J. Milburn, Nature **409**, 46-52 (2001).

[24] J. D. Franson, B. C. Jacobs, and T. B. Pittman, Phys. Rev. A **70**, 062302 (2004).

[25] B. C. Jacobs, T. B. Pittman, and J. D. Franson, Phys. Rev. A **74**, 010303 (2006).

[26] B. C. Jacobs and J. D. Franson, Phys. Rev. A **79**, 063830 (2009).

[27] N. Imoto, H. A. Haus, and Y. Yamamoto, Phys. Rev. A **32**, 2287 (1985).

[28] G. J. Milburn, Quantum optical Fredkin gate, Phys. Rev. Lett.**62**, 2124 (1989).

[29] J. H. Shapiro, Phys. Rev. A **73**, 062305 (2006).

[30] W. J. Munro, K. Nemoto, and T. P. Spiller, New J. Phys. **7**, 137 (2005).

[31] D. A. Braje, V. Balic, G. Y. Yin, and S. E. Harris, Phys. Rev. A **68**, 041801 (2003).

[32] H. Schmidt and A. R. Hawkins, Laser Photon. Rev. **4**, 720-737 (2003).

[33] H. Kang and Y. Zhu, Phys. Rev. Lett. **91**, 093601 (2003).

[34] D. A. Steck, http://steck.us/alkalidata/ (2010).

[35] http://www.nktphotonics.com/files/files/Air-6-800-040611.pdf.

[36] C. Koos, P. Vorreau, T. Vallaitis, P. Dumon, W. Bogaerts, R Baets, B Esembeson, I. Biaggio, T. Michinobu, F. Diederich, W. Freude, and J. Leuthold, Nature Photonics **3**, 216219 (2009).

[37] M. A. Foster, A. C. Turner, J. E. Sharping, B. S. Schmidt, M. Lipson, and A. L. Gaeta, Nature **441**, 960 (2006).

[38] R. Salem, M. A. Foster, A. C. Turner, D. F. Geraghty, M. Lipson, and A. L. Gaeta, Nature Photonics **2**, 3538 (2007).

[39] F. Li, M. Pelusi, D-X. Xu, A. Densmore, R. Ma, S. Janz, and D.J. Moss, Optics Express **18**, 3905 (2010).

[40] M. A. Foster, R. Salem, D. F. Geraghty, A. C. Turner-Foster, M. Lipson, and A. L. Gaeta, Nature **456**, 81 (2008).

[41] P. Del'Haye, A. Schliesser, O. Arcizet, T. Wilken, R. Holzwarth, and T. J. Kippenberg, Nature **450**, 12141217 (2007).

[42] I. H. Agha, Y. Okawachi, and A. L. Gaeta, Opt. Express **17**, 1620916215 (2009).

[43] D. Braje, L. Hollberg, and S. Diddams, Phys. Rev. Lett. **102**, 193902 (2009).

[44] A. A. Savchenkov, A. B. Matsko, V. S. Ilchenko, I. Solomatine, D. Seidel, and L. Maleki, Phys. Rev. Lett. **101**, 093902 (2008).

[45] I. S. Grudinin, N. Yu, and L. Maleki, Opt. Lett. **34**, 878880 (2009).

[46] C. Y. Wang, T. Herr, P. Del'Haye, A. Schliesser, J. Hofer, R. Holzwarth, T. W. Hnsch, N. Picqu and T. J. Kippenberg, Nature Communications **4**, 1345 (2012).

[47] J. L. Hall, Nobel Lecture, (2005).

[48] A. Schliesser, N. Picqu and T. W. Hnsch, Nature Photonics **6**, 440449 (2012).

[49] M. A. Foster, J. S. Levy, O. Kuzucu, K. Saha, M. Lipson, and A. L. Gaeta, Optics Express **19**,14233-14239 (2011).

[50] S. Ghosh, A. R. Bhagwat, C. K. Renshaw, S. Goh, A. L. Gaeta, and B. J. Kirby, Phys. Rev. Lett. **97**, 023603 (2006).

[51] W. Yang, D. B. Conkey, B. Wu, D. Yin, A. R. Hawkins, and H. Schmidt, Nat. Photon. **1**, 331 (2007).

[52] V. Venkataraman, P. Londero, A. R. Bhagwat, A. D. Slepkov, and A. L. Gaeta, Opt. Lett. **35**, 2287-2289 (2010).

[53] P. Londero, V. Venkataraman, A. R. Bhagwat, A. D. Slepkov, and A. L. Gaeta, Phys. Rev. Lett. **103**, 043602 (2009).

[54] E. B. Alexandrov, M. V. Balabas, D. Budker, D. English, D. F. Kimball, C. H. Li, and V. V. Yashchuk, Phys. Rev. A **66**, 042903 (2002).

[55] M. J. Renn, D. Montgomery, O. Vdovin, D. Z. Anderson, C. E.Wieman, and E. A. Cornell, Phys. Rev. Lett. **75**, 3253 (1995).

[56] F. K. Gel'mukhanov and A. M. Shalagin, JETP Lett. **29**, 711 (1979).

[57] H. G. C. Werij, J. E. M. Haverkort, and J. P. Woerdman, Phys. Rev. A **33**, 3270 (1986).

[58] A. Gozzini, F. Mango, J. H. Xu, G. Alzetta, F. Maccarrone, and R. A. Bernheim, Nuovo Cimento D **15**, 709 (1993).

[59] S. N. Atutov, V. Biancalana, P. Bicchi, C. Marinelli, E. Mariotti, M. Meucci, A. Nagel, K. A. Nasyrov, S. Rachini, and L. Moi, Phys. Rev. A **60**, 4693 (1999).

[60] A. Burchianti, C. Marinelli, A. Bogi, J. Brewer, K. Rubahn, H.-G. Rubahn, F. della Valle, E. Mariotti, V. Biancalana, S. Veronesi, et al., Europhys. Lett. **67**, 983 (2004).

[61] A. R. Bhagwat, A. D. Slepkov, V. Venkataraman, P. Londero, and A. L. Gaeta, Phys. Rev. A **79**, 063809 (2009).

[62] A. D. Slepkov, A. R. Bhagwat, V. Venkataraman, P. Londero, and A. L.Gaeta, Opt. Express **16**, 18976 (2008).

[63] A. D. Slepkov, A. R. Bhagwat, V. Venkataraman, P. Londero, and A. L. Gaeta, Phys. Rev. A **81**, 053825 (2010).

[64] D. D. Yavuz, Phys. Rev. A **74**, 053804 (2006).

[65] P. Lambropoulos, C. Kikuchi, and R. K. Osborn, Phys. Rev. **144**, 1081(1966).

[66] D. E. Roberts and E. N. Forston, Phys. Rev. Lett. 31, 1539 (1973).

[67] M. D. Levenson and N. Bloembergen, Phys. Rev. Lett. **32**, 645 (1974).

[68] S. M. Hendrickson, M. M. Lai, T.B. Pittman and J.D. Franson, Phys. Rev. Lett. **105**, 173602 (2010).

[69] K. Saha, V. Venkataraman, P. Londero, and A. L. Gaeta, Phys. Rev. A **83**, 033833 (2011).

[70] F. Nez, F. Biraben and R. Felder and Y. Millerioux, Opt. Commun. **102**, 432 (1993).

[71] R. Boyd, *Nonlinear Optics*, 3rd ed. (Elsevier, Oxford, 2008).

[72] W. Demtroder, in Laser Spectroscopy (Springer-Verlag, Berlin, 1982).

[73] K. Shimoda, ed., in High-Resolution Spectroscopy, Vol. 13 (Springer-Verlag, Berlin, 1976).

[74] M. D. Levenson and N. Bloembergen, Phys. Rev. Lett. **32**, 645 (1974).

[75] J. E. Bjorkholm and P. F. Liao, IEEE J. Quantum Electron. **10**, 906 (1974).

[76] F. Biraben, B. Cagnac, and G. Grynberg, Phys. Rev. Lett. **32**, 643 (1974).

[77] S. N. Bagayev, V. P. Chebotayev, and E. A. Titov, Laser Physics **4(2)**, 224-292 (1994).

[78] T. P. Spiller, K. Nemoto, S. L. Braunstein, W. J. Munro, P. van Loock, and G. J. Milburn, New J. Phys. **8**, 30 (2006).

[79] W. J. Munro, K. Nemoto, R. G. Beausoleil, and T. P. Spiller, Phys. Rev. A 71, 033819 (2005).

[80] K. Nemoto and W. J. Munro, Phys. Rev. Lett. **93**, 250502 (2004).

[81] S. D. Barrett, P. Kok, K. Nemoto, R. G. Beausoleil, W. J. Munro, and T. P. Spiller, Phys. Rev. A **71**, 060302(2005).

[82] N. Matsuda, R. Shimizu, Y. Mitsumori, H. Kosaka, and K. Edamatsu, Nat. Photon. **3**, 95-98 (2009).

[83] H. Chang, Y. Du, J. Yao, C. Xie, and H. Wang, Europhys. Lett. **65**, 485(2004).

[84] H.-Y. Lo, P.-C. Su, and Y.-F. Chen, Phys. Rev. A **81**, 053829 (2010).

[85] B.-W. Shiau, M.-C. Wu, C.-C. Lin, and Y.-C. Chen, Phys. Rev. Lett. **106**, 193006 (2011).

[86] V. Venkataraman, K. Saha, P. Londero, and A. L. Gaeta, Phys. Rev. Lett. **107**, 193902 (2011).

[87] A. J. Olson, E. J. Carlson and S. K. Mayer, Am. J. Phys. **74**, 218 (2006).

[88] V. Venkataraman, K. Saha, and A. L. Gaeta, Nature Photon. **7**, 138-141 (2013).

[89] Th. Udem, R. Holzwarth, T. W. Hänsch, Nature **416,** 233 (2002).

[90] R. Holzwarth, Th. Udem, T. W. Hänsch, J. C. Knight, W. Wadsworth, and P. S. Russell, Phy. Rev. Lett., **85**, 2264, (2000).

[91] D. E. Spence, P. N. Kean, and W. Sibbett, Optics Lett., **16**, 4246 (1991).

[92] T. J. Kippenberg, R. Holzwarth, and S. A. Diddams, "Microresonator based optical frequency combs," Science **332**, 555-559 (2011).

[93] I. S. Grudinin, N. Yu, and L. Maleki, "Generation of optical frequency combs with a CaF_2 resonator," Opt. Lett. **45**, 878-880 (2009).

[94] D. Braje, L. Hollberg, and S. Diddams, Phys. Rev. Lett. **102**, 193902 (2009).

[95] L. Razzari, D. Duchesne, M. Ferrera, R. Morandotti, S. Chu, B. E. Little, and D. J. Moss, Nature Photon. **4**, 41-45 (2010).

[96] J. S. Levy, A. Gondarenko, M. A. Foster, A. C. Turner-Foster, A. L. Gaeta, and M. Lipson, Nature Photon. **4**, 37-40 (2010).

[97] H. Lee, T. Chen, J. Li, K. Y. Yang, S. Jeon, O. Painter, and K. J. Vahala, Nature Photon. **6**, 369-373 (2012).

[98] Scott B. Papp, and Scott A. Diddams, Phys. Rev. A **84**, 053833 (2011).

[99] A. Alduino, and M. Paniccia, Nature Photon., **1**, 153-155 (2007)

[100] D. A. B. Miller, IEEE Journal of Selected Topics in Quantum Electronics, **6**, 1312-1317 (2000).

[101] A. Yariv, IEEE Phot. Tech. Lett., **14**, 483-485 (2002).

[102] A. C. Turner, C. Manolatou, B. S. Schmidt, M. Lipson, M. A. Foster, J. E. Sharping, and A. L. Gaeta, Opt. Express **14,** 4357-4362 (2006).

[103] D. T. H. Tan, K. Ikeda, P. C. Sun, and Y. Fainman, Appl. Phys. Lett. **96,** 061101 (2010).

[104] M. R. E. Lamont, Y. Okawachi, and A. L. Gaeta, Opt. Lett. **38**, 3478-3481 (2013).

[105] T. Herr, K. Hartinger, J. Riemensberger, C.Y. Wang, E. Gavartin, R. Holzwarth, M. Gorodetsky, T.J. Kippenberg Nature Photon. **6**, 480-487 (2012).

[106] A. B. Matsko, A. A. Savchenkov, and L. Maleki, Opt. Lett. **37**, 43-45 (2012).

[107] A. B. Matsko, A. A. Savchenkov, W. Liang, V. S. Ilchenko, D. Seidel, and L. Maleki, Opt. Lett. **36**, 2845-2847 (2011).

[108] T. Herr, V. Brasch, J. D. Jost, C. Y. Wang, N. M. Kondratiev, M. L. Gorodetsky, and T. J. Kippenberg, arXiv:1211.0733 (2013).

[109] M. Haelterman, S. Trillo, and S. Wabnitz, Opt. Commun. **91**, 401 (1992).

[110] Y. K. Chembo and N. Yu, Phys. Rev. A 82, 033801 (2010).

[111] S. T. Cundiff and J. Ye, Rev. Mod. Phys. **75,** 325 (2003).

[112] Y. Okawachi, K. Saha, J. S. Levy, Y. H. Wen, M. Lipson, and A. L. Gaeta, Opt. Lett. **36**, 3398-3400 (2011).

[113] S. A. Diddams, D. J. Jones, J. Ye, S. T. Cundiff, J. L. Hall, J. K. Ranka, R. S. Windeler, R. Holzwarth, Th. Udem, and T. W. Hänsch, Phys. Rev. Lett. **84,** 5102-5105 (2000).

[114] A. Gondarenko, J. S. Levy, and M. Lipson, Opt. Express **17,** 11366-11370 (2009).

[115] T. Carmon, L. Yang, and K. J. Vahala, Opt. Express **12,** 4742-4750 (2004).

[116] A. A. Savchenkov, A. B. Matsko, W. Liang, V. S. Ilchenko, D. Seidel, and L. Maleki, Nature Photon. **5**, 293-296 (2011).

[117] C. Y. Wang, T. Herr, P. Del'Haye, A. Schliesser, J. Hofer, R. Holzwarth, T. W. Hansch, N. Picque, and T. J. Kippenberg, Nature Comm. **4**, 1345 (2013).

[118] K. Saha, Y. Okawachi, J. S. Levy, K. Luke, R. K. W. Lau, M. A. Foster, M. Lipson, and A. L. Gaeta, Opt. Express **20**, 26935-26941 (2012).

[119] A. R. Johnson, Y. Okawachi, J. S. Levy, J. Cardenas, K. Saha, M. Lipson, and A. L. Gaeta, Opt. Lett. **37**, 875-877 (2012).

[120] K. Saha, Y. Okawachi, B. Shim, J. S. Levy, R. Salem, A. R. Johnson, M. A. Foster, M. R. E. Lamont, M. Lipson, and A. L. Gaeta, Opt. Express **21**, 1335-1343 (2013).

[121] R. Trebino, Nature Photon., **5**, 189192(2011).

[122] A. P. Shreenath, *Measuring Broadband, Ultraweak, Ultrashort Pulses*, Ph.D thesis, Georgia Institute of Technology (2005).

[123] S. Abdullah Aljunid, *Optical Autocorrelation using Non-Linearity in a Simple Photodiode*, Bachelor's thesis, National University of Singapore (2007).

[124] H. P. Weber, Journal of Applied Physics, **38**, 2231 (1967).

[125] M. Maier, W. Kaiser, and J. A. Giordmaine, Physical Review Letters, **21**, 12751277 (1966).

[126] J-C. Diels and W. Rudolph *Ultrashort Laser Pulse Phenomena: Fundamentals, Techniques, and Applications on a Femtosecond Time Scale* Academic Press, 2nd edition, 2006.

[127] R. K. Shelton, L.-S. Ma, H. C. Kapteyn, M. M. Murnane, J. L. Hall, and J. Ye, Science **293,** 1286-1289 (2001).

[128] A. Ehlers, I. Riemann, S. Martin, R. Le Harzic, A. Bartels, C. Janke, and K. König, J. Appl. Phys. **102,** 014701 (2007).

[129] J. Ye, J.-L. Peng, R. J. Jones, K. W. Holman, J. L. Hall, D. J. Jones, S. A. Diddams, J. Kitching, S. Bize, J. C. Bergquist, L. W. Hollberg, L. Robertsson, and L.-S. Ma, J. Opt. Soc. Am. B **20,** 1459-1467 (2003).

[130] S. T. Cundiff and J. Ye, Rev. Mod. Phys. **75,** 325 (2003).

[131] J. Schröder, S. Coen, F. Vanholsbeeck, and T. Sylvestre, Opt. Lett. **31,** 3489-3491 (2006).

[132] A. Martinez and S. Yamashita, Opt. Express **19,** 6155-6163 (2011).

[133] H. A. Haus, J. Sel. Top. Quantum Electron. **6**, 1173-1185 (2000).

[134] S. Xiao, L. Hollberg, and S. A. Diddams, Opt. Lett. **34,** 85-87 (2009).

[135] J. Benedict, J. G. Fujimoto, and F. X. Kartner, Nature Photon. **6**, 97-100 (2012).

[136] A. Bartels, D. Heinecke, and S. A. Diddams, Science **326**, 681 (2009).

[137] S. Pekarek, T. Südmeyer, S. Lecomte, S. Kundermann, J. M. Dudley, and U. Keller, Opt. Express **19**, 16491-16497 (2011).

[138] D. Lorenser, D. J. H. C. Maas, H. J. Unold, A.-R. Bellancourt, B. Rudin, E. Gini, D. Ebling, and U. Keller, IEEE J. Quantum Electron. **42**, 838-847 (2006).

[139] P. Klopp, U. Griebner, M. Zorn, and M. Weyers, Appl. Phys. Lett. **98**, 071103 (2011).

[140] M. Hoffmann, O. D. Sieber, V. J. Wittwer, I. L. Krestnikov, D. A. Livshits, Y. Barbarin, T. Südmeyer, and U. Keller, Opt. Express **19**, 8108-8116 (2011).

[141] J. Davila-Rodriguez, I. Ozdur, C. Williams, and P. J. Delfyett, Opt. Lett. **35**, 4130-4132 (2010).

[142] M. Akbulut, N. Hoghooghi, D. Mandridis, S. Ozharar, F. Quinlan, and P.J. Delfyett, Photon. Technol. Lett. **22**, 431-433 (2010).

[143] A. B. Matsko, A. A. Savchenkov, V. S. Ilchenko, D. Seidel, and L. Maleki, Phys. Rev. A **85**, 023830 (2012).

[144] F. Leo, S. Coen, P. Kockaert, S.-P. Gorza, P. Emplit, and M. Haelterman, Nature Photon. **4**, 471-476 (2010).

[145] R. Salem, M. A. Foster, A. C. Turner-Foster, D. F. Geraghty, M. Lipson, and A. L. Gaeta, Opt. Express **17**, 4324-4329 (2009).

[146] Y. Okawachi, R. Salem, A. R. Johnson, K. Saha, J. S. Levy, M. Lipson, and A. L. Gaeta, Opt. Lett., **37**, 4892-4894 (2012).

[147] K. Saha, P. Londero, J. Levy, A. Slepkov, A. Bhagwat, V. Venkataraman, M. Lipson, and Alexander L. Gaeta, Bulletin of the American Physical Society 41st Annual Meeting of the APS Division of Atomic, Molecular and Optical Physics, Volume 55, Number 5, (2010).

[148] N. K. Langford, S. Ramelow, R. Prevedel, W. J. Munro, G. J. Milburn, and A. Zeilinger, Nature **478**, 360 (2011).

[149] K. Uesaka, K. K.-Y. Wong, M. E. Marhic, and L. G. Kazovsky, IEEE J. Sel. Top. Quantum Electron. **8**, 560 (2002).

[150] T. Wilken, G. Lo Curto, R. A. Probst, T. Steinmetz, A Manescau, L Pasquini, J. I. González Hernández, R. Rebolo, Th. W. Hänsch, T. Udem and R. Holzwarth, Nature **485**, 611614(2012).

[151] C-H. Li, G. Chang, A. G. Glenday, N. Langellier, A. Zibrov, D. F. Phillips, F. X. Kartner, A. Szentgyorgyi, and R. L. Walsworth, Opt. Lett., **37**, 3090-3092(2012).

[152] A. Schliesser, N. Picqué, Theodor W. Hänsch, arXiv:1205.3395.

[153] L. Bei, J. Hu, P. Jiang, D. H. Kim, G. F. Dionne, L. C. Kimerling, and C. A. Ross, Nature Photon. **5**, 758 (2011).

[154] D. Dai, J. Bauter, and J. E. Bower, Light: Science & Applications, doi:10.1038*lsa*.2012.1 (2012).

[155] Z. Yu, and S. Fan, Nature Photon. **3**, 91 (2009).

[156] M. S. Kang, A. Butsch, and P. St. J. Russell, Nature Photon. **5**, 549 (2011).

[157] X. Huang, and S. Fan, J. of Lightwave Tech. **29**, 2267 (2011).

[158] H. Lira, Z. Yu, S. Fan, and M. Lipson, Phys. Rev. Lett. **109**, 033901 (2012).

[159] S. Manipatruni, J. T. Robinson, and M. Lipson, Phys. Rev. Lett. **102**, 213903 (2009).

[160] L. Fan, J. Wang, L. T. Varghese, H. Shen, B. Niu, Y. Xuan, A. M. Weiner, and M. Qi, Science **335**, 447 (2012).

[161] M. Shalaby, M. Peccianti, Y. Ozturk, and R. Morandotti, Nature Comm. **4**, 1555 (2013).

[162] K. Inoue, IEEE Phot. Tech. Lett. **6**, 1451 (1994).

[163] M. E. Marhic, Y. Park, F. S. Yang, and L. G. Kazovsky, Opt. Lett. **21**, 1906 (1996).

[164] A. H. Gnauck, R. M. Jopson, C. J. McKinstrie, J. C. Centanni, and S. Radic, Opt. Express **14**, 8989 (2006).

[165] D. Mechin, R. Provo, J. D. Harvey, and C. J. McKinstrie, Opt. Express **14**, 8995 (2006).

[166] T. Tanemura, C. S. Goh, K. Kikuchi, and S. Y. Set, IEEE Photon. Tech. Lett. **16**, 551 (2004).

[167] V. R. Almeida, R. R. Panepucci, and M. Lipson, Opt. Lett. **28**, 1302 (2003).